NOVA SCHOOL OF SCIENCE & TECHNOLOGY

DEPARTAMENT OF MECHANICAL AND INDUSTRIAL ENGINEERING

FRANCISCO LUÍS MATHIOTTE CASTANHO

BSc. in Mechanical Engineering

DESIGN OF A TESTING DEVICE FOR AN ANATOMICAL PART OF THE ASCENDING AORTA

MASTER IN MECHANICAL ENGINEERING

NOVA University Lisbon
February, 2022

NOVA SCHOOL OF SCIENCE & TECHNOLOGY

DEPARTAMENT OF MECHANICAL AND INDUSTRIAL ENGINEERING

DESIGN OF A TESTING DEVICE FOR AN ANATOMICAL PART OF THE ASCENDING AORTA

FRANCISCO LUÍS MATHIOTTE CASTANHO

BSc. in Mechanical Engineering

Adviser: José Manuel Cardoso Xavier
Assistant Professor, NOVA University Lisbon
Co-Adviser: António Joaquim da Cruz Tomás
Hospital Santa Marta

Examination Committee:

Chair: Rui Fernando dos Santos Pereira Martins
Associate Professor, NOVA School of Science and Technology, NOVA University Lisbonn
Rapporteur: António José Freire Mourão
Associate Professor, NOVA School of Science and Technology, NOVA University Lisbon
Paulo José da Silva Tavares
Senior Investigator, Institute of Science and Innovation in Mechanical and Industrial Engineering (INEGI)
Adviser: José Manuel Cardoso Xavier
Assistant Professor, NOVA School of Science and Technology, NOVA University Lisbon

MASTER IN MECHANICAL ENGINEERING

NOVA University Lisbon

February, 2022

Design of a testing device for an anatomical part of the ascending aorta

"You cannot teach a man anything; you can only help him discover it in himself." (Galileo)

Agradecimentos

Em primeiro lugar, gostaria de agradecer ao orientador deste projeto, Prof. José Xavier, professor auxiliar na Faculdade de Ciências e tecnologia, por me ter possibilitado a oportunidade de integrar um projeto interessante e com um papel extremamente importante no âmbito da biomecânica, e pelas diversas novas aprendizagens que adquiri relativamente a ferramentas cruciais tanto no âmbito da engenharia e do seu futuro, como em metodologias de trabalho e organização.

Ao Dr. António Tomás, cirurgião cardíaco no Hospital de Santa Marta, coorientador do projeto, cujo contributo de conhecimento no âmbito da medicina e prática clínica foi fundamental para a concretização do trabalho.

Aos meus colegas universitários, cujos projetos feitos anteriormente tiveram um contributo como referência para esta dissertação.

A todos os meus amigos e familiares próximos, pelo apoio pessoal e o interesse demonstrado pelo projeto durante o seu desenvolvimento.

Aos meus pais, por serem modelos de apoio e coragem, cuja presença constante na minha vida, compreensão e ajuda foram cruciais nos últimos tempos.

Finalmente, gostaria de agradecer à minha namorada, Leonor, por todo o apoio e afeto incomensurável durante os últimos meses, pelo interesse e curiosidade no meu trabalho, e por toda a compreensão nas alturas onde o tempo é escasso.

Muito obrigado.

Este trabalho é financiado por fundos nacionais através da FCT – Fundação para a Ciência e a Tecnologia, I.P., no âmbito do projeto «PTDC/EMD-EMD/1230/2021» com o título «Interação fluido-estrutura para avaliação funcional de aneurismas da aorta ascendente: uma abordagem biomecânica para a prática clínica».

Resumo

O aneurisma da aorta é uma patologia de risco que provoca milhares de mortes mundialmente. O critério atual para intervenção cirúrgica é o diâmetro da aorta, no entanto, uma grande percentagem de pacientes com dissecção ou rutura da aorta apresenta um diâmetro normal. Métodos computacionais têm sido adotados para modelar o comportamento biomecânico de tecido biológico e auxiliar no diagnóstico desta patologia. Testes experimentais nestes tecidos são executados para validar os modelos. O objetivo deste estudo é um contributo para uma plataforma digital integrando métodos computacionais para o desenvolvimento de um mecanismo de ensaio experimental, cuja identificação de parâmetros material deve ser auxiliada pela técnica de correlação digital de imagem 3D. Esta abordagem segue um desenvolvimento de produto orientado por simulação numérica, em que a análise computacional é totalmente integrada como parte do projeto mecânico. Teoria Axiomática de Projeto é tida em consideração para desenvolver o dispositivo de uma forma clara, metódica e eficiente. Um caso de estudo é analisado e uma geometria da peça anatómica 3D, específica de um paciente, é obtida através da segmentação de imagens de uma angiotomografia. Uma metodologia é apresentada atribuindo um modelo constitutivo hiperelástico ao material e executando análise de elementos finitos. Como trabalho futuro a identificação dos parametros constitutivos deve ser obtida com recurso a métodos inversos avançados baseados em campos de deformação obtidos por correlação digital de imagem.

Palavras-chave: Aorta ascendente; Aneurisma; Mecânica computacional; Projeto mecânico; Plataforma digital

Abstract

Aortic aneurysms are life-threatening pathologies that cause thousands of deaths worldwide. The current main clinical criteria for surgical intervention is aortic diameter, although a large percentage of patients with dissection or rupture has a normal diameter. Computation methods have been adopted to model the biomechanical behaviour of biological tissue in view of adding in the diagnosis of this pathology. Furthermore, experimental testing on aneurismatic aortic tissue has been performed to validate these models. The objective of this study is to integrate computational mechanical methods into an innovative experimental test with a specifically designed device where material parameters are obtained by inverse methods assisted by Digital Image Correlation (DIC). Axiomatic Design (AD) is taken into consideration to develop the testing device in a clear, methodical, and efficient way. A case study is analysed, and a patient-specific 3D geometry of an Ascending Thoracic Aortic Aneurysm (ATAA) is obtained by segmenting Computed Tomography Angiography (CTA) images. A methodology is presented by attributing a hyperelastic constitutive model to the geometry and executing Finite Element Analysis (FEA). Future work should rely on real experimental tests where Finite Element Model Updating (FEMU) should be adopted to fit the constitutive model more accurately to the actual specimen material.

Keywords: Ascending aorta; Aneurysm; Computational mechanics; Mechanical design; Digital platform

Table of Contents

List of Figures

List of Tables

Acronyms

4D-US Time Resolved 3D Ultrasound 13
AAA Abdominal Aortic Aneurysm 8, 9, 13, 57
AD Axiomatic Design 25
AISI American Iron and Steel Institute 39
ATAA Ascending Thoracic Aortic Aneurysm vii, viii, 1, 2, 11, 17–19, 28, 33, 35, 37, 51, 54, 57, 65, 66
CAD Computer-Aided Design 1
CFD Computational Fluid Dynamics 23
CSM Computational Solid Mechanics 23
CT Computed Tomography vii, ix, 10, 11, 13, 14, 52, 55, 57
CTA Computed Tomography Angiography ix, 1, 11, 12, 51, 53, 54, 56, 66
CTD Connective Tissue Disorder 20
DIC Digital Image Correlation 18, 20, 29, 30, 32, 65, 66
DICOM Digital Imaging and Communications in Medicine 1, 2, 13, 51
ECM Extracellular Matrix 5
EGTA Ethylene Glycol Tetraacetic Acid 21
FE Finite Element ix, 10, 53, 56, 66
FEM Finite Element Method 10, 13
FEMU Finite Element Model Updating 13
FSI Fluid-Sructure Interaction 1, 10, 13, 15, 23
ILT Intraluminal Thrombus 9
MRI Magnetic Resonance Imaging 1, 10, 11, 13, 52
NURBS Deforming Non-uniform Rational Basis Spline vii, 18, 20, 21
PACS Picture Archiving and Communication System 52
PBS Phosphate-Buffered Saline 21
PET Positron Emission Tomography 10, 52
RPI Rupture Potencial Index 9
STL Standard Triangle Language x, 51, 52, 57, 58
TAA Thoracic Aortic Aneurysm 8–10, 25
TAV Tricuspid Aortic Valve vii, 17, 19
TEE Transoesophageal Echocardiography 11
TTE Transthoracic Echocardiography 10

Symbols

k Bulk modulus
A_{cr} Axiomatic design common range
D Internal diameter of the aorta
d Diameter of a circle
f_z Force in the axial direction
f_θ Force in the circunferential direction
I Information content
λ_θ Stretch in the circumferential direction
λ_z Stretch in the axial direction
L Length in unloaded state
P Intraluminal pressure on the aorta
ν Poisson's ratio
p_s Probability of success
R Radius in the unloaded state
r Radius in the loaded state
$\sigma_{\theta\theta}$ Stress in the circunferential direction
σ_{zz} Stress in the axial direction
A_{sr} Axiomatic design system range
T Wall tension on the aorta tissue
t Wall thickness of the aorta
E Young's modulus

1 Introduction

1.1 Motivation

The Ascending Thoracic Aortic Aneurysm (ATAA) is a life threatening pathology estimated to be diagnosed to 45,000 patients each year in Europe and the United States (Elefteriades and Farkas, 2010). The diameter of the aorta is the primary clinical criterion for determining if surgical intervention is required. However, more than half of patients with dissection of the aorta have a normal diameter, indicating that there could be other conditioning factors. There is a fundamental interest in determining which factors are associated with the progression of the ascending aortic aneurysm.

Computational mechanical methods have become a fundamental tool in several engineering fields, including biomechanics of living systems. In the framework of the aorta tissue, the research interest has been focused on the analysis of the biomechanics of the aneurysm formation and growing. This virtualization tool is intended to add value by understanding the physiology and pathophysiology of the aneurysm. Ultimately, it aims to be a tool to be used in practical clinical skills for diagnosis of aortic aneurysm formation and prediction of risks of rupture (Maier et al., 2010; Vorp, 2007).

Based on the finite element method, the construction of the biomechanical computational models of an aorta requires three main ingredients: the patient-specific geometry, representative mechanical properties, governing a given selected constitutive law, and the physiological boundary conditions. The former has been solved by creating the Computer-Aided Design (CAD) geometry of the inner organ, reconstructed from Digital Imaging and Communications in Medicine (DICOM) standard data from imaging techniques such as Computed Tomography Angiography (CTA), Magnetic Resonance Imaging (MRI), and Ultrasound. Boundary conditions can be estimated with different degrees of approximation, starting from a simple constant pressure up to more sophisticated physiological fluid-structure interaction (FSI) analysis. The material properties to be input need to be calibrated or obtained based on experimental observations.

Several mechanical tests have been proposed to measure the mechanical properties of aortic tissue (Khanafer et al., 2011; Di Giuseppe et al., 2019; Sommer et al., 2016; Duprey et al., 2016; Sommer et al., 2013). Experimental tests can be conveniently coupled with image-based measurements for full-field and contactless observations of the deformation of the tissues (Kim et al., 2011a,b). Advanced inverse identification method can then be used to extract relevant mechanical properties (Davis et al., 2015, 2016; Trabelsi et al., 2015; He et al., 2021; Felfelian et al., 2019; Zhao et al., 2011; Lu et al., 2008).

1.2 Objectives

On this project, it is intended to design an experimental device capable of determining mechanical properties of a piece of anatomical part of the ascending aorta. At this stage of conceptualization, the idea is embedding this device into a digital twin approach for the analysis of the biomechanical behavior of an anatomical aorta piece. The testing device will consist of the insufflation of the piece at study. A finite element model can be used to predict the overall deformation of the aortic piece. This approach follows a simulation-driven product development, in which the simulation is fully integrated as a part on the mechanical design (Jansson et al., 2020; Nikolaev et al., 2018; Sravan et al., 2017).

1.3 Outline

In this paper, several matters will be approached in order to outline the goal of the investigation at hand.

In chapter 1, the motivation and objectives are presented, where the impact numbers of ATAA aneurysms and the uncertainties related to diagnosis and clinical repair are mentioned. A brief presentation of computational tools that aid in the diagnosis and biomechanical characterization is made, and the objectives of both the presented study and the larger-scale investigation on which it is inserted are explained.

Chapter 2 presents itself as a state of art. The anatomy and function of the aorta and its layers are presented, as well as the different types of aneurysms. The importance of a biomechanical approach to the study of this type of pathology is a key subject, and examples of the computational tools used for this purpose are given. The path from obtaining *in-vivo* images to creating a 3D model of a biological structure is explained. Experimental tests performed on biological tissue are thoroughly described regarding sample preparation, test protocol, and data analysis.

In chapter 3, the requirements of the testing design are explained, and the parameters and physical parts necessary to satisfy such requirements are obtained with the aid of Axiomatic Design Theory. The functioning of the mechanism is thoroughly described regarding specimen fixation, mechanical test performance, and the data analysis method intended. The design of key parts is shown as well as chosen tolerances for dimensions and clearances in the assembly of different parts.

Chapter 4 intends to be a proof of concept for the creation of a digital-twin platform for the experimental test. A patient-specific 3D model based on clinical imaging data is obtained thanks to an open-source DICOM segmentation software. The model is then uploaded to software where its assembly on the experimental device can be observed, a finite element mesh is created and the virtualization of the test is performed by simulating a constant internal pressure. The boundary conditions are approximated by fixing the sample on both edges.

Chapter 5 presents the conclusions of the document, as well as future work indications to assure the continuity of the project. Although the main concept, parts, and functioning of the device were determined, there is room for improvement. A deeper analysis of the design may

discover alterations that lead to better solutions. Several choices made in the design phase can only be validated within the construction and testing phases.

2 On the biomechanical characterisation of aneurysmatic aortic tissue

2.1 Introduction

In order to consistently evaluate the mechanical behaviour of the wall tissue of the aorta, it is firstly necessary to comprehend the mechanisms behind the event of an aortic aneurysm and aortic dissection. To start with, a brief introduction of the anatomy of the aorta and thoracic aortic aneurysms is given, from an engineering perspective. A scientific question regarding the importance of a biomechanical approach in study the aortic aneurysm will be then addressed. An overview is given to the currently imagiology methods for inspecting the aortic tissue and structures without open surgery. Finally, a systematic literature review on the experimental test methods for characterising aortic tissue is presented. Different experimental tests are revised in link with the numerical tools that are used to model the biomechanical behaviour of the tissue.

2.2 On the anatomy of the aorta

The aorta is the largest artery in the human body. It has many branches as illustrated in Figure 2.1. The aorta has a major role on the entire cardiovascular system due to its conduit function and elastic behaviour that significantly influences the regulation of the left ventricular performance, myocardial perfusion, and arterial function.

The aorta tissue itself is composed of the *tunica intima*, *tunica media*, and the *tunica adventitia* (Figure 2.2). The *tunica intima* is the innermost layer and comprises one layer of endothelial cells (cells in direct contact with blood or lymph). The *tunica media* is the middle layer consisting of a three-dimensional network of smooth muscle cells, elastin, and collagen fibers. It is usually the thickest layer and its main function is to change vessel diameter to regulate blood flow and pressure, endowing the aorta with its distensibility, as the elastin structure recoils the arterial tissue during each pulse cycle. Collagen gives stiffness, strength, and toughness to the vascular wall. The *tunica adventitia* is the outermost layer of the aorta and comprises fibroblasts and fibrocytes, and Extracellular Matrix (ECM) components of bundles of collagen fibers. The ECM quantifies the amount of stress and/or strain that is transmitted to individual cells of vascular tissue (Elefteriades, 2008; Gasser, 2017).

2.3 On the anatomy of the aortic aneurysm

An aortic aneurysm is a localized dilatation of the aorta diameter due to wall weakening. The increase in size can result in rupture, which is a life-threatening emergency. Aneurysms can be

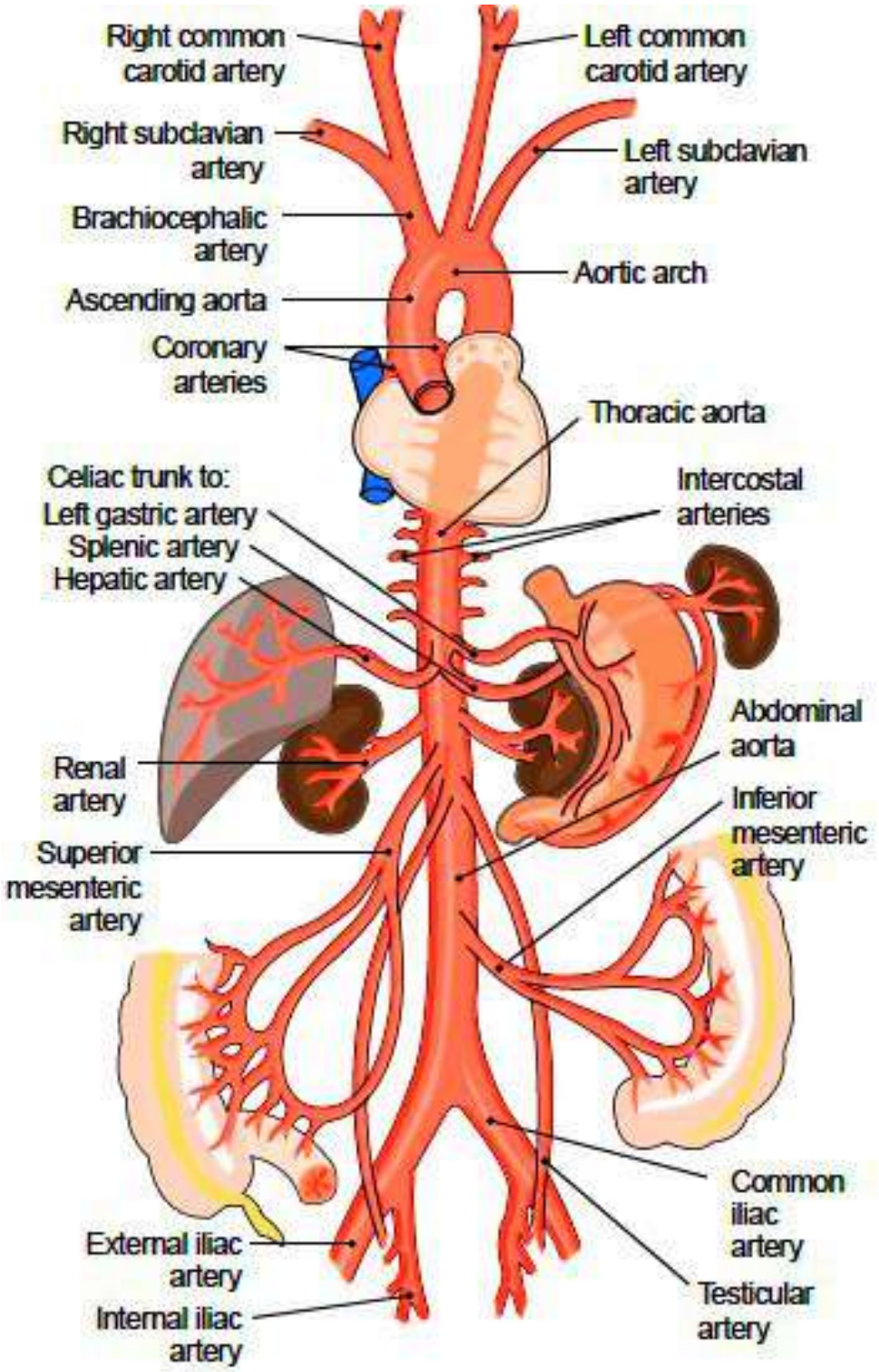

Figure 2.1: Aorta artery and branches. From (www.encyclopedia.lubopitko-bg.com Corporation).

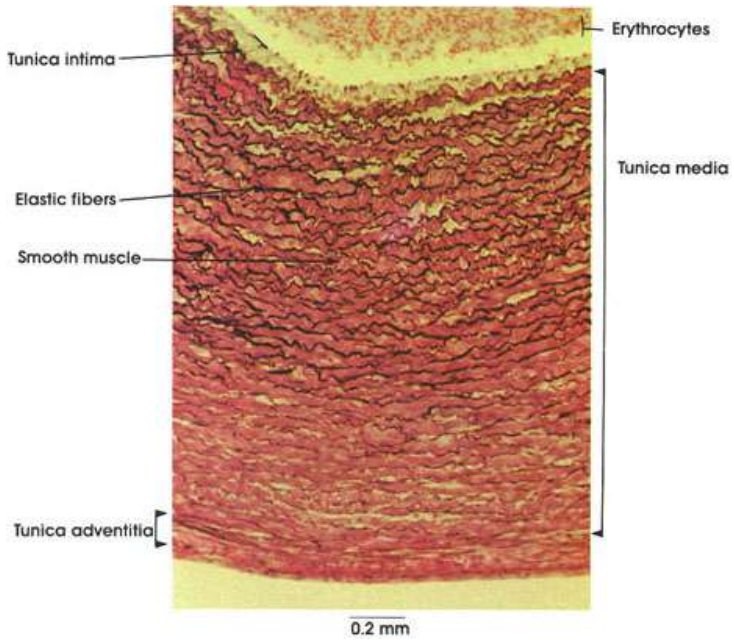

Figure 2.2: Aortic wall characterisation by layer. From (Bergman et al.).

classified according to morphology, location, and etiology. As for morphology, aneurysms can be distinguished between fusiform and saccular. A fusiform aneurysm is roughly cylindrical shaped and affects the entire circumference of the vessel, whereas a saccular aneurysm is a dilatation of only a portion of the vessel wall. Regarding their location, they can be sorted out according to the segment affected as thoracic, thoracoabdominal, or abdominal (Figure 2.3). The thoracic segment can yet be divided into ascending thoracic, transverse arch, and descending thoracic (Figure 2.3).

Different pathologies can occur on the aortic wall, that are similar to an aneurysm. A false aneurysm (Figure 2.4) represents a rupture of the aorta, as the wall in this case does not comprise the same histologic components of the normal aorta wall, but it is rather a fibrous peel formed from a small perforation of the artery. In a true aneurysm (Figure 2.4), being the vast majority of aneurysms seen in patients, the wall of the aneurysm is composed of the normal histologic components of the aorta (Elefteriades, 2008). The previous two should not be confused with a dissecting aneurysm, a process in which occurs a separation of layers of the aortic wall (Figure 2.4).

2.4 Is the experimental and computational biomechanical approach relevant to evaluate the risk of rupture of aortic aneurysms?

Over the last years, incidents of aneurysms have been increasing due to factors such as the aging of the population and the increasing number of smokers. Risk factors like tobacco smoking, male sex, age, and hypertension have been found to influence negatively the occurrences of AAA disease (Powell et al., 2010). Recent advances in non-invasive diagnostic exams, based on imaging technologies, have been helping in the premature detection of aneurysm formation. Although the current clinical practice dictates that the aneurysmatic aorta should be replaced

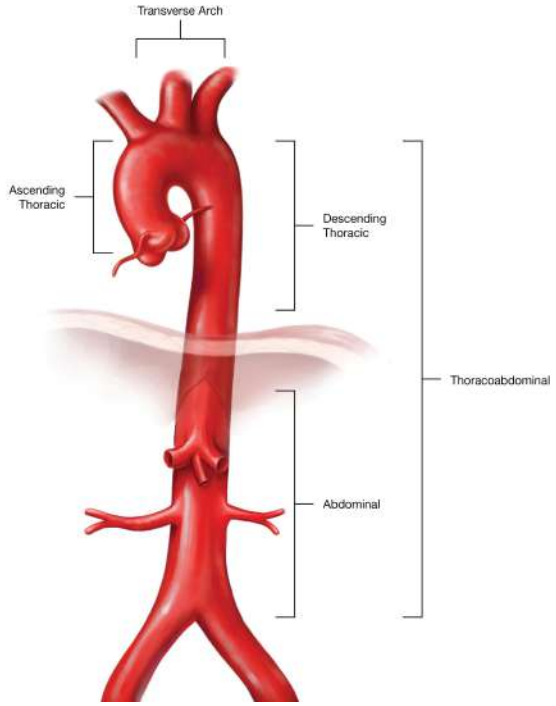

Figure 2.3: Representation of aorta segments. From (UAB Medicine).

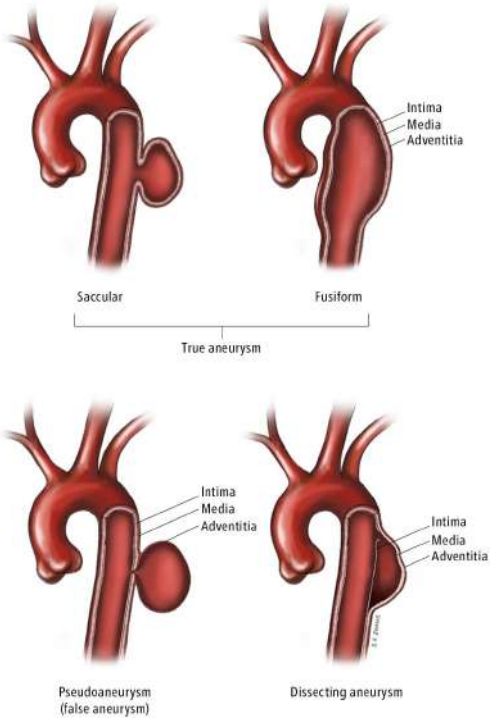

Figure 2.4: Distinction between true, false and dissecting aneurysms. Classification of aneurysms based on morphology. From (Szalay and Frołow, 2019).

when the diameter of the aneurysm reaches 5.0-5.5 cm, both for TAA and AAA, up to 23% of the rupture cases can occur at diameters below 5.0 cm (Powell et al., 2010). Therefore, it is desirable to have a patient-specific approach so that the rupture or dissection risk can be more reliable, allowing for a prognosis and treatment course unique to each patient.

From a biomechanical perspective, aneurysm ruptures or dissects can occur when the wall stress locally exceeds the wall strength of the biological tissue. From the law of Laplace it is stated that,

$$T = \frac{PD}{2t} \tag{2.1}$$

where,

- T is the wall tension on the aorta tissue;
- P is the intraluminal pressure on the aorta;
- D is the internal diameter of the aorta;
- t is the wall thickness of the aorta.

This theoretical equation was earliest used for evaluate the maximum diameter criterion for the clinical support of the risk for AAA rupture (McGloughlin, 2011). However, this law has two major fallacies regarding its application in biomechanics. First, the law assumes that the vessel has a simple cylindrical or spherical shape with a uniform radius of curvature, whereas the aortic wall has a complex geometry, with a greater and a lesser curvature. Secondly, rupture

predictions based on the wall stress alone are not sufficient since a region of the wall under elevated stress may also have a higher wall strength, this way rupture potential equalizes.

Biomechanical experimental testing has shown that aneurysmatic tissue is substantially weaker and stiffer than the normal aorta. These *ex-vivo* observations have also allowed to point out the high heterogeneity of the aneurysm wall strength, both region to region in the same patient and among patients (Davis et al., 2016) (Figures 2.5 and 2.6). One of the most important findings on the biomechanical study of aneurysmatic tissue is that the tensile strength does not appear to be related to the diameter of the aneurysm.

Criteria such as the rate of aneurysm growth, stiffness, Intraluminal Thrombus (ILT) thickness in AAA, peak wall stress, and wall tension have been proposed to predict the aneurysm rupture. Nevertheless, these empirical approaches have their limitations that could potentially lead to erroneous indications regarding TAA and AAA clinical decisions. In this regard, new concepts have been proposing for patient-specific diagnostic assessment, such as the Rupture Potencial Index (RPI) (Maier et al., 2010; Vorp et al., 2006), which is the ratio of the actual wall stress to the wall strength at a particular point on the aneurysm wall. Consistently, the RPI parameter was found to be higher in AAA that have ruptured in regard to the ones that did not rupture. Moreover, a significant differentiation for the rupture risk was found for aneurysm diameter between 55 and 75 mm of asymptomatic and symptomatic/ruptured AAAs, where the maximum diameter had failed to predict the actual risk of rupture (Maier et al., 2010).

During AAA formation and enlargement, the biomechanics of the aortic wall change drastically, the tensile strength decreases as the aneurysm expands and wall strength and stiffness are spatially variable. Local factors such as wall stress and/or hypoxia contribute to the decrease of the biomechanical strength of the artery wall by local degradation (McGloughlin, 2011).

One of the major obstacles of the biomechanical approach on aneurysmatic tissue is the difficulty of obtaining patient-specific properties, an issue that is related to the absence of methodology to estimate stress *in-vivo* via non-invasive techniques. Since, generally, the stress of a deformable body depends on its geometry, load, boundary conditions, and mechanical properties (Cosentino et al., 2019), there is a large and growing interest in reformulating computational mechanics so that stress predictions are weakly sensitive to the variation of mechanical properties once the deformed configuration is given (Miller and Lu, 2013). A method to compute AAA wall stress without being necessary the input on material parameters has been performed by Joldes et al. (2015), even if the approach on modeling the ascending aorta still needs further investigation (Cosentino et al., 2019).

2.5 Overview of computational tools for modeling the biomechanical behaviour of aortic aneurysms

The use of computational tools to model biological tissue is a key ingredient to further understanding its biomechanical behaviour. Several different approaches have been proposed to model aortic aneurysm behaviour. Aortic aneurysms are usually modeled as hyperelastic, incompressible materials, with the stress-strain material response described by a constitutive equation derived from strain energy functions (Kim et al., 2011a; Davis et al., 2015; Gasser, 2017). Ex-

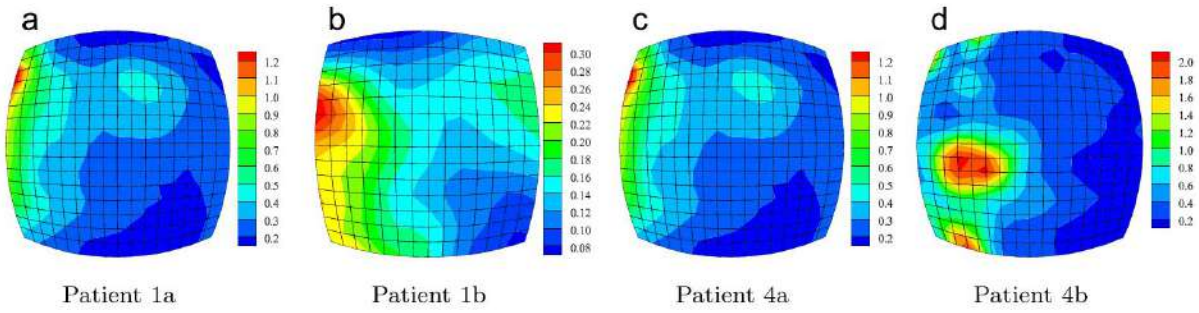

Figure 2.5: Maps of the strain energy for a uniform equibiaxial stretch of 1.2 using the pointwise material properties for (a) Patient 1a, (b) Patient 1b, (c) Patient 4a, and (d) Patient 4b. From (Davis et al., 2016).

perimental *ex-vivo* tests on aortic tissue have been carried out to identify specific material parameters to fit known constitutive model equations. These studies have given a new insight into the biomechanical behaviour of these tissues. These data is fundamental when carrying out computational analysis, even if deterministic parameters have limitations when estimating patient-specific mechanical properties of TAA.

Finite Element Method (FEM) is currently a common method to model aneurysm behaviour. A patient-specific FE model can be obtained with the aid of imaging techniques followed by adequate segmentation and 3D model generation. These models usually rely on the material properties obtained from experimental tests. However, current advances on computational tools have allowed the development of Fluid-Sructure Interaction (FSI) approach, which is a promising tool to assess fluid forces acting on the aortic wall and the possible hemodynamic disturbances caused by the existence of an aneurysm, as it provides a more accurate representation of the *in-vivo* environment.

2.5.1 Imagiology: clinical techniques

There are several methods for imaging internal organs such as the aortic aneurysms. These techniques can be sorted regarding the type of information extracted from the images. They can be classed accordingly into structural and biological functions techniques. Examples of the former are X-ray angiography, Computed Tomography (CT), MRI and Ultrasound. An example of the latter is Positron Emission Tomography (PET).

Imaging techniques are crucial in the assessment, diagnosis, follow-up, and management of aortic aneurysms. Most are non-invasive techniques and all have limitations and strengths and are used for slightly different purposes within the clinical course of an aneurysm. Ultrasound, CT, and MRI are the most common techniques used, each of them having some derivations.

PET is a functional or molecular imaging tool used to study biological function in both health and disease, that consists of the mapping of administered positron-emitting radiopharmaceuticals, thus identifying changes at the cellular level (Lameka et al., 2016). Although it is not the most common imaging technique for aneurysmatic evaluation, previous studies have shown its potential role in the clinical assessment of aortic aneurysms, either alone or combined with a CT (PET-CT) (Sakalihasan et al., 2004; Kim and Song, 2018; Rudd et al., 2015)

A Transthoracic Echocardiography (TTE) (Figure 2.7a), is an ultrasound test and it's one

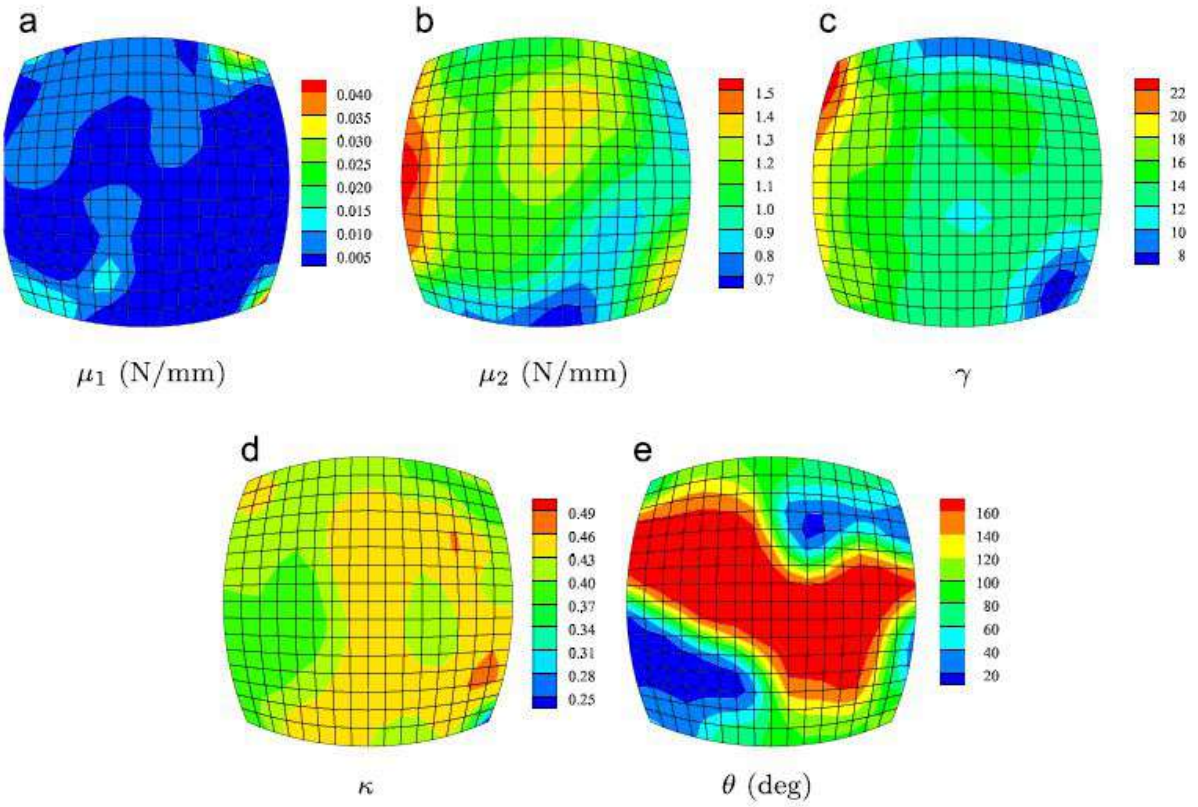

Figure 2.6: Distribution of the identified material parameters μ_1, μ_2, γ, κ, and θ over the ATAA for one of the patients in the study. From (Davis et al., 2016).

of the most used imaging techniques in clinical practice. A transducer emitting ultrasound waves is placed on the chest and allows to see images of the aortic root and proximal ascending aorta. It allows for a correct measurement of aortic diameter and valve morphology and disfunction (Evangelista, 2014).

A Transoesophageal Echocardiography (TEE), also an ultrasound test, is considered semi-invasive for in its procedure, a probe is passed down the esophagus. It has the advantage of providing a high-quality image of almost all the thoracic aorta and being very useful in evaluating regurgitation mechanisms. However, it does not provide accurate measurements of aortic aneurysm diameters. When surgical treatment of a valve is being considered in a patient, this technique is commonly used (Evangelista, 2014).

A CTA) (Figure 2.7b) uses an injection of contrast material in the blood vessels and a CT scanner (multiple x-ray beam sources and x-ray detector spin around the body) to obtain a complete 3D dataset of the vessel. This technique allows for an entire visualization of the aorta and main aortic branches in a short time, and it is widely available. Multidetector Computed Tomography permits an accurate evaluation of the coronary artery and aortic branch disease, making it the technique of choice in the assessment of aortic aneurysms before surgery (Evangelista, 2014).

In an MRI (Figure 2.7c), a strong magnetic field is generated, and sensors detect the energy released as protons on the body align with the magnetic field. It provides significant morphological, functional, and biomolecular information on aortic aneurysms, and can provide significant information of the aortic wall. It may or may not be required the injection of contrast, thus

(a) Echocardiogram

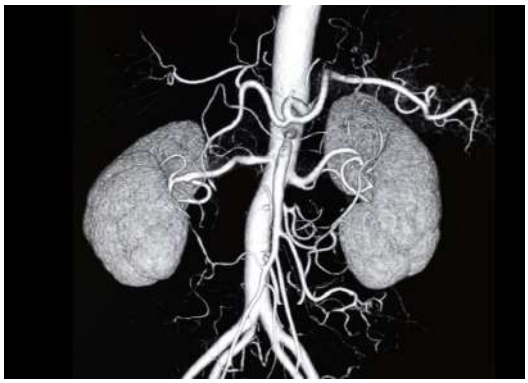

(b) CTA

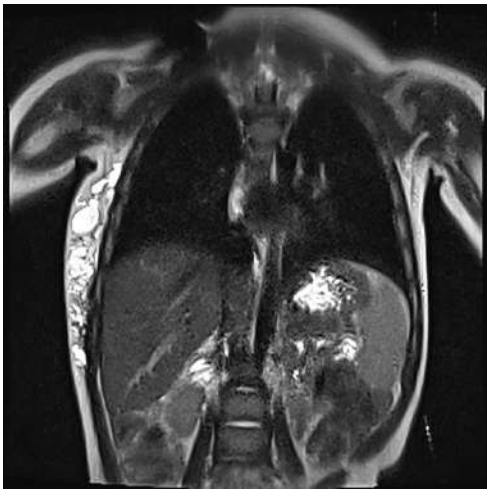

(c) MRI

Figure 2.7: Examples of techniques used in imaging. From (Harkness, 2018), (Go Imaging) and (Gharbia).

enabling for high-quality assessments of the aorta without submitting the patients to radiation exposure (Evangelista, 2014).

2.5.2 Patient-specific geometric and meshing reconstruction

Obtaining a patient-specific 3D reconstruction and a FE model is essential to increase the current knowledge of the aortic aneurysms. These approaches are the *status quo* in the study of the biomechanical behaviour of this physiopathology.

This process begins with analyzing and segmenting data provided by imaging techniques. The most commonly used techniques are CTA or CTA scanning, although they do not provide information on artery thickness. Since understanding more about the aorta thickness is an important step to a more accurate reconstruction, high-quality MR examinations may also be used as a first step of the process, due to the fact that they provide information on wall geometrical parameters (Nguyen et al., 2014).

A common method for the segmentation of the arterial wall is the traditional "snake" model (Figure 2.8). It consists of a deformable contour, or a curve, with a certain mathematical expression, that moves through the plane to minimize the energy function. This function includes

the internal energy which is associated with an elastic property of the snake and external energy which is derived from the particular MR image featuring regions of interest such as boundaries. A similar process proposed in (Auer et al., 2006) consists of a 3D representation by stacking multiple 2D-Derived contours, creating a 3D smooth surface. By including a z-direction derivative energy term in the traditional snake energy function, this representation can be achieved. Figure 2.9 shows the three-dimensional reconstruction with the individual tissue components.

The creation of a FE model starts in the segmentation process, where the outer and inner contours are outlined with a spline-based model from annotated points. Because of the heterogeneity of the thickness of the aorta, and the difficulty of finding this exact value along the artery via imaging techniques, a uniform thickness is usually assumed. Using computer software intended for this purpose, it is possible to interpolate between the offset of the DICOM images provided from the MRI and create surface meshes for both the inner and outer surfaces. A three-dimensional model of an AAA can have a number ranging from, for example, 217 000 to 399 000 elements (Domagała et al., 2018).

CT scans may also be used to reconstruct a 3D model of exact geometry. Computer software can use a marching squares algorithm to threshold and segment the regions of interest of the scan according to a predetermined grayscale value (Doyle et al., 2008). After the segmentation, the software generates polylines around the segmented regions (Figure 2.10), which can then be exported as a chosen format, originating a 3D model. Once the 3D model is generated, a finite element solver can create a mesh with the desired parameters.

2.5.3 In-vivo determination

The modeling of the biomechanical behaviour of the human aorta has been approached, *in-vivo*, via the determination of the elastic properties of the aorta using a non-invasive technique. For this effect, individuals where submitted to time resolved 3D ultrasound (4D-US) while diastolic and systolic blood pressure was measured. Using a speckle tracking algorithm, the displacement field was calculated from the ultrasound data. The definition of a FEM by reconstructing the initial geometry of the aortic segment is possible by analyzing the position of the nodal points, determined by the speckle tracking algorithm, in the end-diastolic position. These nodal points serve as the nodes for the finite element discretisation. A Finite Element Model Updating (FEMU) is used to estimate material properties, showing results with very small errors. The method allows to predict the mechanical properties of the model in the range of deformation resulting from physiological loading, caused by the heart blood pressure, and also to determine the load-free geometry of the aorta (Wittek et al., 2013).

2.5.4 FSI analysis

The FSI approach has been proposed to coupled with the transient interaction between blood flow dynamics and the aorta wall mechanics. This approach allowed to understand the influence of fluid properties with the velocity distribution within the vessel, on strain rate pattern, wall axial displacement, and wall shear stress (Wang and Li, 2011).

In this approach, the hemodynamic and biomechanical changes occurring during the growth

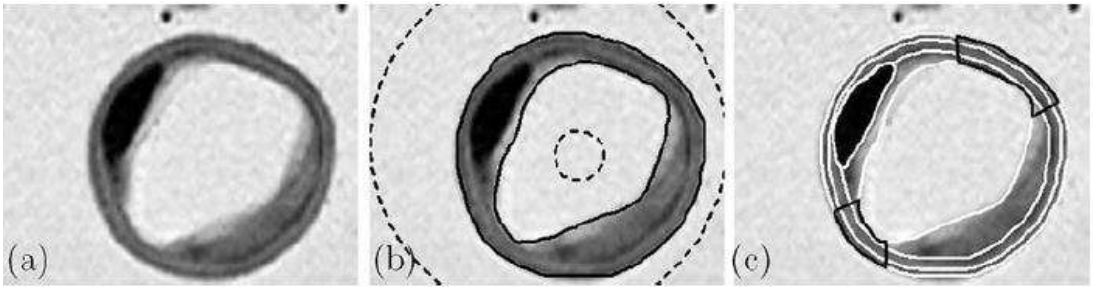

Figure 2.8: Segmentation process: (a) preprocessed MR image; (b) initial (dashed circles) and final (solid lines) snake positions of the boundaries of the arterial wall; (c) segmentation of all arterial components, where the dark boundaries represent the non diseased wall sections. From (Auer et al., 2006).

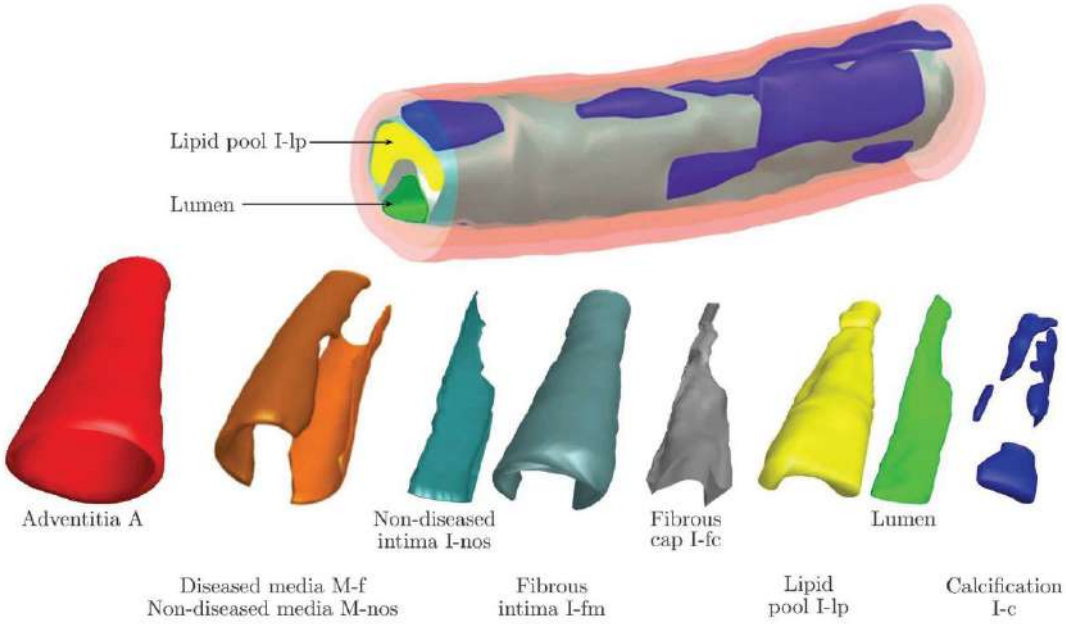

Figure 2.9: 3D reconstruction of a representative stenotic human external iliac artery. Decomposition of its individual tissue components. From (Auer et al., 2006).

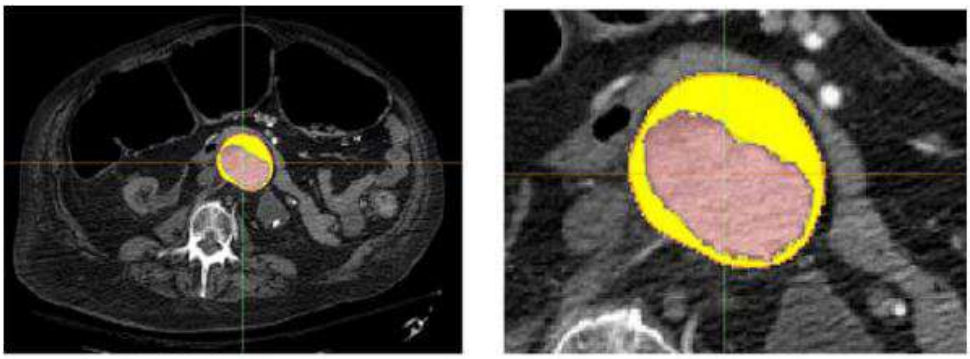

Figure 2.10: Segmentation and polyline generation of CT scan. (a)Full CT scan. (b)Close-up of the region of interest. From (Doyle et al., 2008)

stages of the aortic aneurysm were investigated (Philip et al., 2022). Idealized fusiform aneurysms models were analyzed at different stages and pulsative Newtonian blood flow was assumed as

for fluid characteristics. The numerical simulations were employed with two-way coupled fluid-structure interaction. When evaluating the results, a drastic increase in the maximum wall stresses and wall displacement were observed as the aneurysm approached the critical diameter.

It is possible to conclude that FSI is essential to understand in a very complete way the influence of blood flow on the aortic wall, and also the influence of the growth of the internal diameter due to the aneurysm on blood flow. Also, this is a very important tool in the paradigm of rupture risk index.

2.6 Overview of experimental test methods used for characterising biological tissue

Several experimental tests have been made for characterising and validating current theoretical models of the aortic tissue, aneurysmatic aortic tissue, and other biological tissues. Figures 2.11 and 2.12 show the evolution through time of published articles referring to experimental work, and the quantification of different types of test within the articles in interest, respectively. These data was obtained using the SciVerse Scopus[1] database by collecting relevant publications using predefined searching keywords referring both to experimental tests and aortic aneurysmatic tissue. This section presents a review of these tests focusing on sample preparation, specimen fixation to the testing machine, test protocol, and data analysis.

2.6.1 Uniaxial test

Sommer et al. (2016, 2013) have tested media of diseased human aorta by tensile tests. Dogbone-shaped specimens were prepared using a punch cutter and a scalpel. The overall length of the specimen was 38 mm, and the grip-to-grip length (free length of the specimen) was 20 mm (Figure 2.13). To ensure a secure clamping and to prevent slippage between the specimen and the grip of the testing machine, sandpaper was glued to the ends of the prepared strip with superadhesive gel (Sommer et al., 2013).

Artery tissue can be stored in phosphate-buffered physiological saline at 4°C, and the experimental tests are made within the first 24-48h after being surgically removed. The tissue can also be submitted to cryopreservation in a calcium-free and glucose-free 0.9% physiological saline solution at -80°C.

The specimens were loaded sequentially at different values of the first Piola-Kirchhoff (P-K) stress of 25, 50, 100, and 200 kPa. For each stress value submitted to the samples, four loading and unloading cycles at a constant crosshead speed of 5 $\mathrm{mm\,min^{-1}}$ were executed to obtain repeatable stress-strain curves. Thereafter, the specimen underwent one additional quasi-static cycle with continuous recording of the tensile force, gage length, and width for mechanical data evaluation. After applying the cycles for each level of the P-K stress, the test was finally completed by continuously loading the sample until rupture (Sommer et al., 2013).

Two small black strips were glued transversely and in parallel onto the middle part of the specimen to act as gage markers for the axial deformation measurements via a video-extensometer

[1] https://www.scopus.com/

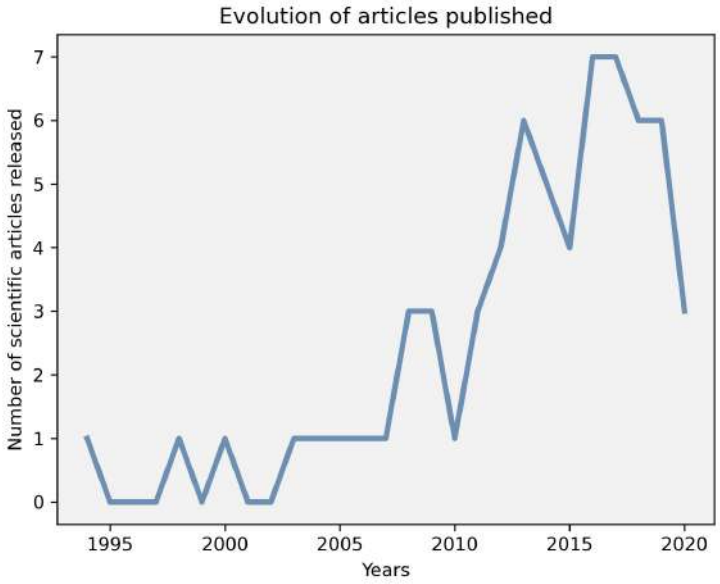

Figure 2.11: Evolution of articles published through time.

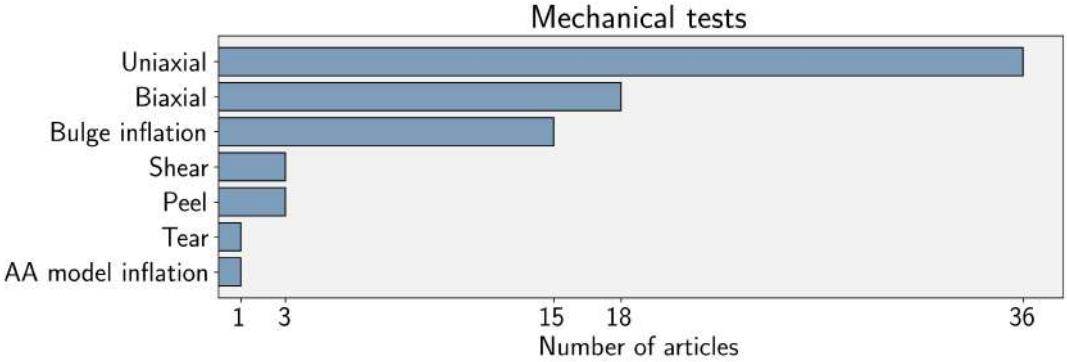

Figure 2.12: Number of articles published regarding different types of experimental tests.

technique.

The Cauchy stresses in the circumferential ($\sigma_{\theta\theta}$) and the axial (σ_{zz}) directions were determined according to:

$$\sigma_{\theta\theta} = \lambda_\theta \frac{f_\theta}{tL_z}, \qquad \sigma_{zz} = \lambda_z \frac{f_z}{tL_\theta} \tag{2.2}$$

where,

- $\lambda_\theta = x_\theta / X_\theta$ represents the tissue stretches in the circumferential direction based on the marker distances in the loaded (x_θ) and unloaded (X_θ) configuration;
- $\lambda_z = x_z / X_z$ represents the tissue stretches in the axial direction based on the marker distances in the loaded (x_z) and unloaded (X_z) configuration;
- f_θ, f_z were the measured forces in each direction;
- t is the mean thickness in the unloaded reference configuration;
- L_z and L_θ are the measured length in the circumferential and axial directions in the undeformed state.

The uniaxial tensile tests were performed in the radial, circumferential, and longitudinal directions. The average ultimate tensile stress of the samples, in the radial direction, were determined to be $\overline{\sigma}^u_{rr} = 131 \pm 56$ kPa, and the ultimate stretch $\overline{\lambda}^u_r = 2.66 \pm 0.68$. In the circumferential and longitudinal directions, the average ultimate tensile stresses and corresponding stretches were determined to be $\overline{\sigma}^u_{\theta\theta} = 1282 \pm 822$ kPa, $\overline{\lambda}^u_\theta = 1.52 \pm 0.20$ and $\overline{\sigma}^u_{zz} = 565 \pm 198$ kPa, $\overline{\lambda}^u_z = 1.50 \pm 0.18$, respectively (Sommer et al., 2013).

2.6.2 Biaxial test

Di Giuseppe et al. (2019) have tested human ATAA specimens from each quadrant of the artery, with a geometry of 15×15 mm, via biaxial test. The specimens were anchored to the testing bench by sutures on the edge using small, surgical fishhooks. The sutures were attached to four electromagnetic motors, as shown in Figure 2.14.

The tests were performed on each quadrant of the ATAA samples (Figure 2.15). The specimen was submerged in a bath with 0.9% physiologic saline solution under a controlled temperature of 37°C during the biaxial loading, while a small preload (0.5 g) was set before the displacement-driven testing protocol. A constant speed of 1 mm/min was applied to each motor to stretch the specimen under equibiaxial conditions. Two 200 N load cells recorded the force along the material directions (Di Giuseppe et al., 2019).

On the side of the intimal tissue surface, five black markers were placed to evaluate strains using a digital video extensometer placed perpendicularly to the testing area. From the marker positions, the in-plane Green strain tensor was calculated as:

$$\mathbf{E} = \frac{1}{2}(\mathbf{F}^T\mathbf{F} - 1) \tag{2.3}$$

where $\mathbf{F}$ is the gradient deformation tensor.

The first Piola-Kirchhoff stress tensor $\mathbf{P}$ was calculated from measuring loads and initial specimen dimensions so that nonzero components of $\mathbf{P}$ are:

$$P_{\theta\theta} = \frac{f_\theta}{tX_z} \tag{2.4}$$

and

$$P_{zz} = \frac{f_z}{tX_\theta} \tag{2.5}$$

where,

- f_θ and f_z are the measured loads along each direction;
- X_θ and X_z are the unloaded specimen dimensions along each direction;
- t is the average specimen thickness in the unloaded reference configuration.

Figure 2.16 shows the equibiaxial raw stress-strain from each quadrant of ATAA samples from several patients with Tricuspid Aortic Valve (TAV). Each ID number represents the data of obtained from different patients.

Figure 2.13: Specimen geometry, length and fixation. Uniaxial test. From (Sommer et al., 2013).

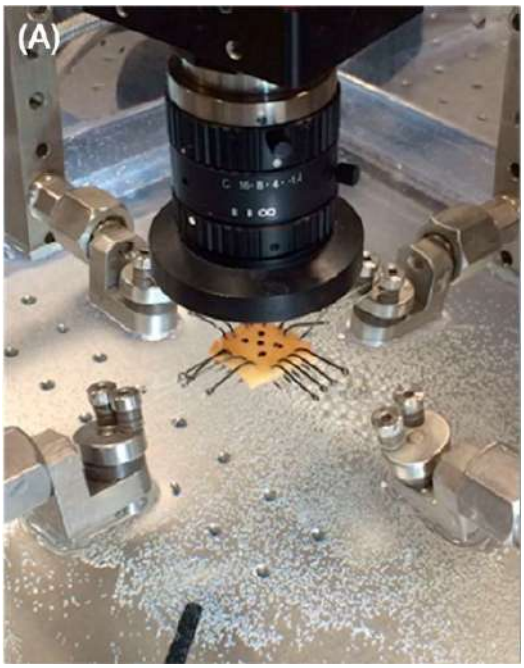

Figure 2.14: Biaxial test setup. From (Di Giuseppe et al., 2019).

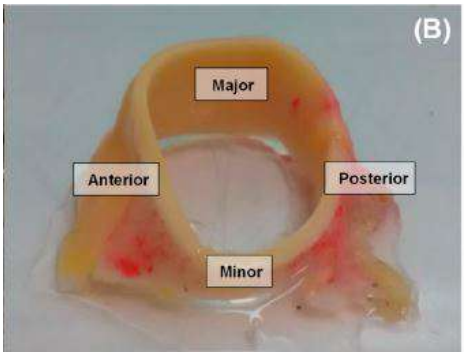

Figure 2.15: Picture of the ATAA sample with anterior, posterior, major curvature and minor curvature quadrants shown. From (Di Giuseppe et al., 2019).

2.6.3 Bulge inflation test

Davis et al. (2015) have tested a section of human ATAA with a geometry of 45×45 mm, in a bulge inflation test. As fixation, the sample is clamped in the bulge inflation device and fixed with screws, as shown in Figure 2.17.

To perform the experimental test, the specimen was inflated using a syringe pump driven at 2 $\mathrm{mL\,min^{-1}}$ to infuse water in the cavity behind the sample. The pressure was measured with a digital manometer during the test, and it was applied up to the failure of the tissue.

A speckle pattern of black paint was applied to the outward side of the specimen, allowing for the required measurements to be maid. Images of the inflating sample were collected every 3 kPa until rupture, using a DIC system composed of two cameras. A deforming NURBS mesh was extracted by morphing a NURBS template to the DIC point clouds. The NURBS surface

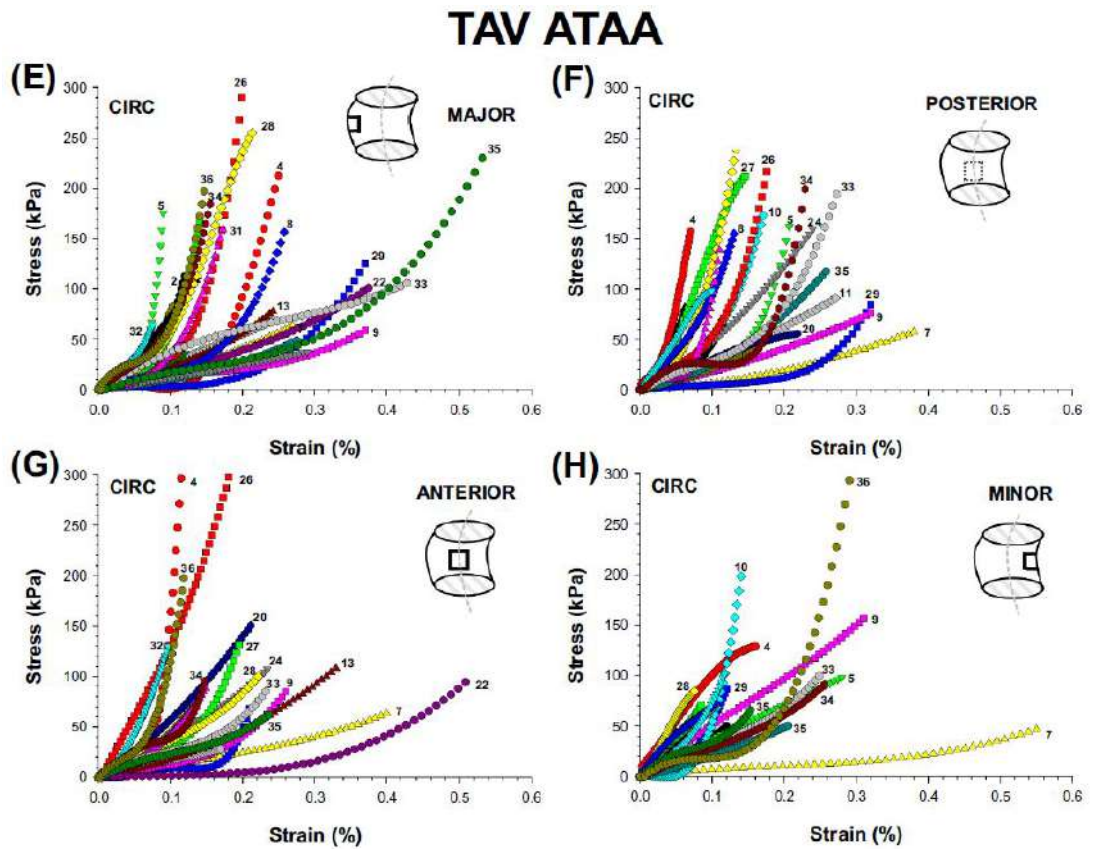

Figure 2.16: Experimental results of stress-strain data from TAV ATAA specimens from each quadrant of the aorta. From (Di Giuseppe et al., 2019).

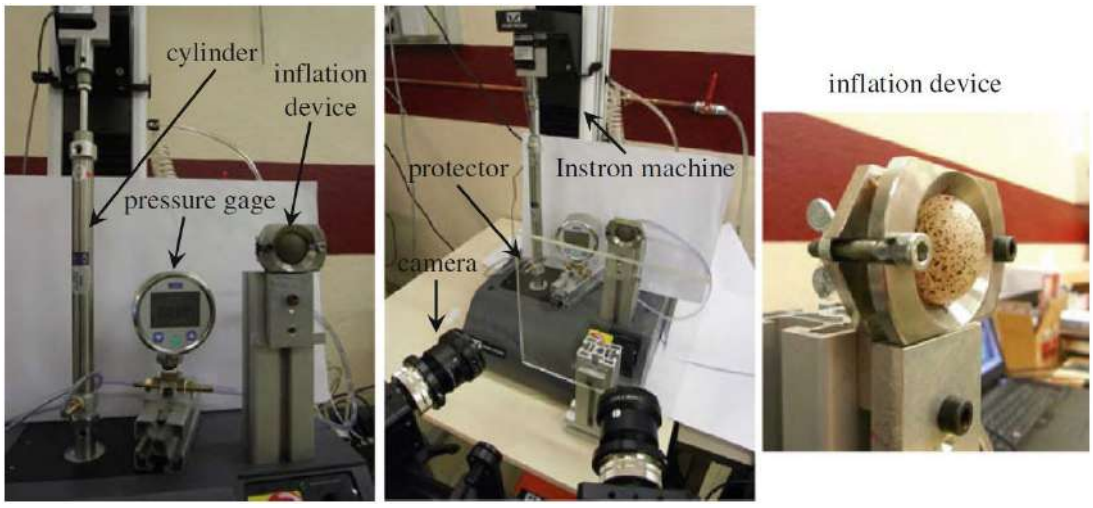

Figure 2.17: Experimental setup. From (Kim et al., 2011b).

was parameterized as a single patch containing clamped knots of 20 divisions in each parametric direction, with 22×22 control points. The positions of the Gauss points were obtained using a moving least-square method.

The surface strains were computed with the NURBS curvilinear coordinate system where the surface coordinates induce a set of convected basis vectors from which the surface deformation tensor can be obtained.

The wall stress is calculated by giving the deformed configurations and boundary conditions as inputs to the finite element model for an inverse membrane boundary value problem.

Combining the stress data with the local surface strains, the stress-strain response at every Gauss Point in the mesh is known (Davis et al., 2015).

During the bulge inflation test, the sample ruptured at 117 kPa. A deforming NURBS mesh was generated of the sample using the experimental DIC point cloud. The extracted NURBS mesh at a pressure of 117 kPa superimposed on the experimental DIC point cloud at that same pressure can be observed in Figure 2.18.

2.6.4 Shear test

Sommer et al. (2016) have tested the media of diseased human aorta using specimens with 5×4 mm and 8×3 mm for the in-plane shear test and out-of-plane shear test, respectively.

For the fixation of the samples in the experimental testing device, sandpaper and a thin consistent layer of cyanoacrylate adhesive were used to fix the specimen between two cylindrical specimen holders. To ensure a proper fixation to the holders and hardening of the adhesive, a compressive force of 0.5 N was applied to the specimens for five minutes (Sommer et al., 2013).

The triaxial shear testing device was developed and built by the Institute of Biomechanics, Graz University of Technology, Austria in cooperation with the company Messphysik Materials Testing, Fürstenfeld, Austria. During the test, the tissue is bathed in a tempered physiological solution to simulate the physiological environment of the specimen. After that, the lower platform is moved relative to the fixed upper platform with a constant speed (Figure 2.19). Once failure occurs, the applied force that led to it is defined as the shear failure force (Sommer et al., 2016).

The shear stress was calculated as the shear force divided by the sheared area. The amount of shear is the ratio of the relative in-plane displacement of two parallel plates to their separation distance. A total of 16 samples were tested, between them 9 aneurysmatic, 3 aneurysmatic with Connective Tissue Disorder (CTD), and 4 dissected. Shear modes in the $z\theta$ plane are referred to as “in-plane” shear modes, and the rz and $r\theta$ planes as “out-of-plane” shear modes (Figure 2.20). Figure 2.21 shows the “in-plane” shear stress vs. the amount of shear behaviour obtained from the tested specimens.

2.6.5 Extension-inflation test

Sommer et al. (2013) have performed an extension-inflation test on a fresh intact ovine esophagus tube segment with an 80-90 mm length.

As shown in figure 2.22, the sample was cannulated at both ends with specially designed tube

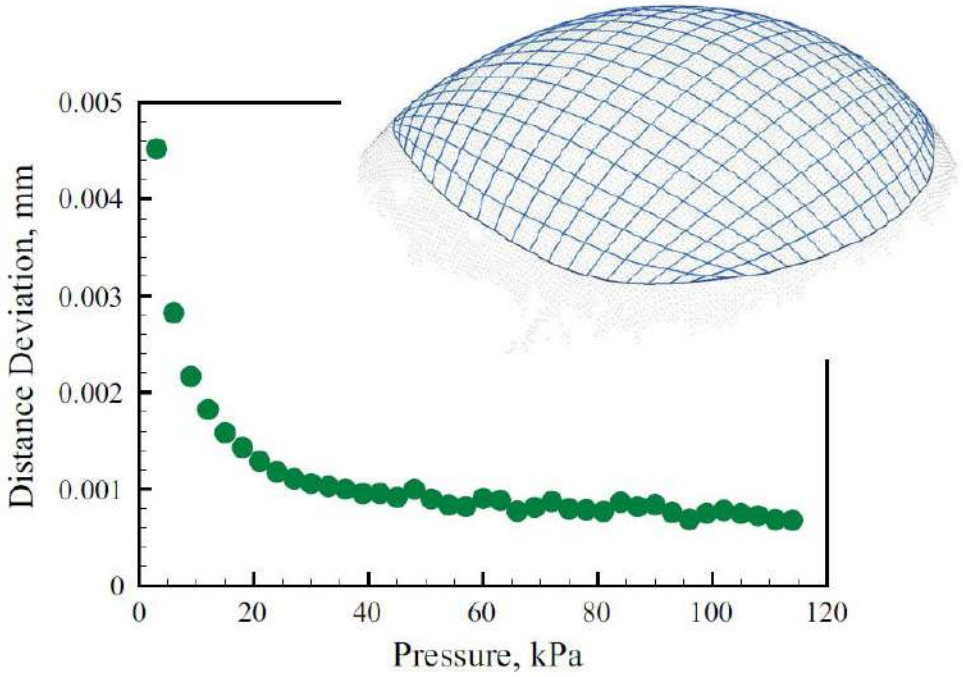

Figure 2.18: NURBS mesh along with a plot of the distance deviation. From (Davis et al., 2015).

connectors matching the inner diameter of the esophagus. The specimen was glued and fixed with a cord to the tube connectors, to avoid slippage (Sommer et al., 2013).

Tests with continuous recording of the inflation pressure, axial force, outer diameter, and gage length were performed at pressures ranging from 0 to 2 kPa at several axial pre-stretches $\lambda_z = l_z/L_z$, ranging from 1.1 to 1.4 in increments 0.1, where l_z denotes the gage length (distance of the two markers) in the axially stretched and pressurized tube, and L_z denotes the corresponding length in the unloaded (reference) state. At each increment of λ_z, preconditioning was applied by performing five axial elongation cycles ($l_z = 1$ mm min^{-1}), ranging from the unstretched condition to the desired axial pre-stretch. Held at the fifth cycle, it was then preconditioned circumferentially by performing 10 inflation-deflation cycles, from 0 to 2 kPa at 10 kPa min^{-1}. The specimen was inflated and deflated one final time, to perform a "measurement cycle", yielding the recorded raw data for further analysis. The test was conducted in Phosphate-Buffered Saline (PBS) with Ethylene Glycol Tetraacetic Acid (EGTA) (0.1 g L^{-1}) at 37°C. The thickness of the specimen was obtained by cutting the tube at the gage region and opening it radially, then measuring it with a video-extensometer (Sommer et al., 2013).

The intact segment of the esophagus is considered to be an incompressible thick-walled cylindrical tube, subjected to extension and inflation under the assumption of no torsion. The current configuration of the cylindrical coordinates (r, θ, z) of the specimen can be described using:

$r_i \leq r \leq r_0, \quad 0 \leq \theta \leq 2\pi, \quad 0 \leq z \leq l_z$, with:

$$r_i = \sqrt{r_0^2 - \frac{R_0^2 - R_i^2}{\lambda_z}} \tag{2.6}$$

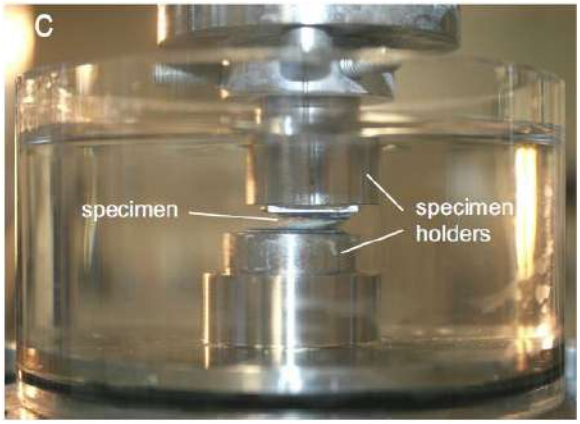

Figure 2.19: Shear test setup. From (Sommer et al., 2016).

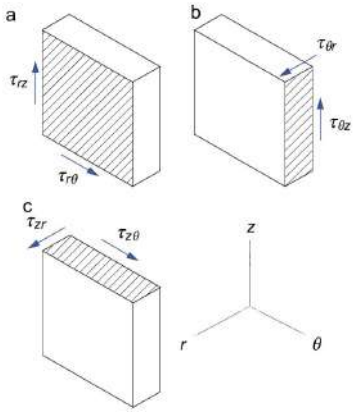

Figure 2.20: Shear mode planes. From (Sommer et al., 2016).

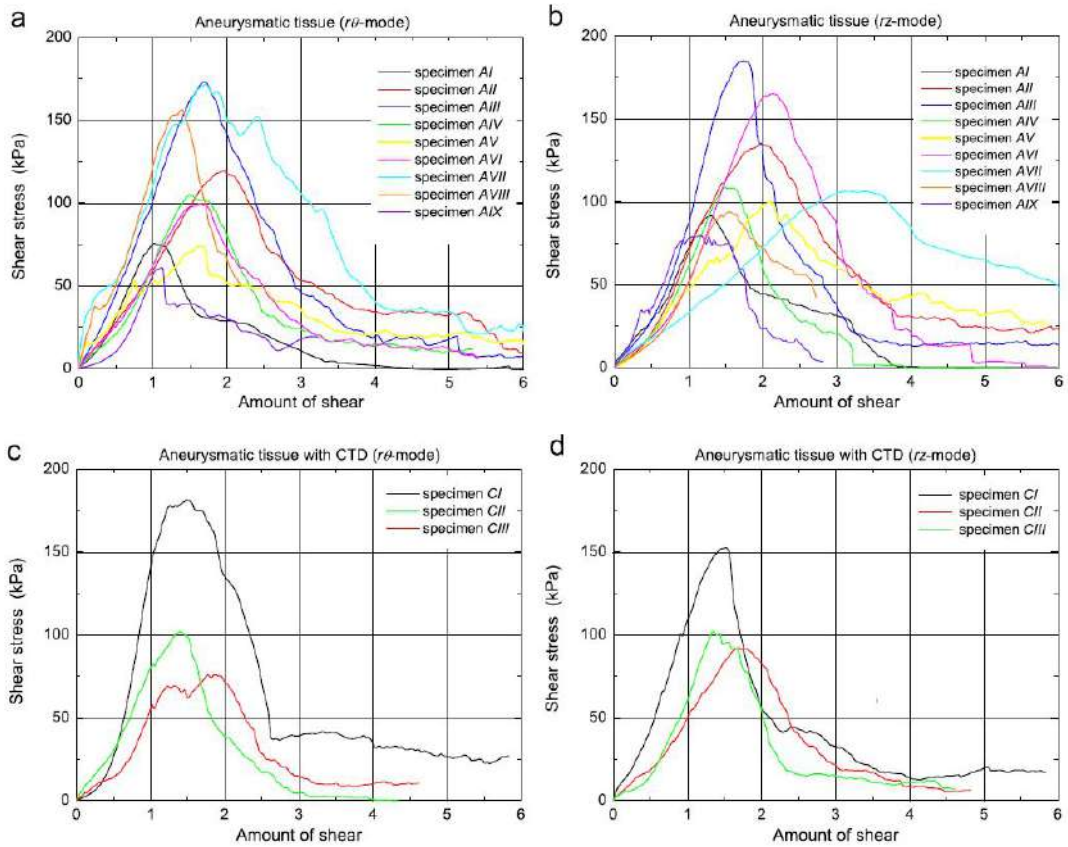

Figure 2.21: Shear stress vs. amount of shear for different tested samples. From (Sommer et al., 2016).

Figure 2.22: Specimen fixation and length demonstration. From (Sommer et al., 2013).

where,

- r_i is the inner radius;
- r_θ is the outer radius;
- $\lambda_z = l_z/L_z$ is the measured axial stretch.

The load-free inner radius is:

$$R_i = R_0 - t \tag{2.7}$$

where t is the unloaded wall thickness, and R_0 is the load-free outer radius.

The internal pressure pi can be obtained in the form (Holzapfel et al., 2000):

$$p_i = \int_{r_i}^{r_0} (\sigma_{\theta\theta} - \sigma_{zz}) \frac{dr}{r} \tag{2.8}$$

where,

- $\sigma_{\theta\theta}$ denotes the Cauchy stress in the circumferential direction;
- σ_{rr} denotes the Cauchy stress in the radial direction.

The measured axial force is obtained in the form:

$$F_z = \pi \int_{r_i}^{r_0} (2\sigma_{zz} - \sigma_{\theta\theta} - \sigma_{rr}) r \, dr \tag{2.9}$$

The inflation pressure and the axial force were plotted as functions of the circumferential ($\lambda_\theta = r_0/R_0$) and axial stretches (λ_z) of the tube, for the different applied axial pre-stretches ($\lambda_z = 1.1$ to 1.4) (Figure 2.23). At these mentioned pre-stretches, the mean and related standard deviation of the maximum circumferential (λ_θ) and axial stretches (λ_z) of the previous pressurizing cycles can be observed in Table 2.1.

2.7 Conclusions

In this chapter, an introduction to the anatomy of the aorta was given from an engineering perspective. The importance of a biomechanical approach to understand the aortic aneurysm has been discussed. One of the major issues of modeling the biomechanical behaviour of biological tissue is its heterogeneity since both the mechanical properties and the thicknesses can vary on a millimeter scale, thus the importance of a testing device that can evaluate the intended section of the artery, in this case, where an aneurysm has occurred, as a whole. Assuming a constant thickness throughout the whole anatomical piece is a common choice when performing mechanical tests and FE analysis due to the difficulty of the measurement of this parameter, and because it facilitates the computational calculation.

With the aid of imaging techniques, it is possible to obtain a patient-specific 3D model which will allow for the virtualization of the anatomical piece. These techniques can also provide essential information on performing FSI analysis coupling Computational Fluid Dynamics (CFD) and Computational Solid Mechanics (CSM).

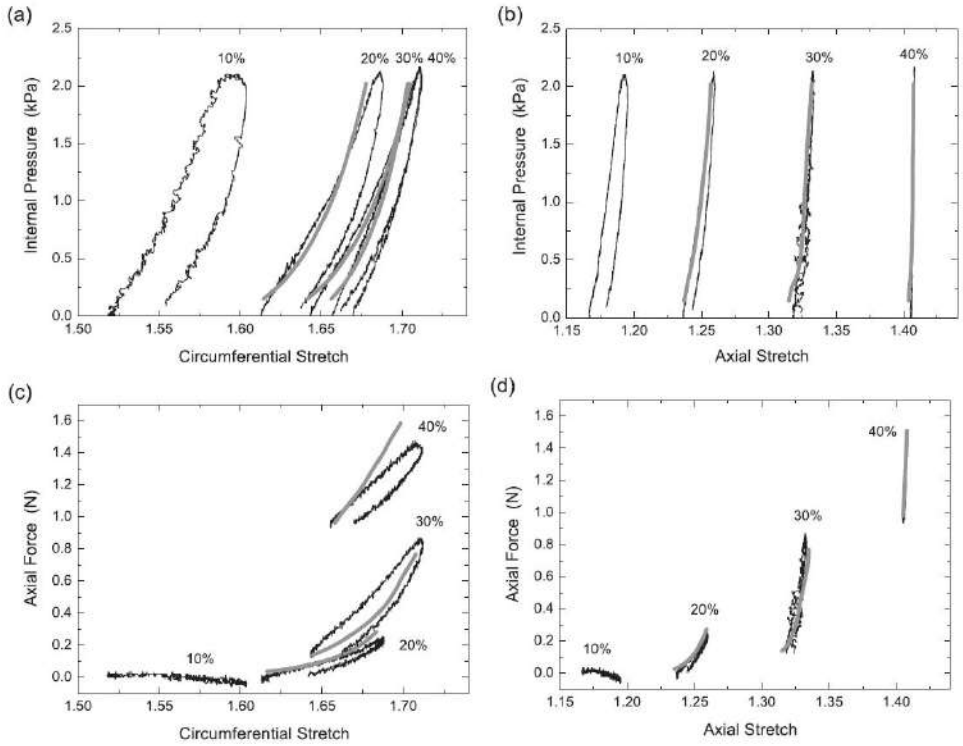

Figure 2.23: Extension-inflation responses of preconditioned intact esophagus wall. Internal pressure is plotted against the circumferential (a) and axial stretch (b). In a similar manner, the axial force is plotted against the circumferential (c) and axial stretch (d). The various pre-stretches are labeled as 10, 20, 30 and 40%. From Sommer et al. (2013).

Table 2.1: Maximum circumferential and axial stretches during inflation tests at different pre-stretches. From Sommer et al. (2013).

Axial pre-stretch	**Circ. stretch**	**Axial stretch**
1.1	1.51 ±0.14	1.17 ±0.12
1.2	1.53 ±0.23	1.21 ±0.06
1.3	1.56 ±0.19	1.33 ±0.05
1.4	1.57 ±0.19	1.40 ±0.01

The protocol for performing experimental tests on biological tissue of the aorta were systematically reviewed. Details regarding the storage and handling of the tissue specimens, conditions on which the tests were performed, and analysed were given. Tests have been typically carried out on small samples of tissues, tests by tensile, biaxial or inflation loading conditions.

3 Design of a testing device for an aortic aneurysm piece

3.1 Introduction

In order to bring insights in understanding the biomechanical behaviour of the aorta tissue, it is essential to perform experimental tests. Besides, this data is fundamental to carry out computational analysis taking into account a patient-specific medial approach. In the previous revision chapter, several test methods were overviewed and described in terms of biological tissue handling, test protocols and data analysis. Typically, a common denominator among these methods is the fact that they perform experimental tests over a section or relatively small part of the anatomical TAA tissue. In this chapter a new protocol is aimed by assuming a test configuration that considers a whole piece of the TAA. In particular, the design of an experimental testing device that fulfills such needs will be developed. The Axiomatic Design (AD) Theory will be considered during the development of the device, which will allow for the concept design process to be clearer and more methodical, and overall more efficient.

3.2 Axiomatic Design principles

AD Theory, developed by Nam Pyo Suh, was motivated by the conclusion that many technological and social problems have been created through poor design practice. Worldwide famous catastrophes like the Union Carbide chemical plant incident in Bhopal, the nuclear power plant accident in Chernobyl, and the failure on NASA Challenger Space Shuttle were caused by engineering design failures. The goal of this theory is to establish a scientific basis for design by providing a theoretical foundation, instead of doing it empirically on a trial-and-error basis. AD can be applied in the design of products, processes, systems, or materials. In AD, design is an interplay between "what we want to achieve" and "how we want to achieve it". It is based on a functional thinking approach and it holds four domains:

- Customer domain;
- Functional domain;
- Physical domain;
- Process domain.

The customer domain comprises the attributes or needs (CNs) that the customer is looking for, and may often not be clearly defined or with a non-technical language. The functional domain comprises the functional requirements (FRs), which are expressed in a neutral language

and are derived from the CNs, and constraints (Cs), which are limitations. The physical domain consists of the design parameters (DPs) in the physical form to satisfy the FRs. Finally, the process domain describes the processes of realization of the DPs by process variables (PVs). The mapping process between two domains occurs when the aspects of the following domain are defined according to the characteristics of the previous one. This "zig zag" process happens when we define the FRs of a certain level and then define the DPs that satisfy them. By asking the simple question "why?" after we obtain the DPs, and then answering it, we obtain the next level FRs. This process repeats itself as many times as necessary until we reach the desired amount of detail (Figure 3.2).

Axiomatic design theory is composed of 2 axioms, 26 theorems, and 8 corollaries. The design axioms are the following:

- Axiom 1: The Independence Axiom – Maintain the independence of the functional requirements.
- Axiom 2: The information Axiom – Minimize the information content of the design.

The first axiom implies that when designing a complex machine, the FRs should be independently satisfied by DPs selected by the designer. The second axiom means that in the existence of multiple designs that satisfy the first axiom, the one with minimum information content should be selected, thus increasing the probability of success. The later aims to view the system from a statistical perspective. The information content can be calculated by using the probability density function, if the range for the design is the design range, and the operating range of the designed product is the system range, then a common range ca be defined as the area between the design range and system range (Figure 3.1). Based on the second axiom, the design should be directed to increase the common range (Park, 2007).

The probability that the system range satisfies the design range is defined in Equation 3.1. The information content is defined in Equation 3.2.

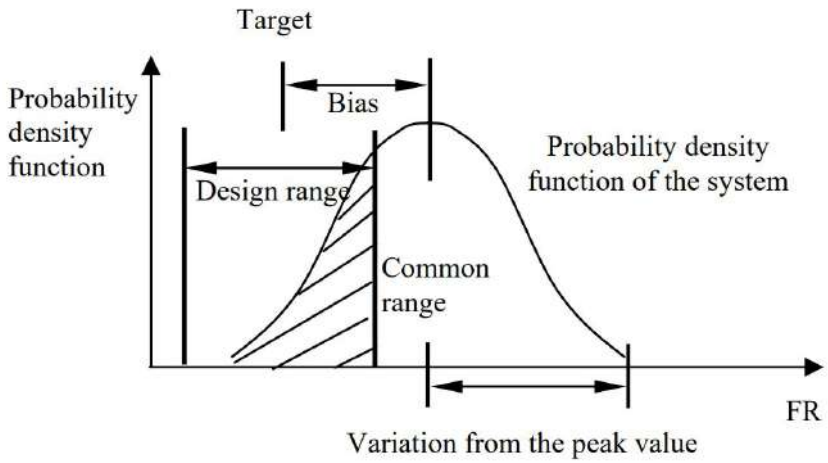

Figure 3.1: Schematic view of the calculation of the information content. From (Park, 2007).

$$p_s = A_{cr}/A_{sr} \tag{3.1}$$

$$I = -\log_2(A_{cr}/A_{sr}) \tag{3.2}$$

where A_{cr} is the common range and A_{sr} is the system range.

In the design process, the information in each domain is decomposed and organized into a hierarchy (Figure 3.3).

Based on the Independence Axiom, the designed matrix can be defined, which will be based on the dependencies and relationships between FRs and DPs. Xs on the matrix means that there is a relationship, while 0s mean that there are no relationships or dependencies. Design matrices can be uncoupled, decoupled, or coupled. Uncoupled designs (Eq. 3.3) are the most desirable, they are characterized by a diagonal matrix meaning that a change to a DP only affects its corresponding FR and no other.

$$\begin{Bmatrix} FR1 \\ FR2 \\ FR3 \end{Bmatrix} = \begin{bmatrix} X & 0 & 0 \\ 0 & X & 0 \\ 0 & 0 & X \end{bmatrix} \begin{Bmatrix} DP1 \\ DP2 \\ DP3 \end{Bmatrix} \tag{3.3}$$

A decoupled design (Eq. 3.4) is acceptable, it is characterized by a triangular matrix (lower or upper), and they translate the fact that a change to a DP will only affect its FR and all the lower (or upper).

$$\begin{Bmatrix} FR1 \\ FR2 \\ FR3 \end{Bmatrix} = \begin{bmatrix} X & 0 & 0 \\ X & X & 0 \\ X & 0 & X \end{bmatrix} \begin{Bmatrix} DP1 \\ DP2 \\ DP3 \end{Bmatrix} \tag{3.4}$$

A coupled design (Eq. 3.5) is characterized by having a design matrix with X's above and below the diagonal and is discouraged because a change to a DP will affect its FR and others in the system.

$$\begin{Bmatrix} FR1 \\ FR2 \\ FR3 \end{Bmatrix} = \begin{bmatrix} X & X & 0 \\ X & X & X \\ X & 0 & X \end{bmatrix} \begin{Bmatrix} DP1 \\ DP2 \\ DP3 \end{Bmatrix} \tag{3.5}$$

3.3 Testing device - Axiomatic approach

Having in consideration AD, the first step would be to know the CNs. Since the experimental device will be integrated into a larger research project and does not have as its destiny to be commercialized or mass-produced, the attribution of the CNs will be skipped because the initial needs of the device will already be defined with technical and neutral language, thus beginning the design approach with FRs. Although the DPs will be presented on this section, a more accurate descriptions of the mechanical parts that will comprise the overall testing device will be presented more ahead.

The first level FRs are:

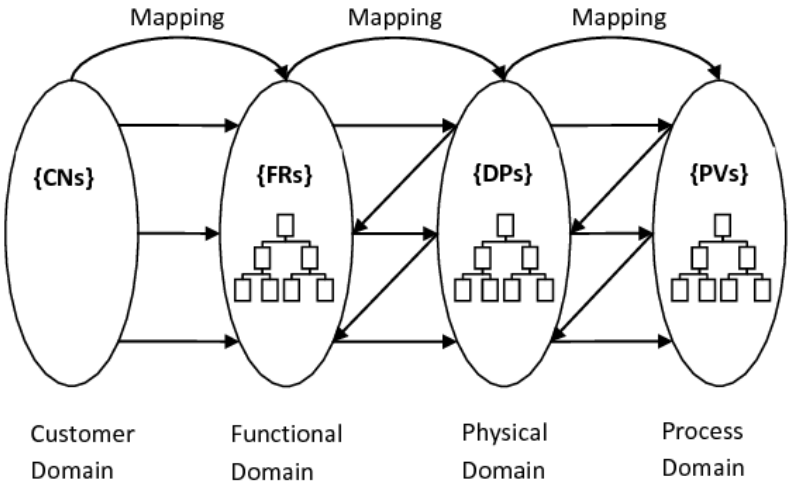

Figure 3.2: Axiomatic Design domains and mapping. From Dagman and Söderberg (2012).

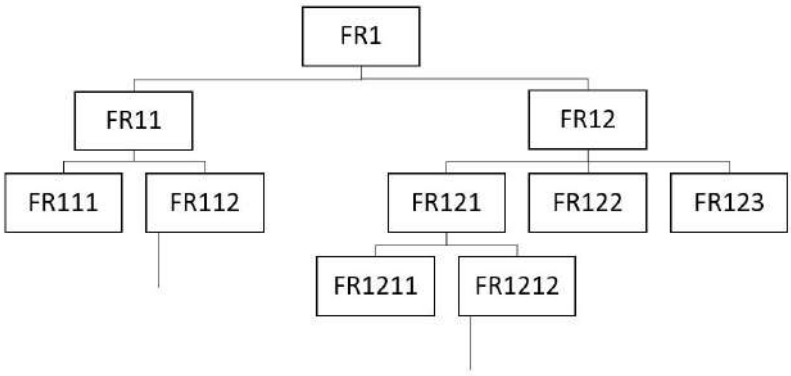

Figure 3.3: Decomposition of a FR.

- FR1: Perform mechanical tests on an anatomic part
- FR2: Measure values

The corresponding DPs can be defined as:

- DP1: Mechanical devices
- DP2: Measuring systems

To perform mechanical required mechanical tests on the specimen, specific conditions must be assured. The mechanical devices within the main experimental device will secure the subject by fixing it on both ends and inflate it with a liquid. Because the ATAA can be compared with a tubular shape with a curvature, the mechanisms will allow for this curvature to be maintained during the entire testing procedure, thus avoiding any parasitic tensions on the surface. To allow for a more organized development and to make sure all the requirements have a corresponding solution, the device will be separated in modules.

The fixation of the specimen will be assured by the fixation module, which comprises parts that guaranty the passage of liquid to the specimen, ensure liquid sealing, and allow for no

displacements at both ends. The inflation module will be responsible for applying the pressurized liquid, transporting it throughout the circuit and draining it from inside the subject. The alignment module allows for one of the fixation ends to be properly adjusted to meet with the plane parallel to the section that has been cut from the aorta, and at the same time permits to vary the distance between fixation parts. The last module can yet be divided into two sub modules, the plane adjustment module and the extension module. Finally, the rotation module will allow for the alignment module to be locked once the alignment requirements are fulfilled and rotate the subject in a way that maintains the same pressure state throughout one complete rotation.

The measuring system comprises of a pressure gauge, a set of digital cameras, and a speckle pattern on the outside surface of the specimen. These will measure the internal pressured being applied at a certain point of the experiment, and record the displacements of the pattern so that the DIC software extracts biomechanical parameters from the tested subject.

This way, the first level FRs presented earlier in this section can be decomposed into the following:

- FR1: Perform mechanical tests on an anatomic part
    - FR11: Hold the specimen on the device
        - FR111: Ensure liquid sealing
        - FR112: Ensure 0 displacements at fixation zone
        - FR113: Ensure passage of liquid to the specimen
    - FR12: Inflate the specimen
        - FR121: Pressurize liquid
        - FR122: Transport liquid throughout the circuit
        - FR123: Drain the liquid from the circuit
    - FR13: Maintain natural curvature of the aneurysm
        - FR131: Adjust alignment of both fixation parts
            - FR1311: Linearly shift the fixation part's revolution axis
            - FR1312: Allow for fixation parts' axes to become non-parallel
        - FR132: Vary the distance between fixation ends
    - FR14: Maintain the same tension state during rotation
        - FR141: Lock the rotation module
        - FR142: Rotate fixation ends around a common axis
- FR2: Measure values
    - FR21: Measure the internal pressure
    - FR22: Observe the specimen's external surface
        - FR221: Hold the camera in place

        - FR222: Make the external surface's displacements visible
        - FR223: Register displacements on the tissue's surface
        - FR224: Interpret 3D displacements

The corresponding DPs are:

- DP1: Mechanical devices
    - DP11: Fixation module
        - DP111: Proper tightness
        - DP112: Proper friction coefficients
        - DP113: Hollow clamping system
    - DP12: Inflation module
        - DP121: Syringe pump
        - DP122: Plastic tubes
        - DP123: Drain valve
    - DP13: Alignment module
        - DP131: Plane adjustment module
            - DP1311: Slot with sliding pin
            - DP1312: Hinge pin
        - DP132: Extension module
    - DP14: Rotation module
        - DP141: Threaded ends on pins
        - DP142: Aligned rotation shafts
- DP2: Measuring systems
    - DP21: Pressure gauge
    - DP22: Image acquisition and analysis system
        - DP221: Tripod
        - DP222: Speckle pattern
        - DP223: Digital camera
        - DP224: DIC software

The decomposition to lower levels and mapping between FRs and DPs can be observed on Figures 3.4 to 3.9.

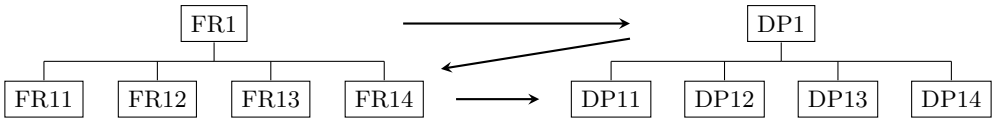

Figure 3.4: Mapping and decomposition to second level of FR1 and DP1.

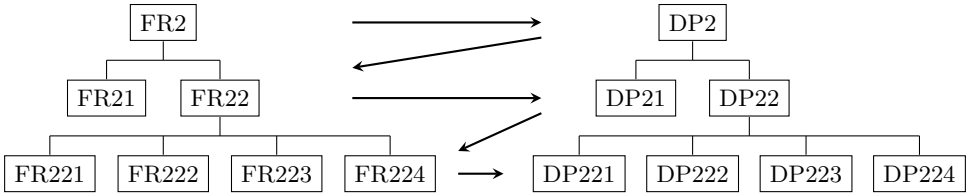

Figure 3.5: Mapping and decomposition of FR2 and DP2.

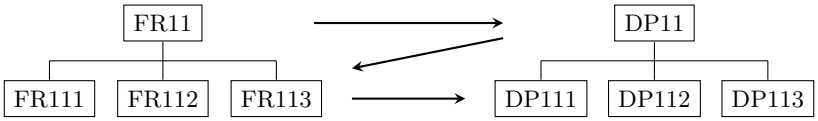

Figure 3.6: Mapping and decomposition of FR11 and DP11.

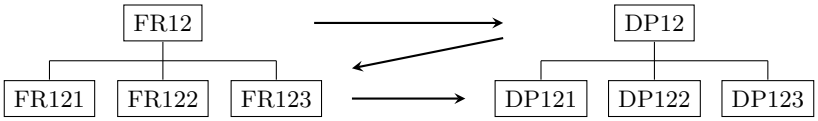

Figure 3.7: Mapping and decomposition of FR12 and DP12.

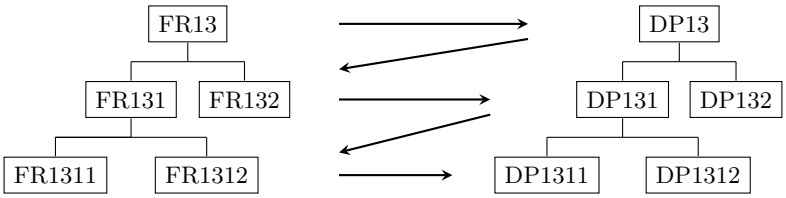

Figure 3.8: Mapping and decomposition of FR13 and DP13.

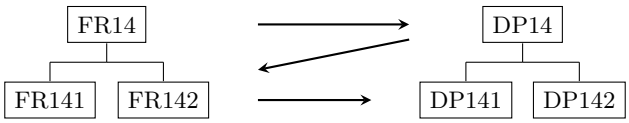

Figure 3.9: Mapping and decomposition of FR14 and DP14.

Once chosen the FRs and DPs, it is now possible to assemble the design matrix (Figure 3.10.), which will enlighten on the relationships between FRs and DPs and allow for a qualitative classification of the design. In the qualitative design matrix, Xs will indicate there is a relationship, and 0s will indicate there is no relationship. A blank space on the matrix will represent a parent-child relationship.

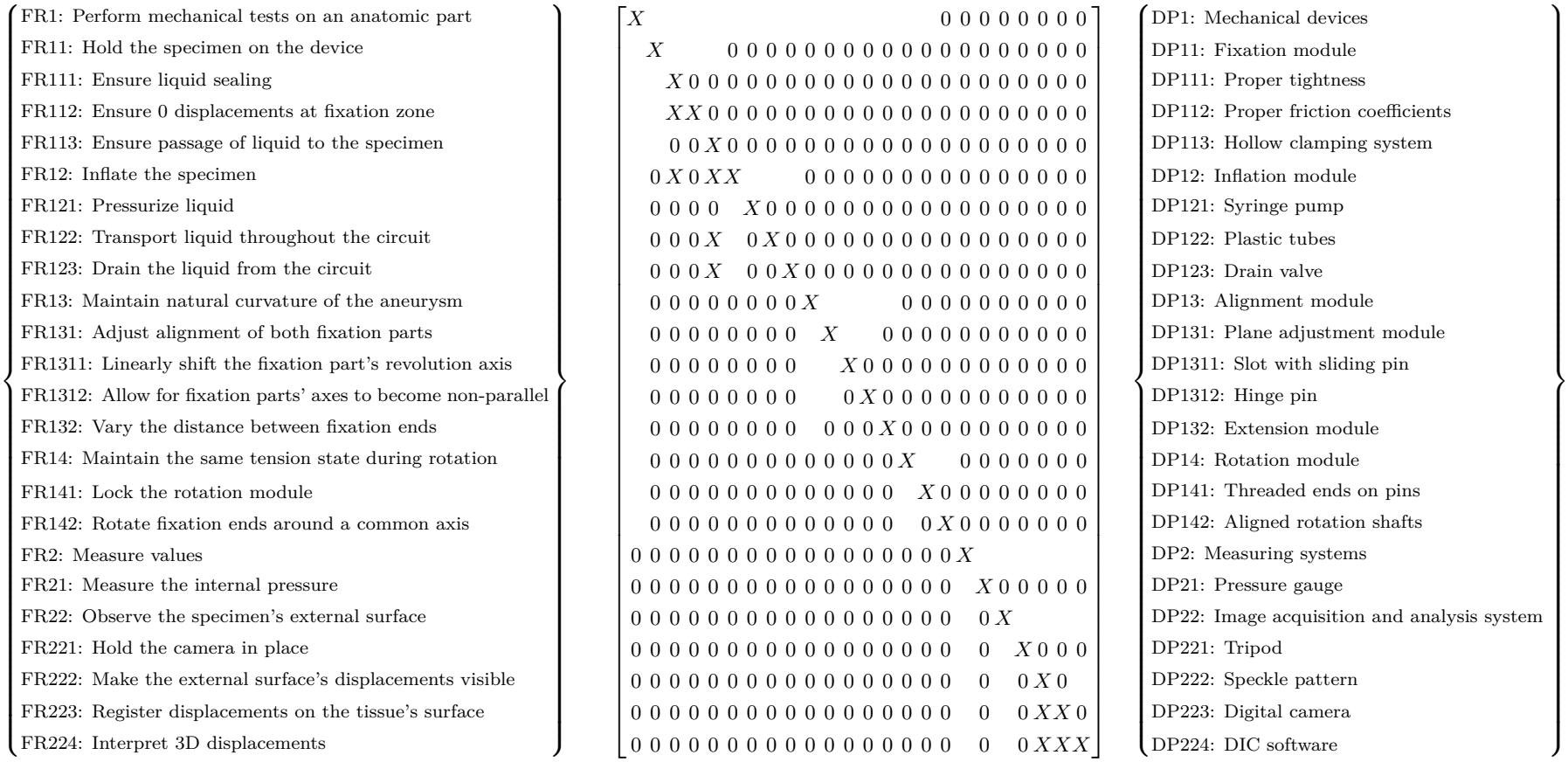

Figure 3.10: Design matrix of the experimental testing device.

The design matrix is a lower triangular matrix, meaning that the design is decoupled. By analyzing the relationships between FRs and DPs, there are found 8 more than the desirable ones, which would be 24 (Same number of FRs and DPs).

FR112 is not only dependent of DP112, but also DP111 because to ensure that the specimen's ends are properly fixed and no displacements occur during the inflation, not only it is necessary to guaranty adequate friction coefficients, but also proper tightness. FR12 has additional dependencies to DP113 and DP111, this happens because by changing the hollow clamping system and proper friction coefficients the successful inflation of the specimen can be compromised. FR122 is dependent of DP113 because the hollow clamping system will allow for the liquid to flow inside the specimen, and by changing this system, FR122 would be affected too. For a similar reason as the previous, FR123 is dependent of DP113, but on this case the hollow clamping system is related to the draining of the liquid from inside the specimen. FR223 and FR224 both have dependencies of DP222, due to the fact that the speckle pattern affects both the registration of the tissue's external surface's displacements and its interpretation. FR224 is also dependent of DP223 because the device observing and tracking the speckle pattern is essential to further on interpret the 3D displacements using an adequate software.

3.4 Fixation Module

After an ATAA is surgically removed, it is replaced by a flexible material with a tubular shape that tries to mimic the behavior of the aorta. These materials are provided with different section diameters, from 26 to 34mm. The diameter chosen for the replacing of the removed aorta segment is the one that will be closer to the patient's aorta.

The expected testing subject will have a tubular shape with an approximately circular section. The fixation part, which will be in contact with the test specimen, is designed with a circular section (Figure 3.11b) to allow the subject to best accommodate itself to the fixation, furthermore, its diameter will be 26mm to easily fit aneurysms with different diameters. The subject is placed in a way enabling it to wrap around the fixation part (Figure 3.12a) in a length between 4 to 5 mm. Afterward, a thin band of rubber or silicone-based material with approximately 3 mm of width is placed around the biological tissue (Figure 3.12b) so that the plastic zip tie pressing on top of it (Figure 3.12c) does not have direct contact with the biological tissue, thus avoiding any damage. A continuous cylindrical shape of the fixation part would most likely provoke slippage of the test subject during inflation. This, way a groove is inserted on the part where the silicone/rubber band and zip tie will be (Figure 3.11a) so that this risk is decreased significantly. The groove is machined at 1.5mm from the edge of the fixation part to reduce the unusable length of the test specimen due to the need to fix it. The tightening force of the zip tie should be enough to avoid slippage or leaking without crushing the subject. This fixation procedure repeats itself on the opposite side of the testing device, thus ensuring a properly tight fixing that is leakage-proof and allows for the subject to be freely inflated.

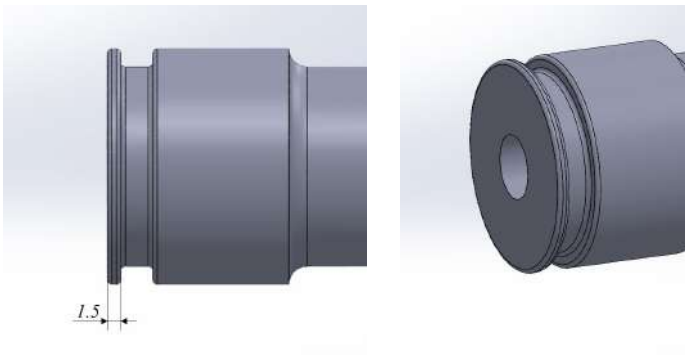

(a) (b)

Figure 3.11: Fixation part. (a) A groove is machined on the fixation part, to accommodate the silicone/rubber band and the zip tie. (b) Fixation part's section in perspective.

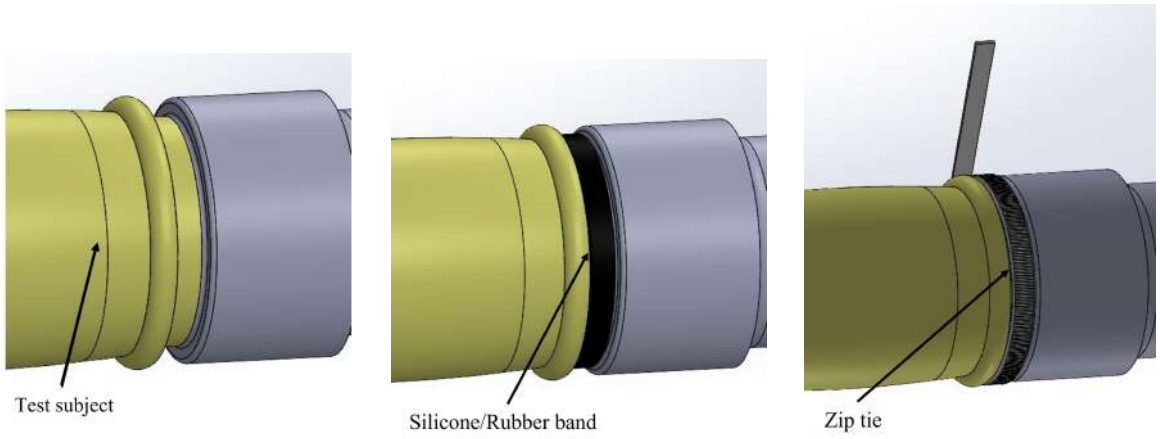

(a) (b) (c)

Figure 3.12: Demonstration of test subject's fixation sequence. (a) Test subject wrapped around the fixation part. (b) Protective silicone/rubber band around test subject. (c) Zip tie tightening the band and the subject.

3.5 Inflation Module

The inflation module consists of a connector block, tube connector, radial shaft seal, fixation part, fixation part blocker, plastic tubes, and a syringe pump. The main part, the connector block (Figure 3.13a), guarantees the connection of all the separate parts to make a single mechanical body. It will also allow for the connection and enabling of the extension module, which will be addressed further on.

The inflation of the specimen with a liquid will be provided by a syringe pump. Plastic tubes will be connected both to the syringe pump and to tube connectors on both the inlet (Figure 3.13) and outlet (Figure 3.14) side of the device. A hole made on the top face and up to the center of the connector block, with an initial threaded length, allows for the assembly of the tube connector and the passage of liquid from it to the fixation part. The hole made through the outlet fixation part has a thread, so a similar tube connector can be placed. The assembly sequence of the inflation's module inlet side can be observed in Figure 3.13. Between the syringe pump and the tube connector, on the inlet side, a pressure gauge will be placed to measure the

applied pressure.

3.6 Alignment Module

As mentioned before, the ascending aorta has a natural curvature (Figure 3.15). ATAAs develop themselves in the course of the curvature, meaning that the biological piece that is surgically removed won't have parallel end planes.

To maintain the angle between both ends, the device will have a "fixed" end (which only allows for linear movement) and an adjustable end (Figure 3.16a). The adjustable end can perform radial movement and rotate around an axis perpendicular to the top plane of the device, allowing for an angle to be created between both ends (Figures 3.16b and 3.16c). A slot and a sliding pin will endow the mechanism its axial movement, the pin has a threaded end so that it can be tightened after a specific displaced length. The "hinge pin" will allow for a hinge type of movement.

To accommodate itself to the test subject's length, the device will rely on a rolled ball screw, which is composed of a threaded shaft, a nut, and rolling elements (composite ball inserts in this case). First, the nut is fixed to the connector block and its rotary movement is prevented, secondly, the threaded shaft is inserted inside the nut and is constrained on both ends by retaining rings to prevent axial movement. By turning the shaft, rotary action is transformed into linear motion by the aid of the ball inserts, thus allowing the connector block to move forward and backward (Figure 3.17a). To avoid the rotation of the connector block due to its weight, linear ball bearings are connected to "L" shaped "arms" on each side of the connector block, the bearings will slide on two shafts that are fixed on the workstation. These bearings allow for two parts in contact and with relative movement to have significantly lower friction coefficients between them.

After the desired configuration is locked, the device is then ready to inflate the test specimen.

3.7 Rotation Module

After the test subject is inflated to a certain pressure, digital cameras will register the current position of the speckle pattern on the surface. Because the cameras will be placed only on one side of the device and will be stationary, the specimen will need to rotate for the whole outer surface to be observable.

For the rotation not to provoke any unwanted surface tensions on the specimen, both ends will rotate around a common axis and at the same angular velocity. For the rotation to be successful, the fixation and alignment mechanisms on the outlet side will rotate as a whole with the aid of a specifically designed shaft, the "outlet shaft", connecting the mechanisms, that will be concentric with the fixation part on the inlet side. The outlet shaft will be assembled on a sleeve bearing for a low-friction rotation, and its axial movement will be prevented by retaining rings (Figure 3.18).

On the inlet side, as the fixation part is assembled on the connector block and restrained of axial movement because of the locker, a clearance between the two parts will allow for the fixation

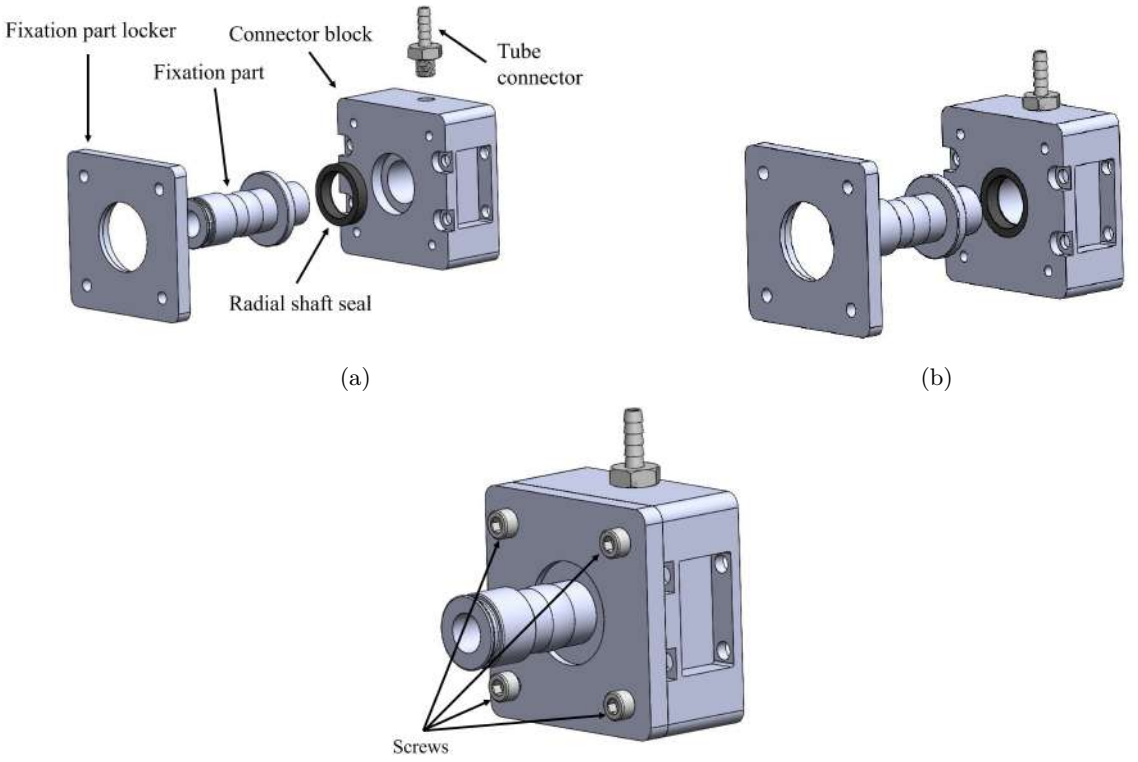

Figure 3.13: Inlet side of the inflation module. (a) Module's different components. (b) Radial shaft seal is inserted in the bore, fixation part is aligned with the hole on the connector block and with the seal. (c) Fixation part is inserted in the hole of the seal, fixation part blocker is screwed to the connector block to hold the fixation part.

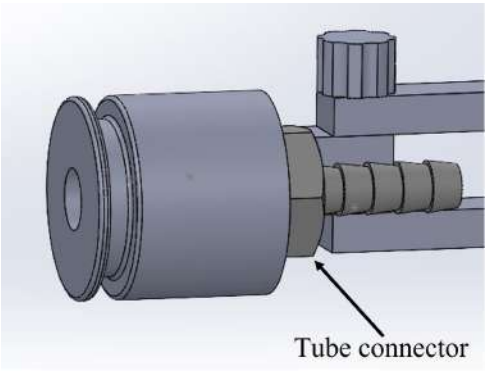

Figure 3.14: Outlet side of the inflation module. Plastic tubes attached to the tube connector allow for the liquid to drain from inside the test specimen.

part to rotate with minimal effort. The radial shaft seal, designed to sit between rotating and stationary components, also guarantees a relative movement between the parts with low friction forces.

The rotation of both the outlet shaft and the fixation part will be held by a flat belt transmission (Figures 3.18 and 3.19), with approximately 10mm belts (Figure 3.20b). A convex shape machined on both the outlet shaft (Figure 3.20c) and the inlet fixation part (Figure 3.20a) will host the belts. The belts on both sides will be connected to a common shaft designed to hold

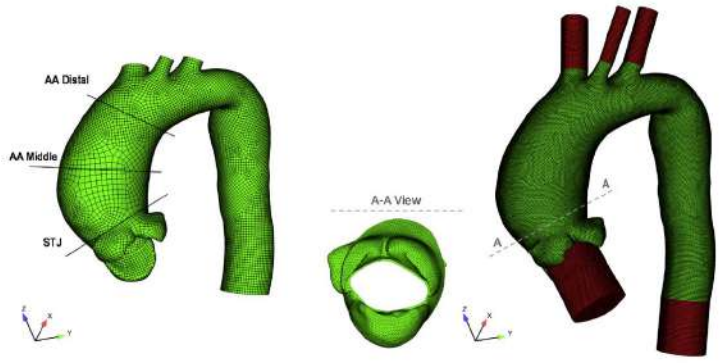

Figure 3.15: Representative FE analysis mesh reconstruction of a patient specific ATAA. The curvature of the aneurysm can be observed. From Mendez et al. (2018).

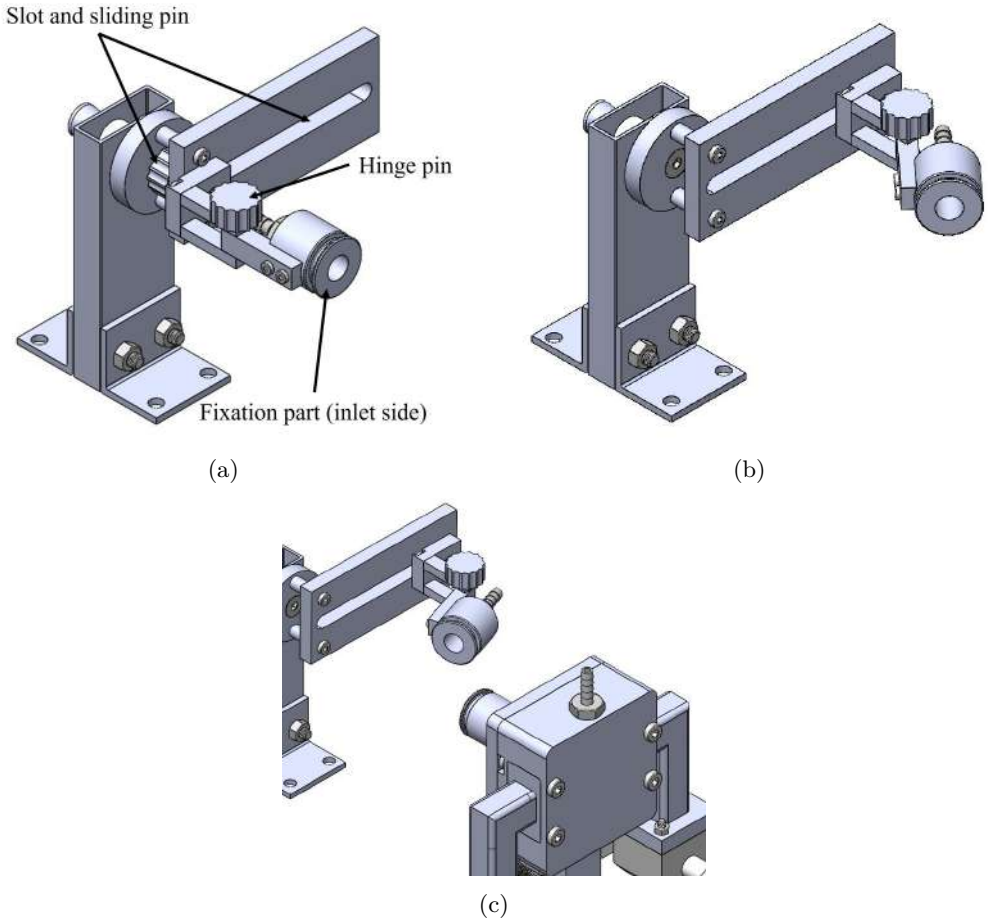

Figure 3.16: Alignment module. (a) The outlet fixation part's initial position is aligned with the inlet fixation part. (b) The pretended configuration is set and the sliding pin and hinge pins are tightened to lock the position.(c) An angle is created between both fixation part's front faces.

them. This shaft will be assembled on the workstation by two-shaft blocks on which sleeve bearings will be assembled, endowing the shaft with a low-friction rotary movement (Figure 3.21). Again, retaining rings will restrict the shaft of axial movement, and a knob fixed to the shaft will enable a manual rotation. To lock the specimen rotation shaft during inflation, and to unlock it during the rotation, a wing screw can be tightened and loosened, respectively.

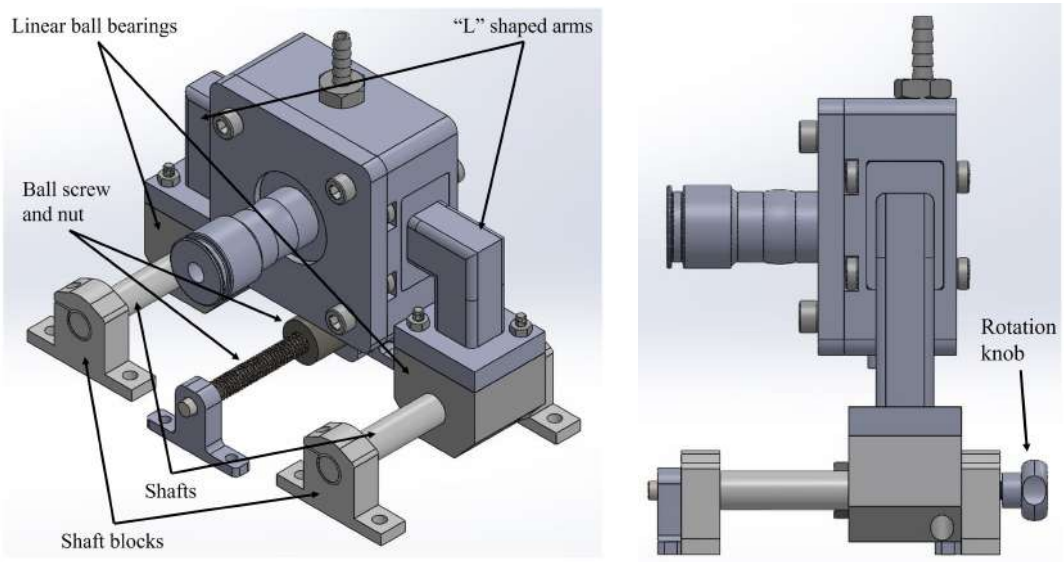

(a) (b)

Figure 3.17: Extension mechanism. Allows for the inlet fixation part to have movement in the direction of the outlet fixation part. (a) Shaft blocks hold the shafts in place and are screwed to the workstation. (b) The knob connected to the screw allows for the manual rotation.

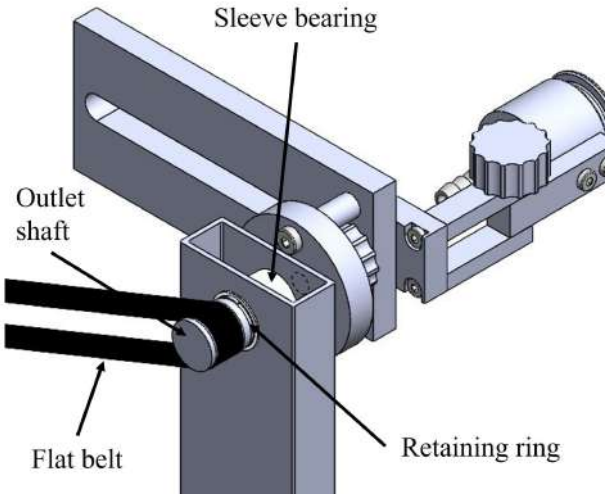

Figure 3.18: Flat belt connected to the outlet shaft allowing the alignment module on this side to rotate.

3.8 Materials, Dimensions, and Clearances

In this section, the choice of materials, dimensions, clearances, and tolerances of the parts and assemblies strictly essential for the correct functioning and assembly of the experimental testing device will be analyzed. The tolerances on the assembly of commercialized and normalized parts will be stipulated according to the manufacturer's technical specifications. ISO tolerance grades can be found in table 3.1.

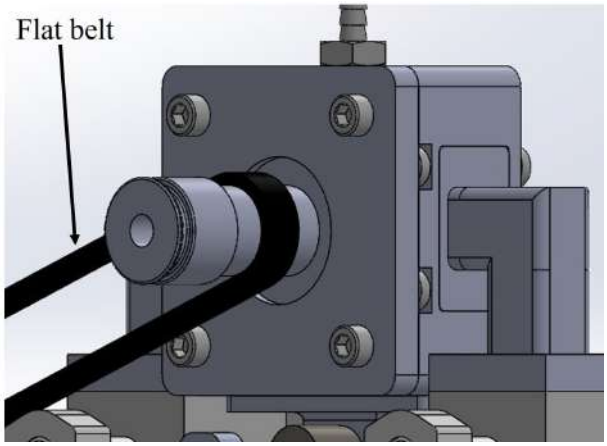

Figure 3.19: Flat belt connected to the fixation part on the inlet side of the device.

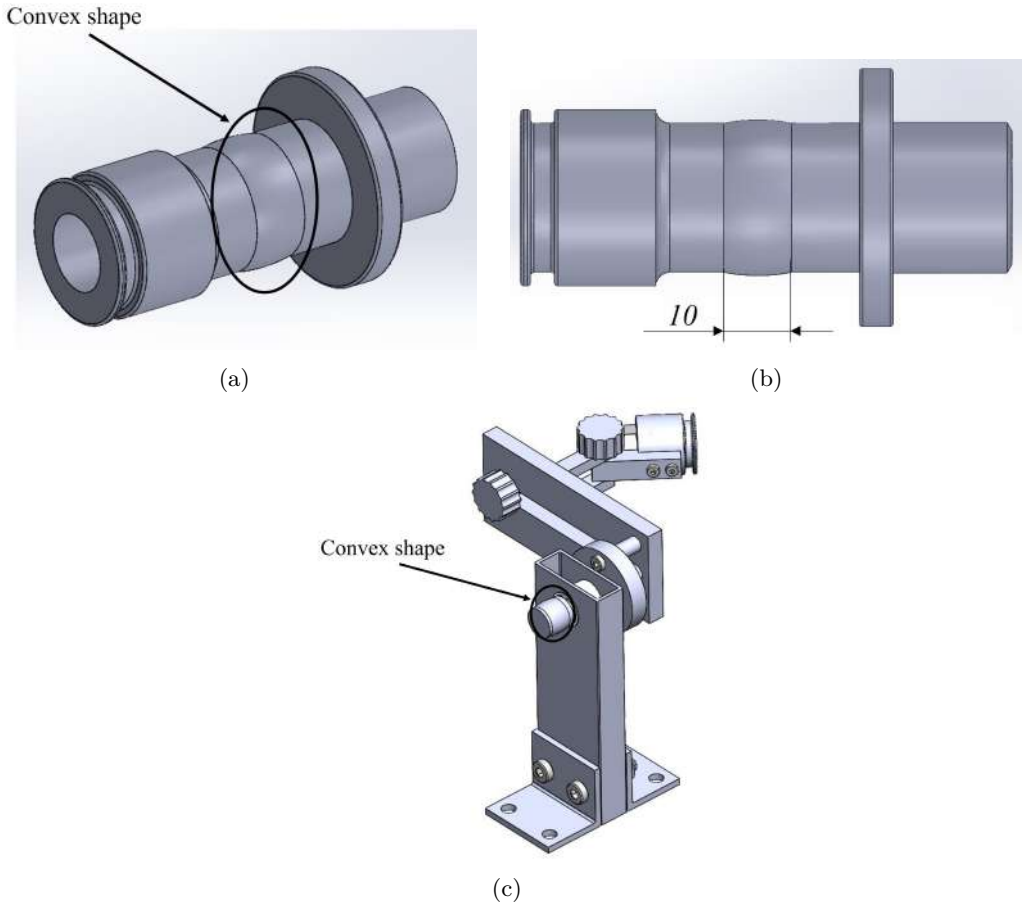

Figure 3.20: Convex shapes machined to endow stability during the belts movement. (a) Convex shape on the inlet fixation part. (b) Convex shape's length. (c) Convex shape on the outlet shaft.

3.8.1 Fixation Part (Inlet Side)

The fixation part, in direct contact with biological tissue and with water (or physiological saline), will be made from stainless steel AISI 316 (American Iron and Steel Institute) due to its improved corrosion resistance and good machinability. The groove which hosts the silicone/rubber band

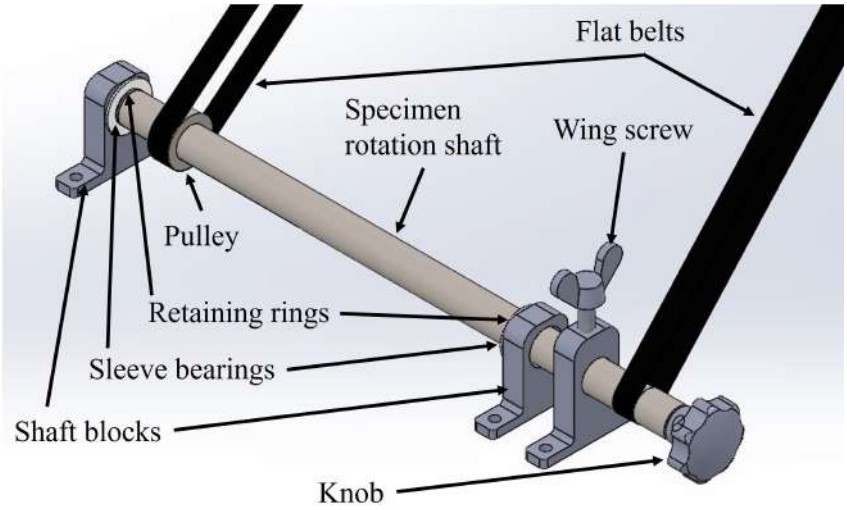

Figure 3.21: Specimen rotation shaft assembly.

Table 3.1: Normalized tolerance grades for nominal dimensions up to 50 mm. From ISO (2018).

Nominal Dim. [mm]		Normalized tolerance grades																	
		IT01	IT0	IT1	IT2	IT3	IT4	IT5	IT6	IT7	IT8	IT9	IT10	IT11	IT12	IT13	IT14	IT15	IT16
Above	Until (inc.)	Tolerances																	
		um													mm				
-	3	0.3	0.5	0.8	1.2	2	3	4	6	10	14	25	40	60	0.1	0.14	0.25	0.4	0.6
3	6	0.4	0.6	1	1.5	2.5	4	5	8	12	18	30	48	75	0.12	0.18	0.3	0.48	0.75
6	10	0.4	0.6	1	1.5	2.5	4	6	9	15	22	36	58	90	0.15	0.22	0.36	0.58	0.9
10	18	0.5	0.8	1.2	2	3	5	8	11	18	27	43	70	110	0.18	0.27	0.43	0.7	1.1
18	30	0.6	1	1.5	2.5	4	6	9	13	21	33	52	84	130	0.21	0.33	0.52	0.84	1.3
30	50	0.6	1	1.5	2.5	4	7	11	16	25	39	62	100	160	0.25	0.39	0.62	1	1.6

and the zip tie is made at 1.5 mm from the edge to minimize the unusable specimen length. The convex shape made to host the flat belt is machined with a 1 mm height to prevent it from having axial movement along the fixation part and maintain the alignment of the flat belt during rotation.

The radial shaft seal chosen is SKF[1] 8634 CRWA5 seal. The tolerances on both the housing bore and the shaft are set according to the manufacturer's indication, meaning that the housing bore (31.75 mm of nominal diameter) will have an IT8 ISO tolerance. Furthermore, the depth of the bore will be 0.3 mm deeper than the shaft's thickness. The bore's necessary chamfer and radius are to be designed according to Figure 3.22, where $r = 0.3$ mm.

As mentioned previously, the fixation part will be secured in its place with the aid of the fixation part locker. The fixation part is designed with a flap with a larger diameter than the seal's bore to prevent it from advancing furthermore inside the connector block. The locker has a bore machined on one of the surfaces so that when the face presses against the connector block, the fixation part's flap remains housed inside the locker (Figure 3.23a). Furthermore, the mechanism is designed to work with a clearance, c, between 0.2 and 0.3 mm (Figure 3.23b).

The nominal dimensions are:

[1] https://www.skf.com/group

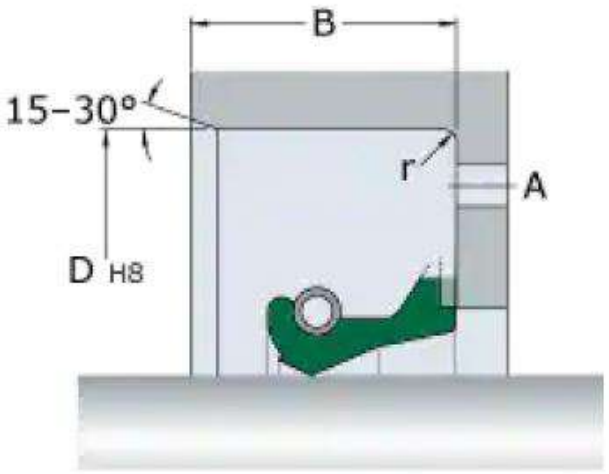

Figure 3.22: Bore requirements for SKF's radial shaft seal assembly. From SFK (2019).

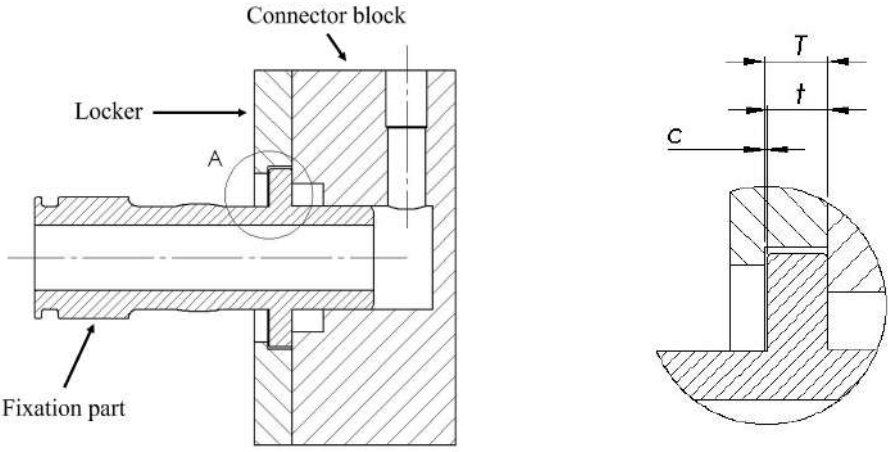

(a) (b)

Figure 3.23: Assembly of fixation part and locker on connector block. (a) Section view of the assembly. (b) Detail A with design clearance.

- $T = 5.20$ mm
- $t = 5.00$ mm

Where T belongs to the locker, and t belongs to the fixation part.The tolerances for the hole and the flap are H8 and h8, respectively. This means for the hole,

- Upper deviation = 18 µm
- Lower deviation = 0 µm

And for the flap,

- Upper deviation = 0 µm
- Lower deviation = -18 µm

Since the maximum and minimum values for a dimension with a hole or female function (meaning that during the assembly it will be on the outside of another part, position of tolerance zone indicated with upper case letter) can be obtained, respectively,

$$D_{max} = D_n + D_u \tag{3.6}$$

$$D_{min} = D_n + D_l \tag{3.7}$$

where,

- D_{max} = Maximum dimension
- D_{min} = Minimum dimension
- D_n = Nominal dimension
- D_u = Upper deviation
- D_l = Lower deviation

And the maximum and minimum values for a dimension with a shaft or male function (meaning that during the assembly it will be on the inside of another part, position of tolerance zone indicated by lower case letter) can be obtained, respectively,

$$d_{max} = d_n + d_u \tag{3.8}$$

$$d_{min} = d_n + d_l \tag{3.9}$$

where,

- d_{max} = Maximum dimension
- $d_{mín}$ = Minimum dimension
- dn = Nominal dimension
- du = Upper deviation
- dl = Lower deviation

From Equations (3.6) and (3.7), the dimensions for T are

$$T_{max} = T_n + T_u \Leftrightarrow T_{max} = 5.20 + 0.018 = 5.218 \text{ mm}$$

$$T_{min} = T_n + T_l \Leftrightarrow T_{min} = 5.20 + 0 = 5.20 \text{ mm}$$

and from Equations (3.8) and (3.9), the dimensions for t are

$$t_{max} = t_n + t_u \Leftrightarrow t_{max} = 5.0 + 0 = 5.0 \text{ mm}$$

$$t_{min} = t_n + t_l \Leftrightarrow t_{min} = 5.0 - 0.018 = 4.982 \text{ mm}$$

Having the maximum and minimum dimensions, it is now possible to obtain the maximum and minimum clearance value, C_{max} and C_{min}, respectively,

$$C_{max} = D_{max} + d_{min} \tag{3.10}$$

$$C_{min} = D_{min} + d_{max} \tag{3.11}$$

From Equations (3.10) and (3.11), the maximum and minimum clearance values for c are

$$c_{max} = 5.218 - 4.982 = 0.236 \text{ mm}$$

$$c_{min} = 5.2 - 5.0 = 0.2 \text{ mm}$$

The clearance is within the design interval and the assembly of the two components is classified as a clearance fit.

While rotating, the fixation part will be in contact with the connector block in a shaft/hole relationship as shown in Figure 3.24.

The nominal dimensions are

- $d = 22.23$ mm
- $D = 22.23$ mm

Where d belongs to the fixation part and D to the connector block. In this assembly, a clearance fit will also be chosen, allowing for an effortless and manual assembly while enabling free rotation at the same time. More precisely, a close running fit will be chosen, a common fit in mechanical assemblies, represented by its ISO symbol as $H8/f7$. This fit translates in tolerances for d and D of $f7$ and $H8$, respectively.

3.8.2 Specimen rotation shaft

The shaft responsible for rotating the specimen will be in contact with two flat belts, allowing it to transmit rotation to two different mechanisms simultaneously. The belt on the outlet shaft will be in direct contact with the specimen rotation shaft, while the belt on the fixation part will be in contact with a pulley which will then be assembled to the shaft (Figure 3.25a). The specimen rotation shaft will have a slot on which a ledge on the pulley will slide (Figure 3.25b), allowing it to follow the linear movement of the set on the inlet side. The clearance between the ledge's width on the pulley and the slot's width on the shaft (Figure 3.25c), $c2$, should be larger than 0.005 mm and smaller than 0.05 mm.

The nominal dimension of both b and B is 3 mm. By attributing an h7 tolerance to b, and an F8 tolerance to B, the tolerance zones come as

- Upper deviation for $b = 0$ µm
- Lower deviation for $b = -10$ µm
- Upper deviation for $B = 20$ µm
- Lower deviation for $B = 6$ µm

By using the same method as previously shown, the limit dimensions for b can be obtained

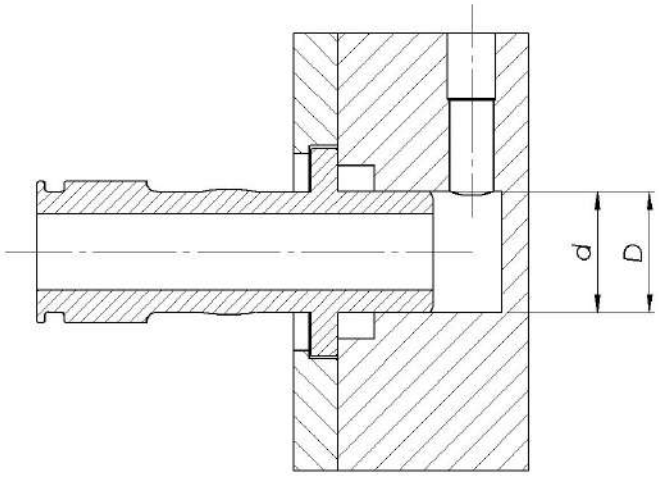

Figure 3.24: Assembly of fixation part on connector block. Dimension d has the same nominal value as D.

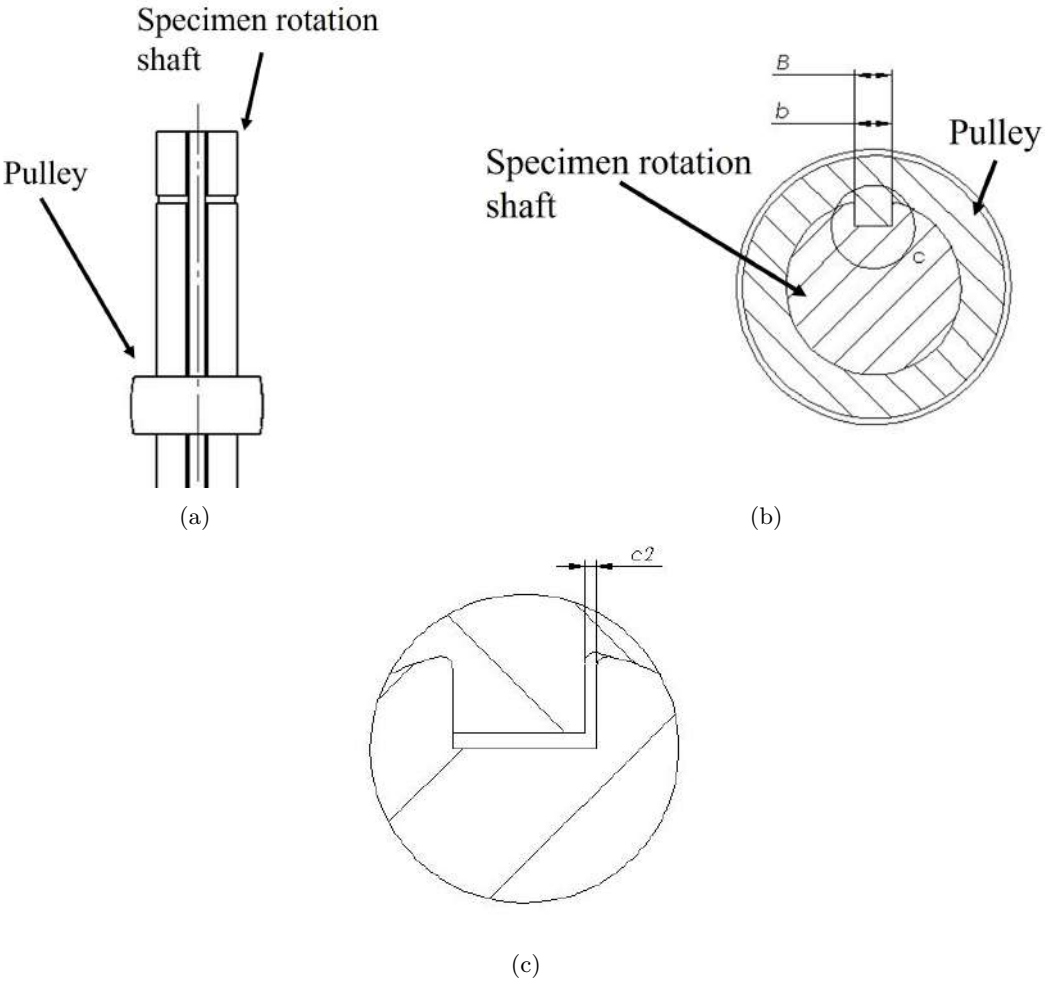

Figure 3.25: Assembly and clearance between specimen rotation shaft and pulley. (a) Section view of the shaft-pulley set. b belongs to the pulley, B belongs to the shaft. (b) Clearance between parts exaggerated for demonstration purposes.

$$b_{max} = 3.0 + 0 = 3.0 \text{ mm}$$

$$b_{min} = 3.0 - 0.01 = 2.990 \text{ mm}$$

and for B, the dimensions are

$$B_{max} = 3.0 + 0.020 = 3.020 \text{ mm}$$

$$B_{min} = 3.0 + 0.06 = 3.006 \text{ mm}$$

Since the clearance is nominally 0, it will be obtained by the chosen tolerance grades and position of tolerance zone. Once the maximum and minimum dimensions of both parts are known, the clearance can be calculated

$$c2_{max} = 3.020 - 2.990 = 0.030 \text{ mm}$$

$$c2_{min} = 3.006 - 3.0 = 0.006 \text{ mm}$$

It can be concluded that the design clearance between parts is respected.

Another clearance needs to be taken into consideration, on the assembly of the two components, as shown in Figure 3.26.

Again, the nominal dimensions for the ledge's height (h) and the slot's height (H) are the same (2.16 mm in this case), so the clearance, $c3$ will be determined by the tolerances. The tolerance attributed to dimension h is h7, while to dimension H is F8. The mechanism is designed to work properly with a minimum clearance of 0.005 mm and a maximum clearance of 0.05 mm. Since the nominal value of this dimension belongs to the same interval, on the standard ISO tolerance grade, as the one demonstrated in the analysis above, and the position of tolerance grades are the same, the upper and lower deviations are also equal to the ones previously demonstrated. The dimensions can now be determined

$$h_{max} = 2.16 + 0 = 2.16 \text{ mm}$$

$$h_{min} = 2.16 - 0.01 = 2.15 \text{ mm}$$

$$H_{max} = 2.16 + 0.020 = 2.18 \text{ mm}$$

$$H_{min} = 2.16 + 0.006 = 2.166 \text{ mm}$$

From these values, the clearance can be determined

$$c3_{max} = 2.18 - 2.15 = 0.030 \text{ mm}$$

$$c3_{min} = 2.166 - 2.16 = 0.006 \text{ mm}$$

Is it possible to conclude that the chosen tolerances result in a clearance interval within the desired.

The final tolerances to be determined on this assembly are for the pulley's internal diameter

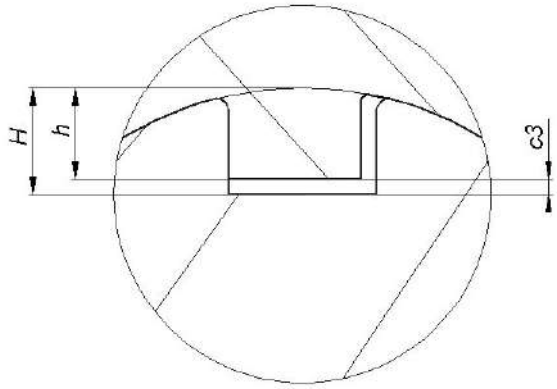

Figure 3.26: Existing clearance between the ledge's height and the slot's height. H belongs to the shaft while h belongs to the pulley. Clearance has been enhanced for demonstration purposes.

(DP) and the shaft's diameter (ds). The parts will have relative sliding movement with a clearance (Figure 3.27) that will be determined by the tolerances since both dimensions are nominally the same and equal to 14 mm. This value should be greater than 0.01 mm and lower than 0.1 mm.

By attributing an F8 tolerance to DP and an h8 tolerance to ds, the resulting deviations are

- Upper deviation for $DP = 43$ µm
- Lower deviation for $DP = 16$ µm
- Upper deviation for $ds = 0$ µm
- Lower deviation for $ds = -27$ µm

By applying Equations (3.6) to (3.9), the maximum and minimum values for both dimensions can be determined

$$DP_{max} = 14.0 + 0.043 = 14.043 \text{ mm}$$

$$DP_{min} = 14.0 + 0.016 = 14.016 \text{ mm}$$

$$ds_{max} = 14.0 + 0 = 14.0 \text{ mm}$$

$$ds_{min} = 14.0 - 0.027 = 13.973 \text{ mm}$$

The clearance of the assembly can be achieved from Equations (3.10) and (3.11)

$$c4_{max} = 14.043 - 13.973 = 0.070 \text{ mm}$$

$$c4_{min} = 14.016 - 14.0 = 0.016 \text{ mm}$$

The final clearance values are too found within the required interval.

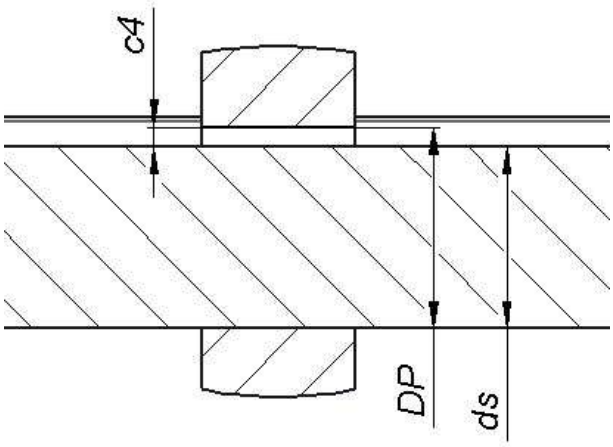

Figure 3.27: Existing clearance between the pulley's internal diameter and the shaft's diameter. $c4$ has been enhanced for demonstration purposes.

3.8.3 "L" shaped arm

The "L" shaped arm that connects the connector block to the linear guide shafts is composed of 3 assembled parts that assemble on each other and are fixed with socket countersunk head screws (Figure 3.28). The head of the screws will be sunk on conical grooves machined on the opposite faces of the assembly faces on both parts 1 and 3. To guaranty that the assembly is made without interference, when the assembly face on part 2 penetrates the grooves on both part 1 and 3, a clearance should be present. The existing clearance, c5 (Figure 3.29), is designed to be larger than 0 mm and lower than 0.1 mm.

The nominal values for both W and w dimensions are 36 mm, where W belongs to part 1 and is considered a hole dimension, and w belongs to part 2 and is considered a shaft dimension. H and h also have the same nominal value, 40 mm. Since both dimensions are on the same category on the ISO tolerance table, their grade will be the same. W and H will have a tolerance of H8, while w and h will have a tolerance of h8.

These translate in the following deviations:

- Upper deviation for $H = 39$ µm
- Lower deviation for $H = 0$ µm
- Upper deviation for $h = 0$ µm
- Lower deviation for $h = -39$ µm
- Upper deviation for $W = 39$ µm
- Lower deviation for $W = 0$ µm
- Upper deviation for $w = 0$ µm
- Lower deviation for $w = -39$ µm

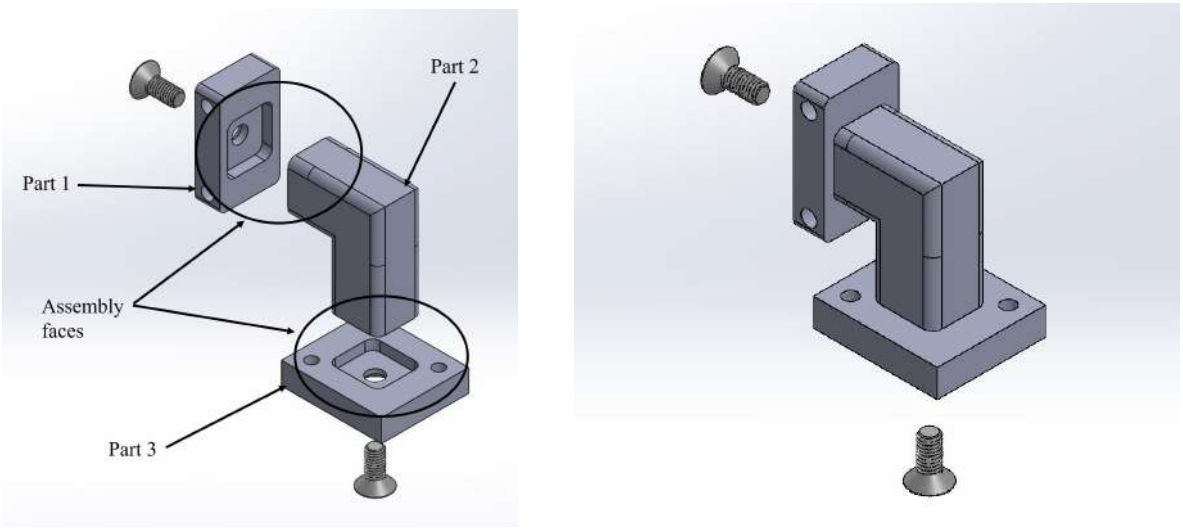

(a) (b)

Figure 3.28: Assembly sequence of the L arm. (a) The assembly face on part 2 will penetrate the grooves present on both parts 1 and 3. (b) The separated parts are fixed together with socket countersunk head screws.

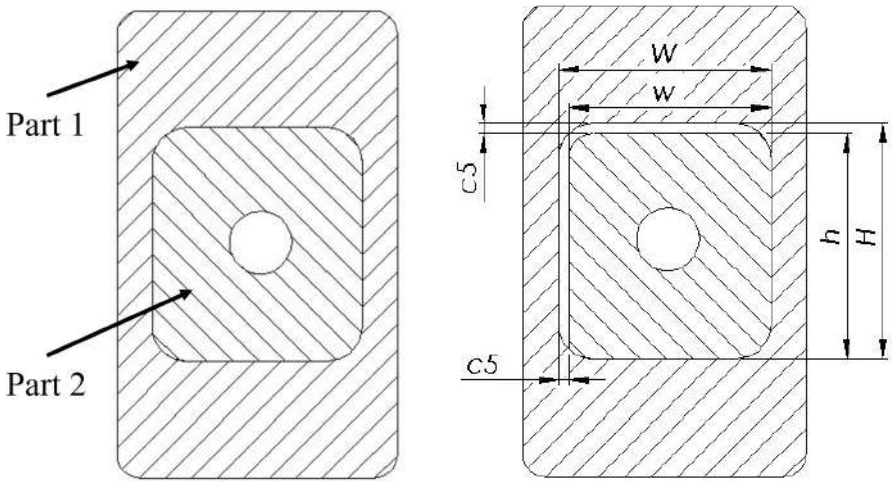

(a) (b)

Figure 3.29: Section view of the assembly of part 2 on part 1. (a)

With the chosen tolerances, the maximum and minimum dimensions can be obtained for H and h

$$H_{max} = 40.0 + 0.039 = 40.039 \text{ mm}$$

$$H_{min} = 40.0 + 0 = 40.0 \text{ mm}$$

$$h_{max} = 40.0 + 0 = 40.0 \text{ mm}$$

$$h_{min} = 40.0 - 0.039 = 39.961 \text{ mm}$$

and for W and w

$$W_{max} = 36.0 + 0.039 = 36.039 \text{ mm}$$

$$W_{min} = 36.0 + 0 = 36 \text{ mm}$$

$$w_{max} = 36.0 + 0 = 36.0 \text{ mm}$$

$$w_{min} = 36.0 - 0.039 = 35.961 \text{ mm}$$

Having calculated the values for the dimensions, the maximum clearance values can be obtained wither by analyzing the width of the section

$$c5_{max} = 40.039 - 39.961 = 0.078 \text{ mm}$$

$$c5_{min} = 40.0 - 40.0 = 0.0 \text{ mm}$$

or by analyzing the height of the section

$$c5_{max} = 36.039 - 35.961 = 0.078 \text{ mm}$$

$$c5_{min} = 36.0 - 36.0 = 0.0 \text{ mm}$$

3.8.4 Ensuring no interferences on assembly

In the previous analysis, an assembly between two parts was looked in to and the position of tolerance zone H/h was chosen.

H/h tolerance position is characterized by assuming a lower deviation for holes, and an upper deviation for shafts of 0 (Figure 3.30). This translates into the fact that when an assembly of two parts is characterized by having H/h tolerances on the dimensions that fit together, in no possible situation can interferences occur.

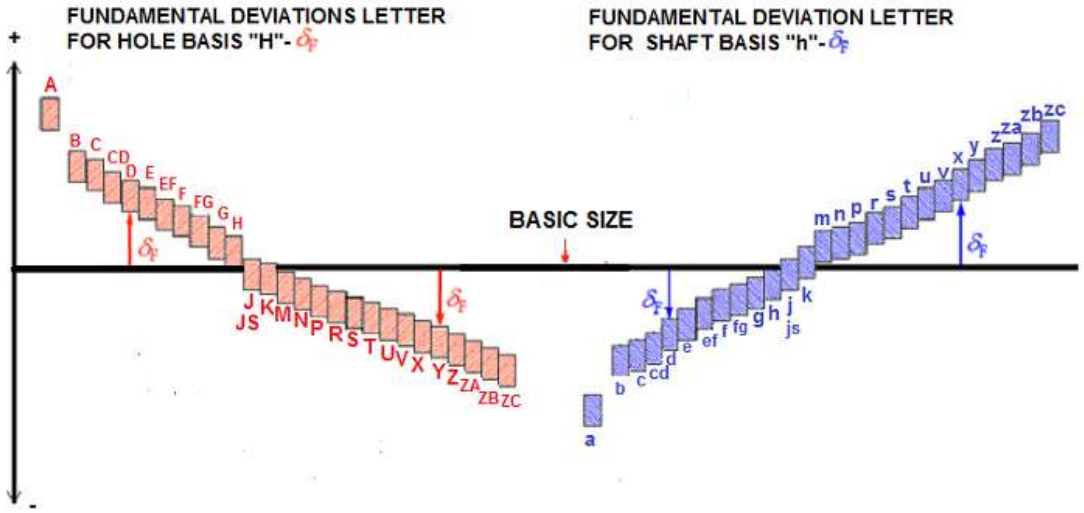

Figure 3.30: ISO position of tolerance zone relatively to the nominal (Basic) size. From infomech (2014)

Besides the tolerances and clearances presented in this chapter, several dimensions for parts that fit together where no minimum or maximum clearances are of importance to the functioning

of the device were designed with an H/h position. This decision guarantees that all these assemblies can be made manually. Other tolerances positions will be taken into consideration as well.

Furthermore, all technical drawings are presented with a general tolerance ISO 2768-1: 1989 medium (Table 3.2).

Table 3.2: Limits for linear measures [mm] according to the standard ISO 2768-1: 1989.

Tolerance class	0.5 to 3	above 3 to 6	above 6 to 30	above 30 to 120	above 120 to 400	above 400 to 1000	above 1000 to 2000
f (fine)	± 0.05	± 0.05	± 0.1	± 0.15	± 0.2	± 0.3	± 0.5
m (medium)	± 0.1	± 0.1	± 0.2	± 0.3	± 0.5	± 0.8	± 1.2
c (coarse)	± 0.15	± 0.2	± 0.5	± 0.8	± 1.2	± 2	± 3
v (very coarse)	-	± 0.5	± 1	± 1.5	± 2.5	± 4	± 6

3.9 Conclusions

In this chapter the design of a testing device capable of performing experimentation on biological tissue is presented. At this stage of development, a virtualization of the design was implemented. The device is able to fix a tubular-shaped specimen by the edges. The sample is supposed to be submitted to a physiological inflate loading. The versatility of the device allows not only for parts with parallel end faces to be tested but also parts with different angles between the end faces. Within the scope of human anatomy, this feature permits experimentation, for example, on the ascending, descending, and abdominal aorta.

The analysis made in this chapter allowed to synthesize the design parameters necessary for the fulfillment of the requirements. A critical part of the device is the fixation part, where special care on selecting dimensions was necessary to guaranty the specimen is fixed while minimizing the unused area of observation. It is important to mention that the geometry and tightening method were chosen on empirical knowledge and to guaranty the success of the inflation of the specimen, it is fundamental to manufacture the parts and assemble the device in a laboratory environment while testing it with materials that can be approximated to biological tissue.

Materials for non-commercialized parts were chosen based on corrosion resistance, stainless steel being the appropriate solution. The choice of clearances is based on the principle that most parts can be manually assembled whilst not allowing for significant misalignment and vibrations. The tolerances are within the reach of common machining techniques such as turning, drilling, and milling.

4 Digital-twin platform for testing an aortic aneurysm piece: a case study

4.1 Introduction

The first step in the process of obtaining a 3D model of an aneurysm with a patient-specific geometry is the conversion of Digital Imaging and Communications in Medicine (DICOM) files obtained from clinical imaging into STL or equivalent formats. DICOM is the standard format for medical images that can be exchanged with the data and quality necessary for clinical use, and it is implemented on almost every radiology, cardiology imaging, and radiotherapy device.

Among several software nowadays available to process and convert DICOM files to 3D models, one can highlight the following list: Materialise Mimics, Simpleware ScanIP Medical (Synopsys®), 3D Slicer, democratiz 3D®, InVesalius, and DICOM Viewer PRO (Inobitec®). Tables 4.1 (proprietary software) and 4.2 (open source software) present a comparison of several features between the different software previously mentioned. The one that will be used in the present study to generate a patient-specific 3D reconstruction of an ATAA is 3D Slicer. It has the advantages of being open-access and operations can be automatised using the python programming languages.

4.2 Patient-specific 3D geometric reconstruction

In anatomy, the human body can be divided into 3 planes, the coronal, the transverse, and the saggital. These planes are used to accurately describe locations on the body and they are called anatomic planes (Figure 4.1). When a CT exam is executed, the output it provides is images of the three anatomic planes (Figure 4.3). In a CTA, since contrast has been injected into the bloodstream, the identification of biological structures is easier, as can be shown in Figure 4.2.

The DICOM data used for the case study is from a CTA scan. When loading them to the software, it is possible to observe the images taken on the three anatomical planes. By segmenting images on the different planes, it is then possible to obtain a 3D model of any organ, tissue, or bone. 3D Slicer has available several tools to aid in the process of segmentation, and the one used in this study was the “grow from seeds”. This tool consists of using two different markers, one to mark the pretended organ and the other to mark the background, and every few layers on the anatomical planes “seeds” are planted, booth on the pretended organ and outside of it (Figure 4.4). After executing the command, the software will automatically identify the region being studied (Figure 4.5).

The aorta and the background were marked, starting from the first images where the aorta was visible, on 10 approximately equally spaced images, on each plane. After the command

Table 4.1: DICOM to 3D software comparison table (proprietary software).

Features	Mimics	Simpleware ScanIP Medical	DICOM Viewer PRO
Supported input	CT, MRI, X-ray and more.	CT, MRI, Ultrasound and more.	PET and CT images.
Export	STL, PACS[1] compatible.	STL and FE mesh.	STL, OBJ, and PLY.
Versatility	Quick, semi-automatic segmentation. Extensive set of tools, Pulmonology module.	Automated image segmentation, tools for handling data with poor quality.	Vessel Analysis algorithm and vessel wall tissue classification, 3D tissue reconstruction.
Disadvantages	Commercial software. Additional modules commercialized separately.	Commercial software.	Commercial Software, does not support MRI.

Table 4.2: DICOM to 3D software comparison table (open source software)

Features	3D Slicer	democratiz 3D®	InVesalius
Supported input	CT, Ultrasound, radiation therapy images, and MRI.	CT images.	CT and MRI images.
Export	STL, Poly Data, and XML Poly Data.	STL.	STL, OBJ, and PLY.
Versatility	Over 150 extensions, real-time 3D reconstruction in surgical intervention, and Artificial Intelligence automatic segmentation.	3D model automatic generation, online platform and file sharing.	Used in hospitals and clinics, semi-automatic image segmentation, and volumetric and surface measurement tools.
Disadvantages	Quantity of modules and tools make the software complex to use.	DICOM files need to be converted to NRRD first.	Less consistent when segmenting soft-tissue structures.

was given for the software to extrapolate the whole aortic structure from the seeds, the result was carefully inspected to guaranty that the boundary between the pretended structure and the background was always on the correct location, and when the result was not according, manual rectification was performed. Since the 3D resulting structure has a rough surface, proper smoothing operations were performed obtaining the model in Figure 4.7. Different sections of the aorta can be observed on the model, such as the ascending aorta, aortic branches, aortic arch, and descending aorta.

[1]Picture Archiving and Communication System (PACS)

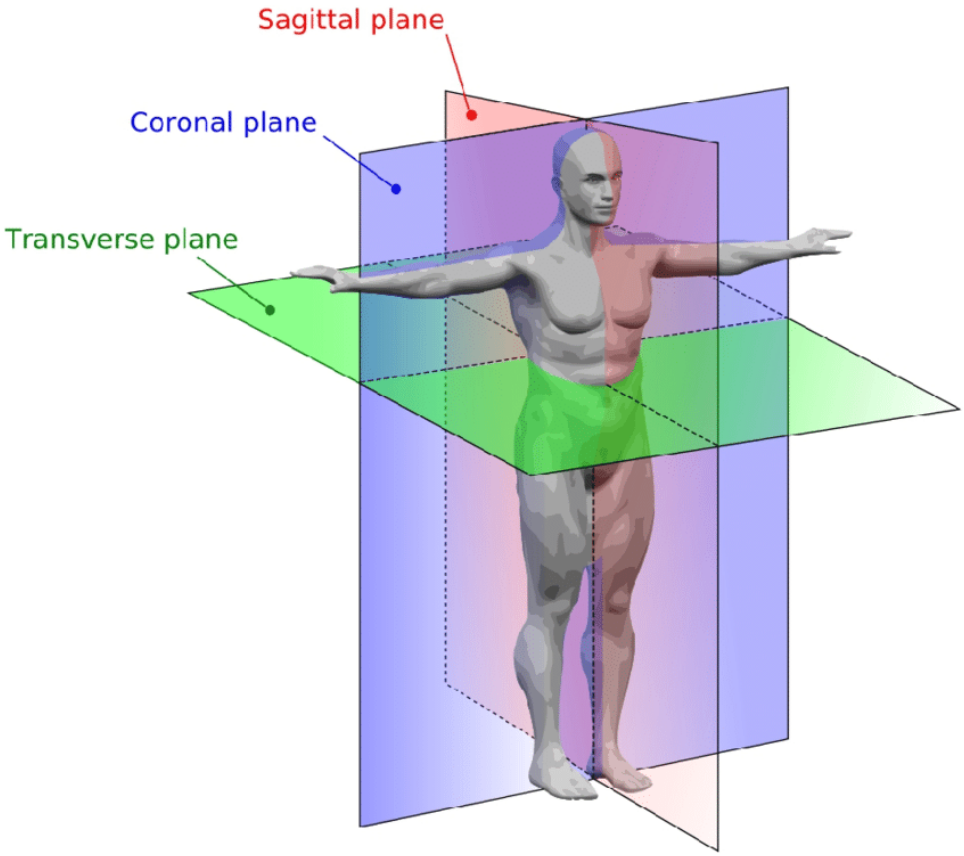

Figure 4.1: Graphical demonstration of the three anatomical planes. From (Adistambha et al., 2012)

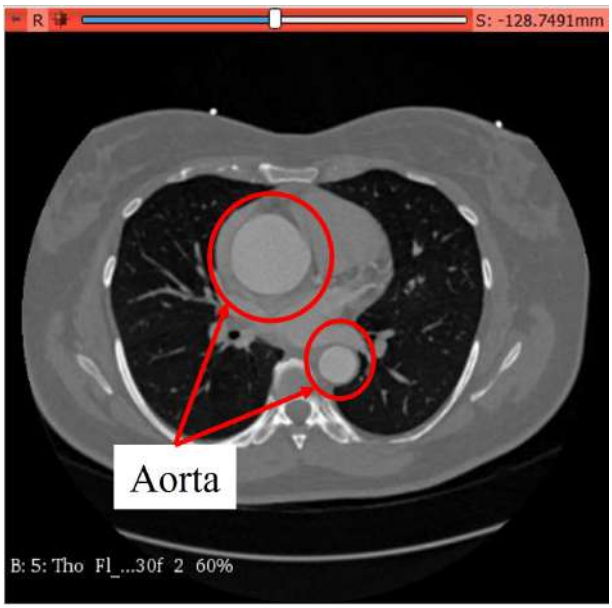

Figure 4.2: Identification of the location of the aorta on a CTA image. The contrast provokes an increase in intensity.

The segmentation process allowed to obtain a volume, but to perform a computational analysis, creating a FE model mesh, an approximate geometry of the aneurysm is required. The aneurysm section alone will be extracted from the obtained volume by making cuts on planes

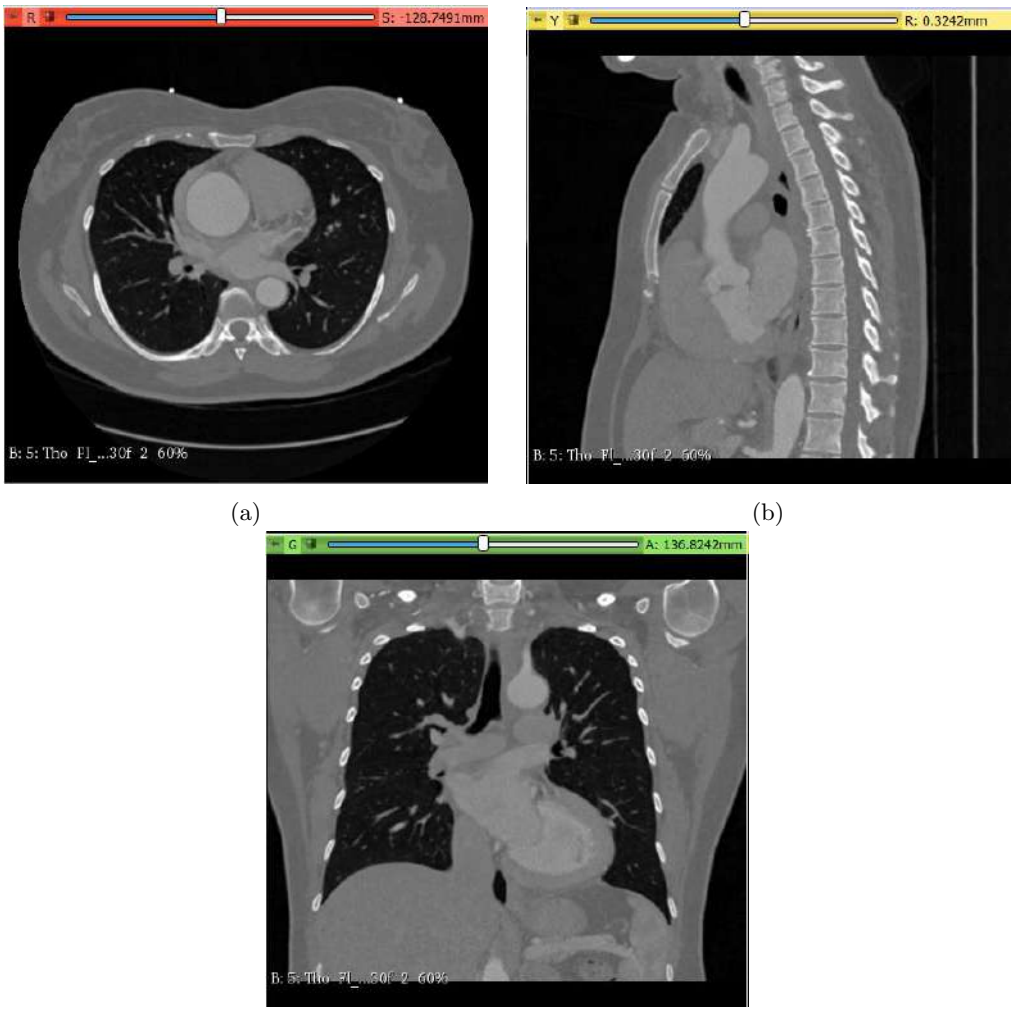

(a) (b)

(c)

Figure 4.3: CTA images of the each anatomical plane. (a) Transverse plane. (b) Saggital plane. (c) Coronal plane.

that are approximately perpendicular to the specimens axis. The diameter of the aorta on the cut cross sections (Figure 4.6) must be within the values of 26 and 34 mm as to maintain consistency with the diameter range of the stent-graft used in ATAA repair. Splines where marked on the cross sections to be defined as the end faces of the aneurysm, and the length was noted. Because they are not perfect circles, the length values were used to calculate the diameter of the theoretically circular end cross section as if the aorta was accommodating to a circular shape. The perimeter of a circle, P_{cir}, can be defined as

$$P_{cir} = \pi \times d \tag{4.1}$$

were d is the diameter.

By arranging equation (4.1), the diameter, d, can be obtained as

$$d = \frac{P_{cir}}{\pi} \tag{4.2}$$

Table 4.3 shows that the results of the diameters for the theoretical circular geometries are

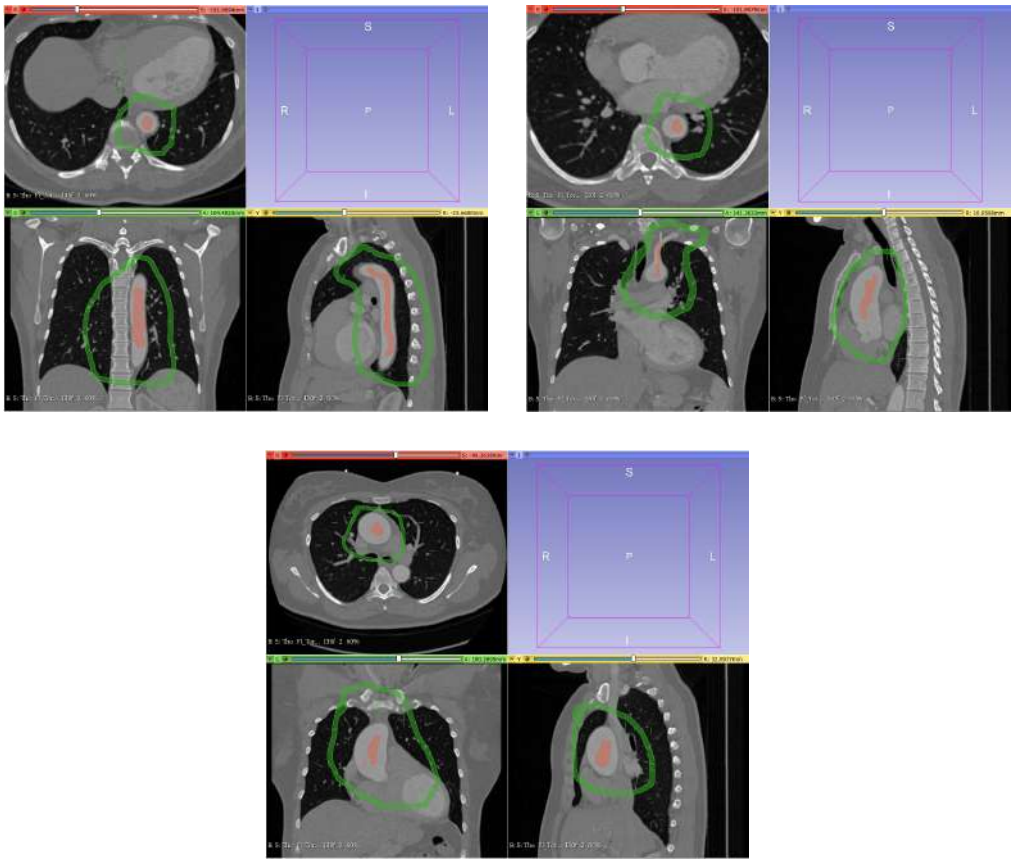

Figure 4.4: Seeds are planted on the pretended organ and background on different layers of the CT images.

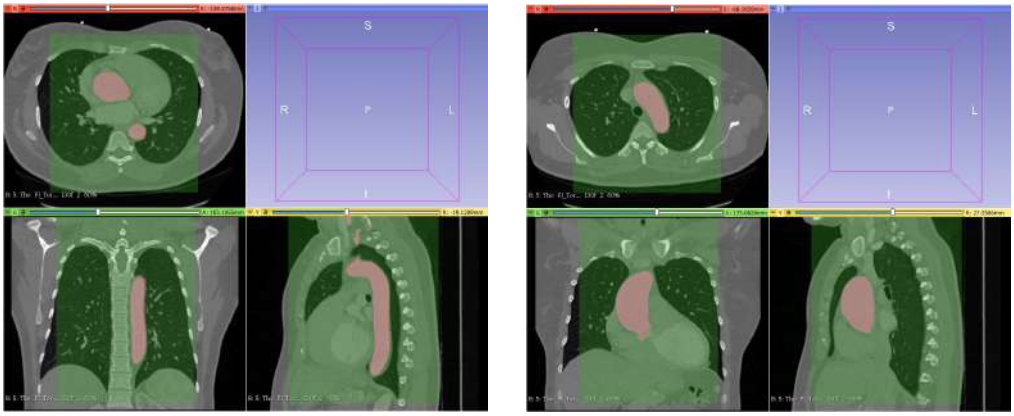

Figure 4.5: The software automatically identifies the aorta on every layer after the "grow from seeds" command is given.

within the desirable interval.

Table 4.3: Calculation of the circular cross section diameter for both ends of the aneurysm.

Cross section	Spline length [mm]	d [mm]
Section 1	104.67	33.32
Section 2	95.34	30.35

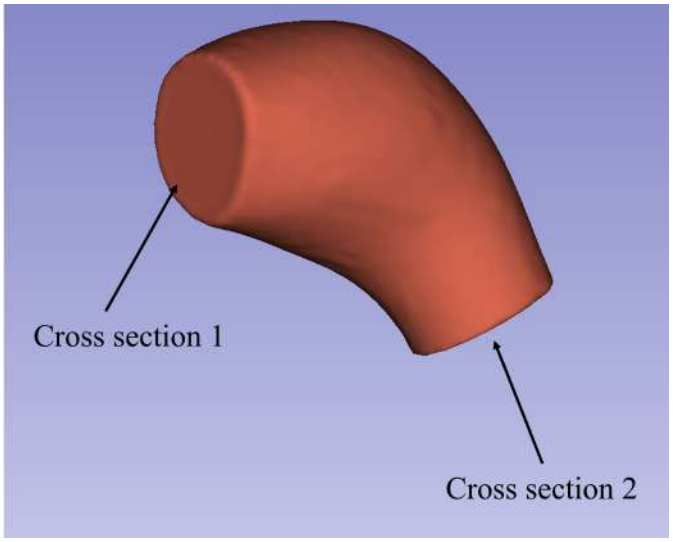

Figure 4.6: Portion of the aorta considered for the FE analysis. Cross section 1 is closest to the aortic root while cross section 2 is closest to the aortic branches.

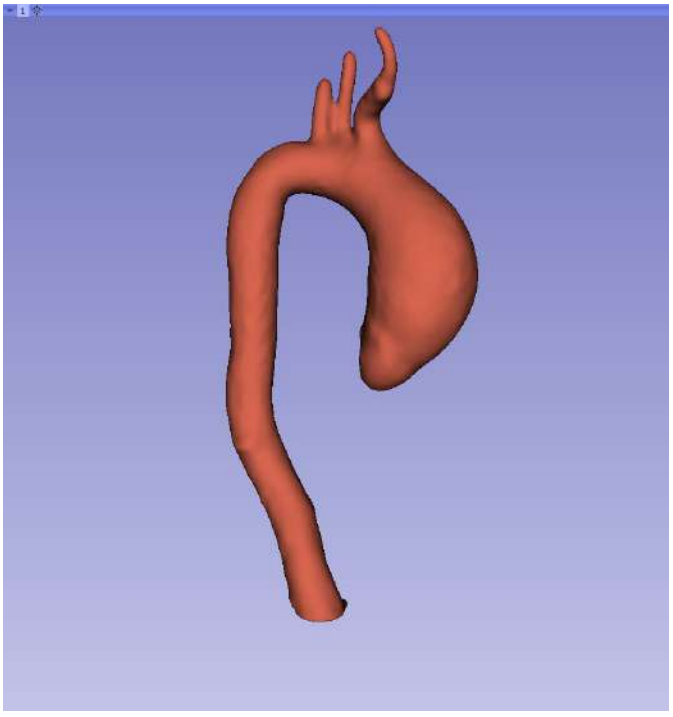

Figure 4.7: Volume obtained from the segmentation of CTA images.

4.3 Experimental test virtualization

4.3.1 3D geometry to model adaptation

The software used to simulate an internal pressure on the biological part is SOLIDWORKS® (Dassault Systèmes SolidWorks Corp.) Student edition. The analysis will be made using a shell with a surface geometry concordant with the inner geometry of the aorta, with a constant thickness of 1.9 mm based on presented papers where ATAA tissue was studied (Khanafer et al., 2011; Di Giuseppe et al., 2019; Duprey et al., 2016).

When the STL file is loaded in the software, the geometry presented is a mesh (Figure 4.8) with 79524 polygons that is not yet ready for analysis. The automatic tool, surface wizard, converts this mesh file into a surface geometry, allowing only the manual input of refining the detail of the surface, which will influence the number of faces present on the surface.

After the surface is generated with 1348 faces, some faces are not created and others are deformed due to limitations on the manual setting of the detail during the surface wizard phase (Figure 4.9a). This issue is fixed by deleting the surfaces and patching the hole with a surface defined by the surrounding edges (Figure 4.9b).

Since the surface that is going to be analyzed does not include the end faces, since these will be fixed during the non-linear simulation analysis, they will be merged thus reducing the number of faces to fix, and allowing for a better performance of the hardware being used (Figure 4.10). Finally, the creation of a simulation-ready geometry is complete.

4.3.2 Material model

As previously mentioned, aortic tissue has been characterized as a hyperelastic and incompressible material. The constitutive model assumed for this simulation will be the hyperelastic and isotropic two-term Mooney-Rivlin model (Mooney, 1940) used by Ruiz de Galarreta et al. (2017) to present a methodology for verifying AAA wall stress. In this paper, AAA phantoms were created, by segmenting CT images, with two commercially available bicomponent polyurethane resins by a vacuum casting process.

The Mooney-Rivlin constitutive model (Bergström, 2015) is characterized by the following expression

$$W = C_{10}(I_1^* - 3) + C_{01}(I_2^* - 3) + \frac{k}{2}(J-1)^2 \tag{4.3}$$

For this incompressible version of the model, $k \to \infty$. To define the near compressibility of the material the bulk modulus, k, was calculated using the expression

$$k = \frac{E}{3(1-2\nu)} \tag{4.4}$$

Where E is Young's modulus, and ν is Poisson's ratio.

The incompressible version of the model is then characterized by the strain energy expression

$$W = C_{10}I_1^* - 3) + C_{01}(I_2^* - 3) \tag{4.5}$$

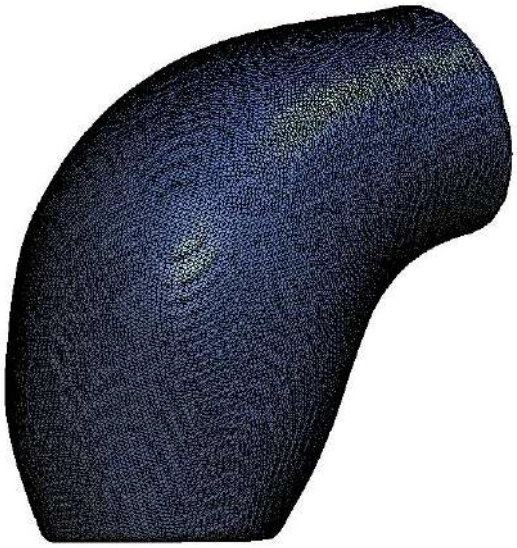

Figure 4.8: Triangular-shaped polygon mesh geometry obtained from 3D Slicer software, with 79524 polygons.

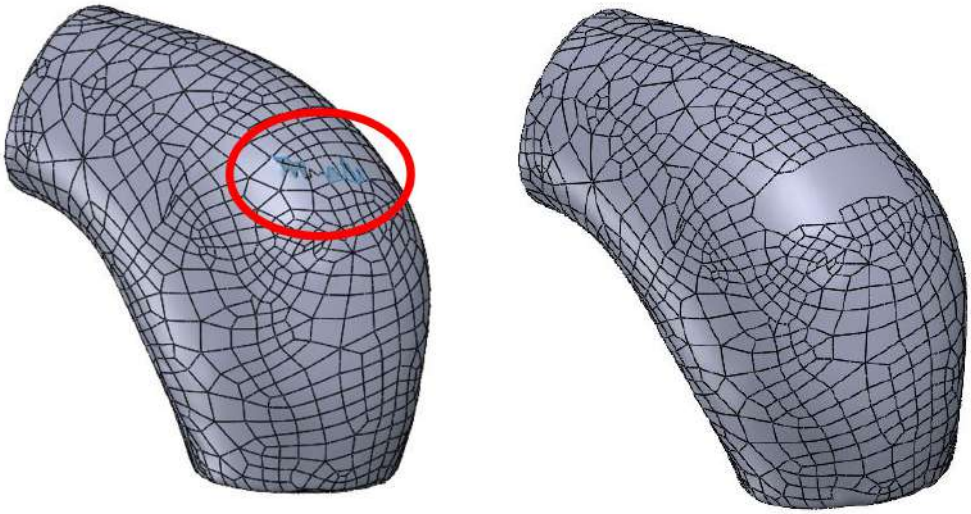

(a) (b)

Figure 4.9: Surface creation from the STL initial geometry, with 1348 faces. (a) Existence of gaps on the surface. (b) Deformed surfaces were deleted and the gaps were replaced based on surrounding edges.

Where W is the strain energy, I_1^* and I_2^* are the first and second invariants of the Cauchy-green deformation tensor, and C_{10} and C_{01} are material parameters. The Cauchy stresses in uniaxial, planar, and equibiaxial deformations are expressed by (Bergström, 2015)

$$\sigma_{uniax} = 2\left(\lambda^2 - \frac{1}{\lambda}\right)\left[C_{10} + \frac{C_{01}}{\lambda}\right] \tag{4.6}$$

$$\sigma_{planar} = 2\left(\lambda^2 - \frac{1}{\lambda^2}\right)[C_{10} + C_{01}] \tag{4.7}$$

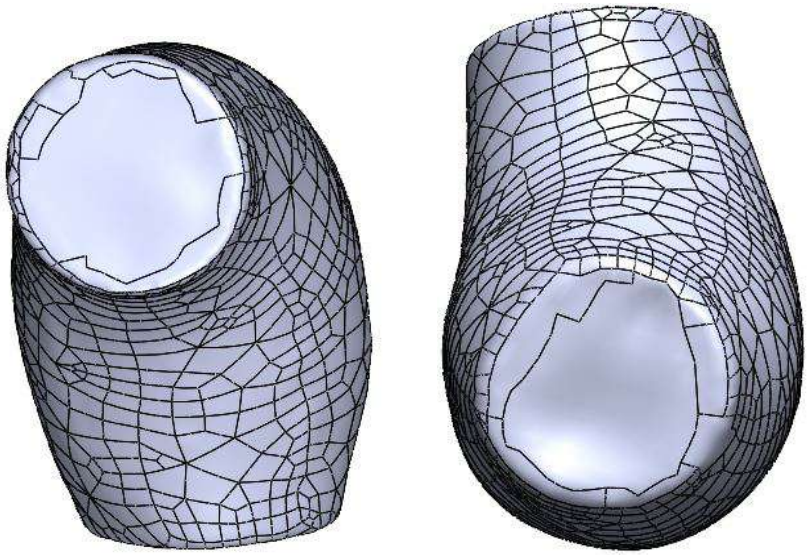

Figure 4.10: Merging of the end faces to increase hardware performance.

$$\sigma_{biaxial} = 2C_{10}\left(\lambda^2 - \frac{1}{\lambda^4}\right) + 2C_{01}\left[\lambda^4 + \frac{1}{\lambda^2}\right] \tag{4.8}$$

The material constants used for this concept proof will be 44.52 kPa for C_{10}, 624.18 kPa for C_{01}, and 0.49 for ν (Ruiz de Galarreta et al., 2017).

4.3.3 Simulation and results

In the virtualization of the inflation of the specimen, The end faces, and the ones on their periphery, were fixed, constraining them of translational motion and rotation. This condition is only an approximation of the real boundary conditions during the actual experimental test. Internal pressure is applied, being always perpendicular to the surface. 3 inflation trials were executed, with 5 kPa, 10 kPa, and 20 kPa values for internal pressure. A curvature-based mesh with triangular elements was generated with the following parameters:

- Element size: 4.0 mm
- Tolerance: 0.2 mm
- Number of nodes: 7022
- Number of elements: 3510
- Number of degrees of freedom: 34644

Figures 4.11 and 4.12 show the visualization of the test specimen on the testing device.

After all variables are set, the simulations are executed. The results for von Mises stress, displacement, and strain are shown in Figures 4.13, 4.14, and 4.15.

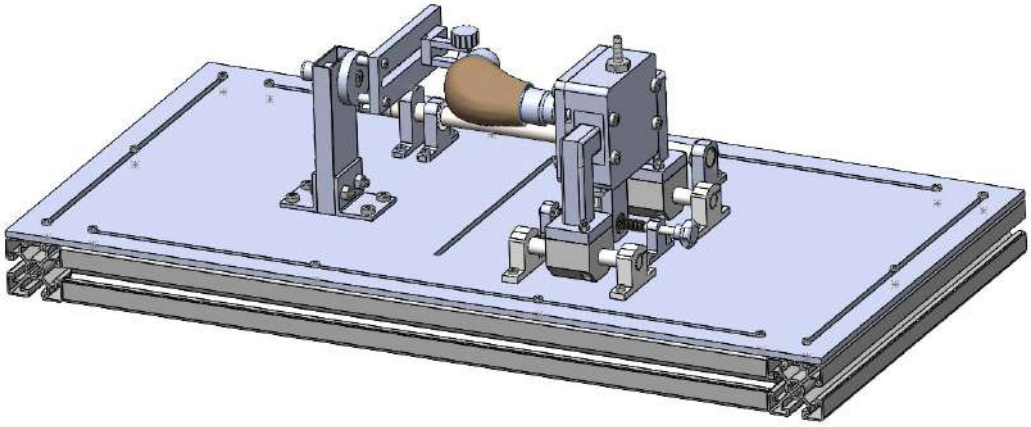

Figure 4.11: Isometric perspective of the virtualization of the assembly.

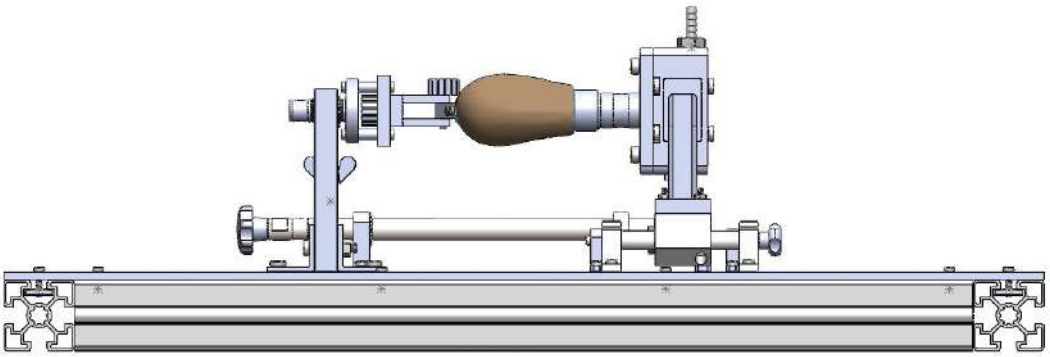

Figure 4.12: Front perspective of the virtualization of the assembly.

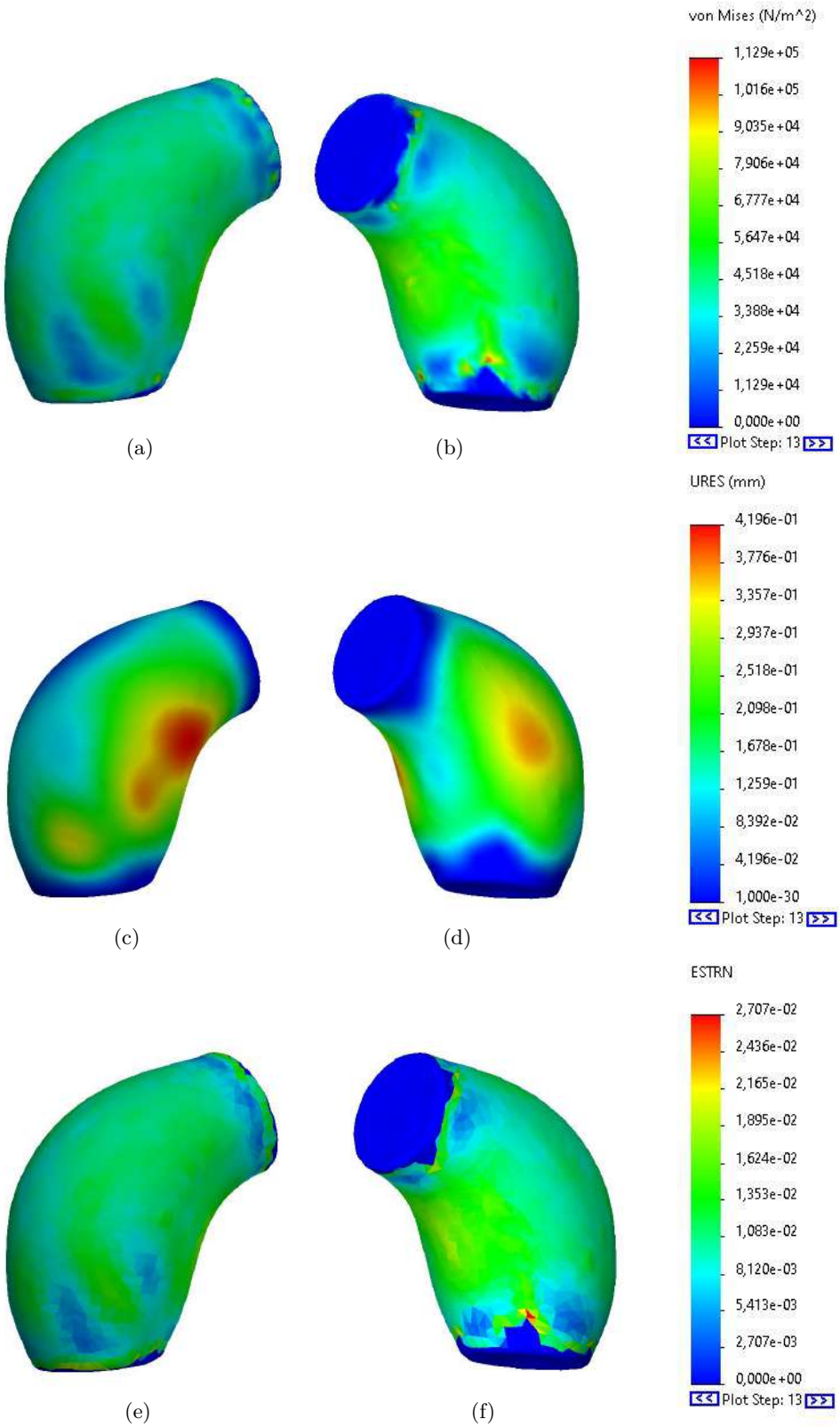

Figure 4.13: Simulation results with 5 kPa of internal pressure. (a) and (b) von-Mises stress [Pa]. (c) and (d) Displacement [mm]. (e) and (f) Strain.

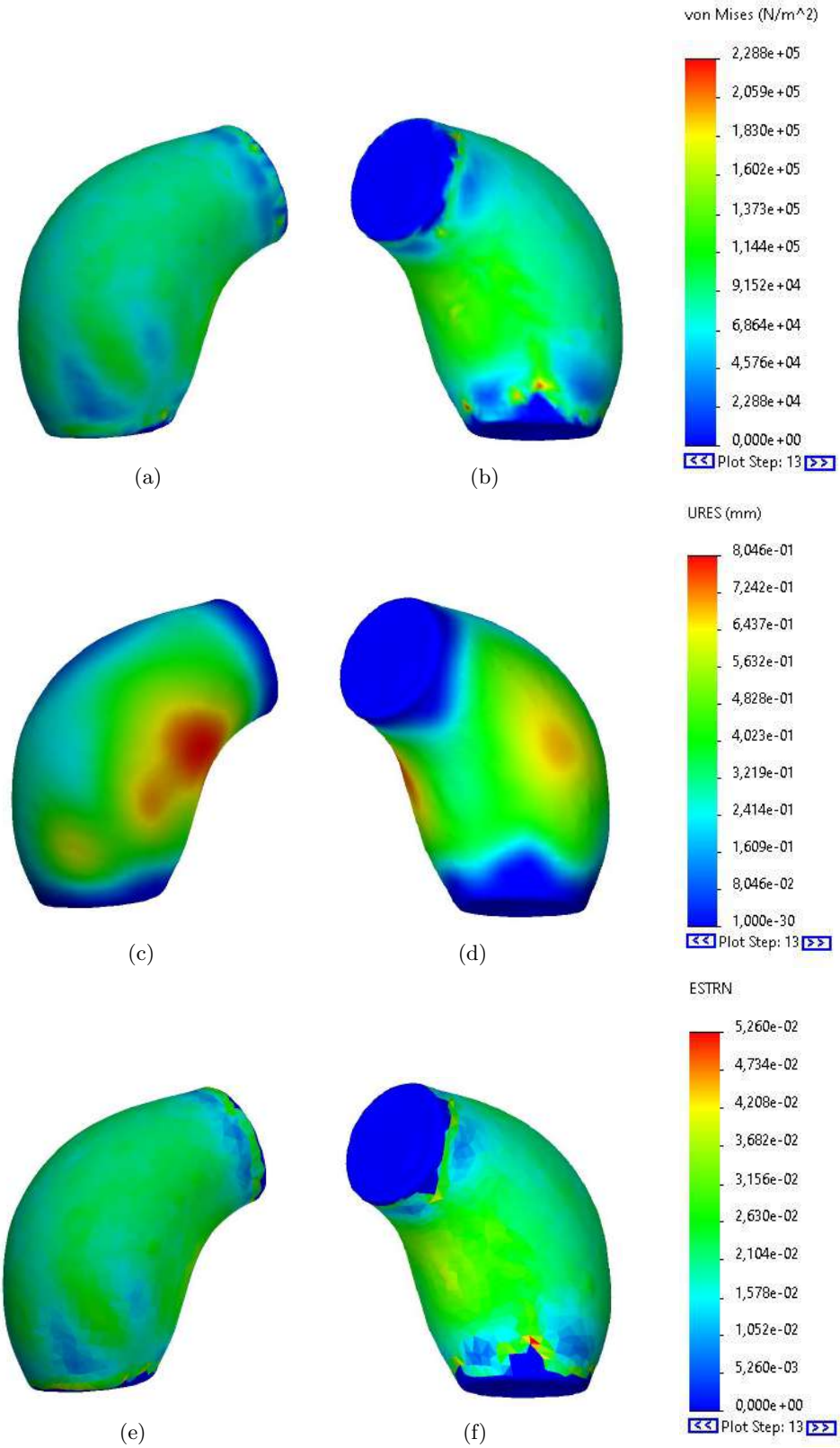

Figure 4.14: Simulation results with 10 kPa of internal pressure. (a) and (b) von-Mises stress [Pa]. (c) and (d) Displacement [mm]. (e) and (f) Strain.

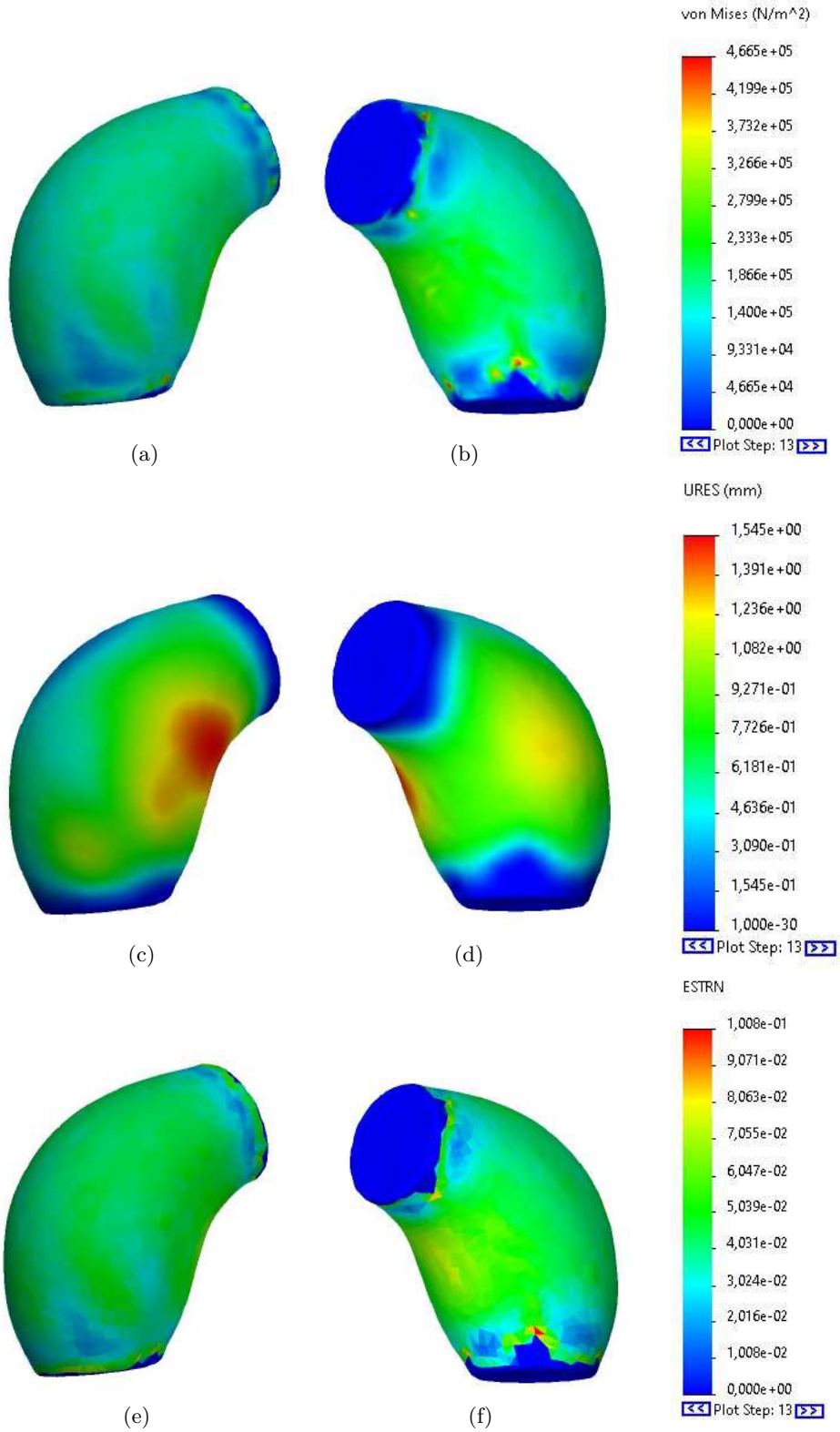

Figure 4.15: Simulation results with 20 kPa of internal pressure. (a) and (b) von-Mises stress [Pa]. (c) and (d) Displacement [mm]. (e) and (f) Strain.

5 Conclusions and future work

The presented work was divided into different chapters, each one with an important role as an introductory step to a large-scale investigation with the goal of adopting a biomechanical approach to clinical practice. ATAA is a life-threatening pathology that takes thousands of lives worldwide every year. To further dive into the study of its biomechanical behavior, one must understand the anatomy of the aorta and the physiology behind aortic tissue and aneurysms. The continuity of this study should be ensured with deeper research on the physiology of the different layers of the aorta, both before and after the occurrence of an aneurysm, where the significant existing heterogeneity should be deeply understood.

Computational tools have been increasingly used in clinical practice, where computed-aided diagnosis is possible through computer-aided detection and computer-aided quantification working together to return usable quantities aimed at helping identify the pathology. Several techniques have been presented to estimate *in-vivo* material properties and rupture risk index, but these approaches require experimental tests to validate themselves. Several previously performed experimental tests were presented to understand the universe of biological tissue experimentation. Specimen storing, handling and evaluation procedures, test protocols, and data analysis are crucial information to biological tissue experimental practice.

With the aid of Axiomatic Design, it was possible to introduce an innovative experimental device capable of performing an inflation test on an ATAA part. Functional requirements and design parameters were determined so that all necessary functionalities were taken into consideration. As future work, Axiomatic Design should be taken into further consideration and the process variables need to be determined to build the pretended device. The dimensions of a patient-specific geometry were used as a basis of work, however, the device was designed to adapt to different lengths and curvatures of an ATAA and to perform inflation on aneurysms from different segments of the aorta. The necessary parts that need to be fabricated were designed, and the basic functioning and assembly were briefly explained. The device is capable of inflating the subject with either a gas or a liquid. Some components of the full experimental set were excluded from the technical drawing and graphical demonstrations, such as a liquid or air pump, plastic tubes connecting the circuit, draining valve and reservoir, and the DIC setup (software, cameras, tripods, and speckle pattern). As a suggestion for future work, to assemble the entire experimental setup, all the previously mentioned components need to be chosen based on the information presented in this work. The test specimen fixation technique was chosen by an empirical method, and to perform the experimentation, this technique must be previously validated in its capability of holding the subject in place and being leakage proof. Once the setup is assembled, the first approach should be to use a material with a biomechanical behavior similar to biological tissue to validate the device both in its mechanical operation and

DIC performance.

A patient 3D-geometry was obtained via the segmentation of CTA images with open-source software, a critical step in the FE analysis of the virtualization of the experimental test. Since semi-automatic tools are used in obtaining this geometry, the accuracy of the models is fallible. Furthermore, since rectification is done manually, and a final smoothing process is performed, the final geometry is significantly influenced by the user's input. As future work, several segmentation methods should be taken into consideration, and the final geometry should be as similar to the real geometry as possible.

By attributing known parameters to the obtained geometry, it was possible to create a digital-twin platform and virtualise the experimental test. A hyperelastic and incompressible material model characterized the FE analysis simulation. As a suggestion for future work, deeper research into hyperelasticity should be made, and the constitutive model that better fits the experimental data should be used. Finite element model updating is based on the solution of a minimization problem where the goal is to minimize an objective function that evaluates the error between the numerical and the experimental data. This method should be used on testing the ATAA part to generate a model that better fits the biomechanical behavior of this material.

References

J.A. Elefteriades and E.A. Farkas. Thoracic aortic aneurysm: Clinically pertinent controversies and uncertainties. *Journal of the American College of Cardiology*, 55(9):841–857, 2010. ISSN 0735-1097. doi:10.1016/j.jacc.2009.08.084.

A. Maier, M.W. Gee, C. Reeps, J. Pongratz, H.-H. Eckstein, and W.A. Wall. A comparison of diameter, wall stress, and rupture potential index for abdominal aortic aneurysm rupture risk prediction. *Annals of Biomedical Engineering*, 38(10):3124–3134, 2010. doi:10.1007/s10439-010-0067-6.

D.A. Vorp. Biomechanics of abdominal aortic aneurysm. *Journal of Biomechanics*, 40(9):1887–1902, 2007. doi:http://dx.doi.org/10.1016/j.jbiomech.2006.09.003.

K. Khanafer, A. Duprey, M. Zainal, M. Schlicht, D. Williams, and R. Berguer. Determination of the elastic modulus of ascending thoracic aortic aneurysm at different ranges of pressure using uniaxial tensile testing. *The Journal of Thoracic and Cardiovascular Surgery*, 142 (3):682–686, 2011. ISSN 0022-5223. doi:https://doi.org/10.1016/j.jtcvs.2010.09.068. URL https://www.sciencedirect.com/science/article/pii/S0022522311004259.

M. Di Giuseppe, G. Alotta, V. Agnese, D. Bellavia, G.M. Raffa, V. Vetri, M. Zingales, S. Pasta, and M. Pilato. Identification of circumferential regional heterogeneity of ascending thoracic aneurysmal aorta by biaxial mechanical testing. *Journal of Molecular and Cellular Cardiology*, 130:205–215, 2019. doi:10.1016/j.yjmcc.2019.04.010.

G. Sommer, S. Sherifova, P.J. Oberwalder, O.E. Dapunt, P.A. Ursomanno, A. DeAnda, B.E. Griffith, and G.A. Holzapfel. Mechanical strength of aneurysmatic and dissected human thoracic aortas at different shear loading modes. *Journal of Biomechanics*, 49(12):2374–2382, 2016. doi:10.1016/j.jbiomech.2016.02.042.

A. Duprey, O. Trabelsi, M. Vola, J.P. Favre, and S. Avril. Biaxial rupture properties of ascending thoracic aortic aneurysms. *Acta Biomaterialia*, 42:273–285, 2016. ISSN 1742-7061. doi:https://doi.org/10.1016/j.actbio.2016.06.028. URL https://www.sciencedirect.com/science/article/pii/S1742706116303051.

G. Sommer, A. Schriefl, G. Zeindlinger, A. Katzensteiner, H. Ainödhofer, A. Saxena, and G.A. Holzapfel. Multiaxial mechanical response and constitutive modeling of esophageal tissues: Impact on esophageal tissue engineering. *Acta Biomaterialia*, 9(12):9379–9391, 2013. doi:10.1016/j.actbio.2013.07.041.

J.-H. Kim, P. Badel, A. Duprey, J. P. Favre, and S. Avril. Characterisation of failure in human aortic tissue using digital image correlation. *Computer Methods in Biomechanics and Biomedical Engineering*, 14(sup1):73–74, 2011a. doi:10.1080/10255842.2011.592368.

J.H. Kim, S. Avril, A. Duprey, and J.P. Favre. Experimental characterization of rupture in human aortic aneurysms using full-field measurement technique. *Biomechanics and modeling in mechanobiology*, 11:841–853, 11 2011b. doi:10.1007/s10237-011-0356-5.

F.M. Davis, Y. Luo, S. Avril, A. Duprey, and J. Lu. Pointwise characterization of the elastic properties of planar soft tissues: application to ascending thoracic aneurysms. *Biomechanics and Modeling in Mechanobiology*, 14(5):967–978, 2015. doi:10.1007/s10237-014-0646-9.

F. Davis, Y. Luo, S. Avril, A. Duprey, and J. Lu. Local mechanical properties of human ascending thoracic aneurysms. *Journal of the Mechanical Behavior of Biomedical Materials*, 61:235–249, 2016. doi:10.1016/j.jmbbm.2016.03.025.

O. Trabelsi, F.M. Davis, J.F. Rodriguez-Matas, A. Duprey, and S. Avril. Patient specific stress and rupture analysis of ascending thoracic aneurysms. *Journal of Biomechanics*, 48(10):1836–1843, 2015. ISSN 0021-9290. doi:https://doi.org/10.1016/j.jbiomech.2015.04.035.

X. He, S. Avril, and J. Lu. Estimating aortic thoracic aneurysm rupture risk using tension–strain data in physiological pressure range: an in vitro study. *Biomechanics and Modeling in Mechanobiology*, 20(2):683–699, 2021. doi:10.1007/s10237-020-01410-8.

A. M. Felfelian, A.B. Najar, R. J. Nedoushan, and H. Salehi. Determining constitutive behavior of the brain tissue using digital image correlation and finite element modeling. *Biomechanics and Modeling in Mechanobiology*, 18(6):1927–1945, 2019. doi:10.1007/s10237-019-01186-6.

X. Zhao, M.L. Raghavan, and J. Lu. Identifying heterogeneous anisotropic properties in cerebral aneurysms: a pointwise approach. *Biomechanics and Modeling in Mechanobiology*, 10(2):177–189, 2011. doi:10.1007/s10237-010-0225-7.

J. Lu, X. Zhou, and M.L. Raghavan. Inverse method of stress analysis for cerebral aneurysms. *Biomechanics and Modeling in Mechanobiology*, 7(6):477–486, 2008. doi:10.1007/s10237-007-0110-1.

J. Jansson, J. Olofsson, and K. Salomonsson. Simulation-driven product development of cast components with allowance for process-induced material behaviour. *Journal of Computational Design and Engineering*, 7(1):78–85, 03 2020. doi:10.1093/jcde/qwaa008.

S. Nikolaev, M. Gusev, D. Padalitsa, E. Mozhenkov, S. Mishin, and I. Uzhinsky. Implementation of "digital twin" concept for modern project-based engineering education. In Paolo Chiabert, Abdelaziz Bouras, Frédéric Noël, and José Ríos, editors, *Product Lifecycle Management to Support Industry 4.0*, pages 193–203, Cham, 2018. Springer International Publishing. ISBN 978-3-030-01614-2.

T. Sravan, N. R. Suddapalli, P. Johan, S. Mats, and J. Christian. Simulation-driven design approach for design and optimization of blankholder. *Journal of Physics: Conference Series*, 896:012045, sep 2017. doi:10.1088/1742-6596/896/1/012045. URL https://doi.org/10.1088/1742-6596/896/1/012045.

www.encyclopedia.lubopitko-bg.com Corporation. Systemic arteries. URL https://encyclopedia.lubopitko-bg.com/Systemic_Arteries.html. [Online image].

J. Elefteriades. Thoracic aortic aneurysm: Reading the enemy's playbook. *Current Problems in Cardiology*, 33(5):203–277, 2008. doi:10.1016/j.cpcardiol.2008.01.004.

T.C. Gasser. Chapter 8 - aorta. In Yohan Payan and Jacques Ohayon, editors, *Biomechanics of Living Organs*, volume 1 of *Translational Epigenetics*, pages 169–191. Academic Press, Oxford, 2017. doi:10.1016/B978-0-12-804009-6.00008-0.

R. Bergman, A. Afifi, and P. Heidger. Plate 8.152 aorta. *Anatomy Atlases*, Atlas of Microscopic Anatomy: Section 8 - Cardiovascular System. URL https://www.anatomyatlases.org/MicroscopicAnatomy/Section08/Plate08152.shtml. [Online image].

UAB Medicine. Aortic aneurysm. URL https://www.uabmedicine.org/patient-care/conditions/aneurysm. [Online image].

D. Szalay and M. Frołow. Aortic aneurysms. *McMaster Textbook of Internal Medicine*, Kraków: Medycyna Praktyczna, 2019. URL https://empendium.com/mcmtextbook/chapter/B31.II.2.22. [Online image].

J.T. Powell, S.M. Gotensparre, M. Sweeting, L.C. Brown, F.G.R. Fowkes, and S.G. Thompson. Rupture rates of small abdominal aortic aneurysms: A systematic review of the literature. *European journal of vascular and endovascular surgery : the official journal of the European Society for Vascular Surgery*, 41:2–10, 10 2010. doi:10.1016/j.ejvs.2010.09.005.

T. McGloughlin. *Biomechanics and Mechanobiology of Aneurysms*. Springer Berlin, 2011.

D. Vorp, Madhavan Raghavan, Satish Muluk, MICHEL MAKAROUN, DAVID STEED, RON SHAPIRO, and MARSHALL WEBSTER. Wall strength and stiffness of aneurysmal and nonaneurysmal abdominal aorta. *Annals of the New York Academy of Sciences*, 800:274 – 276, 12 2006. doi:10.1111/j.1749-6632.1996.tb33330.x.

F. Cosentino, V. Agnese, G.M. Raffa, G. Gentile, D. Bellavia, M. Zingales, M. Pilatom, and S. Pasta. On the role of material properties in ascending thoracic aortic aneurysms. *Computers in Biology and Medicine*, 109:70–78, 2019. ISSN 0010-4825. doi:10.1016/j.compbiomed.2019.04.022.

K. Miller and J. Lu. On the prospect of patient-specific biomechanics without patient-specific properties of tissues. *Journal of the mechanical behavior of biomedical materials*, 27, 02 2013. doi:10.1016/j.jmbbm.2013.01.013.

G. Joldes, K. Miller, A. Wittek, and B. Doyle. A simple, effective and clinically applicable method to compute abdominal aortic aneurysm wall stress. *Journal of the Mechanical Behavior of Biomedical Materials*, 58, 08 2015. doi:10.1016/j.jmbbm.2015.07.029.

K. Lameka, M. D. Farwell, and M. Ichise. Chapter 11 - positron emission tomography. In Joseph C. Masdeu and R. Gilberto González, editors, *Neuroimaging Part I*, volume 135 of *Handbook of Clinical Neurology*, pages 209–227. Elsevier, 2016. doi:https://doi.org/10.1016/B978-0-444-53485-9.00011-8. URL https://www.sciencedirect.com/science/article/pii/B9780444534859000118.

N. Sakalihasan, R. Hustinx, and R. Limet. Contribution of pet scanning to the evaluation of abdominal aortic aneurysm. *Seminars in vascular surgery*, 17:144–53, 07 2004. doi:10.1053/j.semvascsurg.2004.03.002.

J. Kim and H.-C. Song. Role of pet/ct in the evaluation of aortic disease. *Chonnam Medical Journal*, 54:143, 09 2018. doi:10.4068/cmj.2018.54.3.143.

J.H.F. Rudd, P. A. Coughlin, and A. M. Groves. Predicting aortic aneurysm expansion by pet. *Journal of Nuclear Medicine*, 56(7):971–973, 2015. ISSN 0161-5505. doi:10.2967/jnumed.115.154062. URL https://jnm.snmjournals.org/content/56/7/971.

A. Evangelista. Imaging aortic aneurysmal disease. *Heart*, 100(12):909–915, 2014. doi:10.1136/heartjnl-2013-305048.

A. Harkness. Echocardiogram – part 1: Why do i have to have an echocardiogram? 2018. URL https://www.topdoctors.co.uk/medical-articles/echocardiogram-part-1-why-do-i-have-to-have-an-echocardiogram. [Online image].

Go Imaging. CTA. URL https://go-imaging.com/services/cta/. [Online image].

H. Gharbia. Radiopaedia. *Cystic hygroma - chest wall*. URL https://radiopaedia.org/cases/cystic-hygroma-chest-wall. [Online image].

V.L. Nguyen, T. Leiner, F.A.M.V.I. Hellenthal, W.H. Backes, M.C.J. Wishaupt, R.J. van der Geest, S. Heeneman, M.E. Kooi, and G.W.H. Schurink. Abdominal aortic aneurysms with high thrombus signal intensity on magnetic resonance imaging are associated with high growth rate. *European Journal of Vascular and Endovascular Surgery*, 48(6):676–684, 2014. doi:10.1016/j.ejvs.2014.04.025.

M. Auer, R. Stollberger, P. Regitnig, F. Ebner, and G.A. Holzapfel. 3-d reconstruction of tissue components for atherosclerotic human arteries using ex vivo high-resolution mri. *IEEE Transactions on Medical Imaging*, 25(3):345–357, 2006. doi:10.1109/TMI.2006.870485.

Z. Domagała, H. Stępak, P. Drapikowski, A. Kociemba, M. Pyda, K. Karmelita-Katulska, L. Dzieciuchowicz, and G. Oszkinis. Geometric verification of the validity of finite element method analysis of abdominal aortic aneurysms based on magnetic resonance imaging. *Biocybernetics and Biomedical Engineering*, 38(3):544–555, 2018. doi:10.1016/j.bbe.2018.04.001.

B. J. Doyle, L. G. Morris, A. Callanan, P. Kelly, D. A. Vorp, and T. M. McGloughlin. 3d reconstruction and manufacture of real abdominal aortic aneurysms: From ct scan to silicone model. *Journal of Biomechanical Engineering*, 130(3), 2008. doi:10.1115/1.2907765.

A. Wittek, K. Karatolios, P. Bihari, T. Schmitz-Rixen, R. Moosdorf, S. Vogt, and C. Blase. In vivo determination of elastic properties of the human aorta based on 4d ultrasound data. *Journal of the Mechanical Behavior of Biomedical Materials*, 27:167–183, 2013. doi:10.1016/j.jmbbm.2013.03.014.

X. Wang and X. Li. Computational simulation of aortic aneurysm using fsi method: Influence of blood viscosity on aneurismal dynamic behaviors. *Computers in Biology and Medicine*, 41 (9):812–821, 2011. ISSN 0010-4825. doi:10.1016/j.compbiomed.2011.06.017.

N.T. Philip, B.S.V. Patnaik, and B.J. Sudhir. Hemodynamic simulation of abdominal aortic aneurysm on idealised models: Investigation of stress parameters during disease progression. *Computer Methods and Programs in Biomedicine*, 213:106508, 2022. ISSN 0169-2607. doi:10.1016/j.cmpb.2021.106508.

G.A. Holzapfel, T.C. Gasser, and R.W. Ogden. A new constitutive framework for arterial wall mechanics and a comparative study of material models. *Journal of Elasticity*, 61(1-3):1–48, 2000. doi:10.1023/A:1010835316564.

Gyung-Jin Park. Analytic methods for design practice. *Analytic Methods for Design Practice*, 01 2007. doi:10.1007/978-1-84628-473-1.

A. Dagman and R. Söderberg. Toward a method for improving product architecture solutions by integrating designs for assembly, disassembly and maintenance. volume 3, 11 2012. doi:10.1115/IMECE2012-87466.

V. Mendez, M. Di Giuseppe, and S. Pasta. Comparison of hemodynamic and structural indices of ascending thoracic aortic aneurysm as predicted by 2-way fsi, cfd rigid wall simulation and patient-specific displacement-based fea. *Computers in Biology and Medicine*, 100:221–229, 2018. ISSN 0010-4825. doi:10.1016/j.compbiomed.2018.07.013.

ISO. Iso 129-1:2018. 2018. URL https://www.iso.org/standard/64007.html.

SFK. Industrial shaft seals. SE/P1 18729 EN, 2019. URL https://www.skf.com/group/products/industrial-seals/power-transmission-seals/radial-shaft-seals.

infomech. Fundamental deviations letter for hole and shaft basis, December 2014. URL http://mecaninfo.blogspot.com/2014/12/fundamental-deviations-letter-for-hole.html.

K. Adistambha, S. Davis, C. Ritz, I. Burnett, and D. Stirling. *Enhancing Multimedia Search Using Human Motion*. 03 2012. ISBN 978-953-51-0216-8. doi:10.5772/36585.

M. Mooney. A theory of large elastic deformation. *Journal of Applied Physics*, 11(9):582–592, 1940. doi:10.1063/1.1712836.

S. Ruiz de Galarreta, C. Aitor, R. Antón, and E. Finol. A methodology for verifying abdominal aortic aneurysm wall stress. *Journal of biomechanical engineering*, 139, 01 2017. doi:10.1115/1.4034710.

J. Bergström. 5 - elasticity/hyperelasticity. In Jörgen Bergström, editor, *Mechanics of Solid Polymers*, pages 209–307. William Andrew Publishing, 2015. ISBN 978-0-323-31150-2. doi:https://doi.org/10.1016/B978-0-323-31150-2.00005-4. URL https://www.sciencedirect.com/science/article/pii/B9780323311502000054.

Appendices

1 Technical drawings

In the following, the technical drawings of main parts of the device will be presented, as well as assembly drawings:

1. Drawing DM-1
2. Drawing DM-2
3. Drawing DM-3
4. Drawing DM-4
5. Drawing DM-5
6. Drawing DM-6
7. Drawing DM-7
8. Drawing DM-8
9. Drawing DM-9
10. Drawing DM-10
11. Drawing DM-11
12. Drawing DM-12
13. Drawing DM-13
14. Drawing DM-14
15. Drawing DM-15
16. Drawing DM-16
17. Drawing DM-17
18. Drawing DM-18
19. Drawing DM-19
20. Drawing DM-20
21. Drawing DM-21
22. Drawing DM-22
23. Drawing DM-23
24. Drawing DM-24
25. Drawing DM-25

26. Drawing DM-26
27. Drawing DM-27
28. Drawing DM-28
29. Drawing DM-S1
30. Drawing DM-S2
31. Drawing DM-S3
32. Drawing DM-S4
33. Drawing DM-S5
34. Drawing DM-S6

Designed	19/11/21	
Drawn	19/11/21	
Copied	19/11/21	
Verified		

2

Master's Dissertation

Testing device for an anatomical part

Francisco Castanho
Nº51959

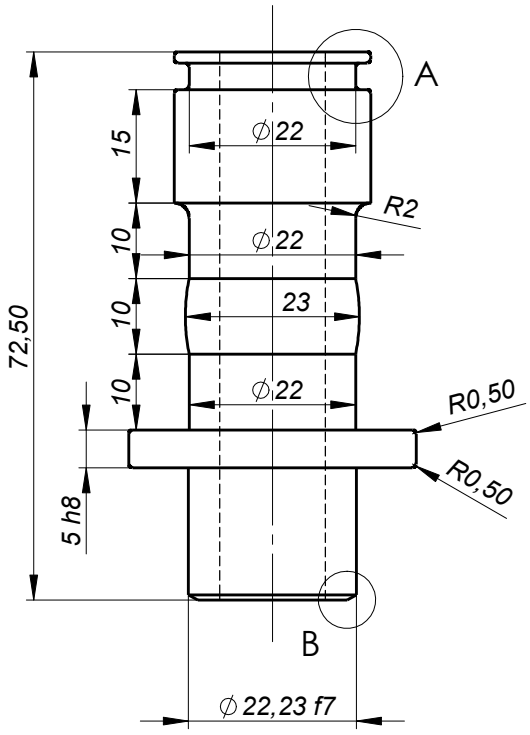

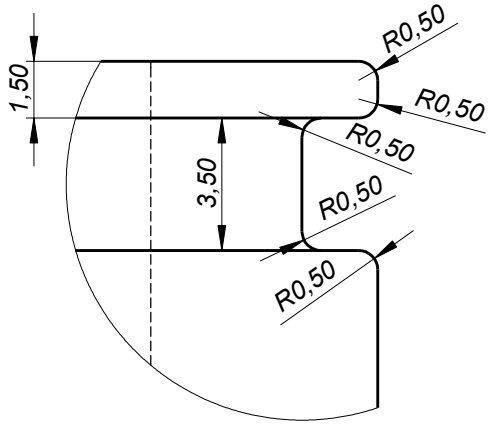

DETAIL A
SCALE 5 : 1

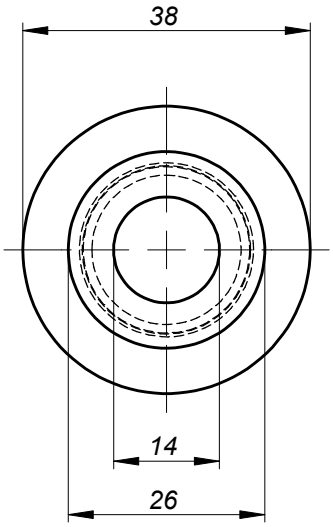

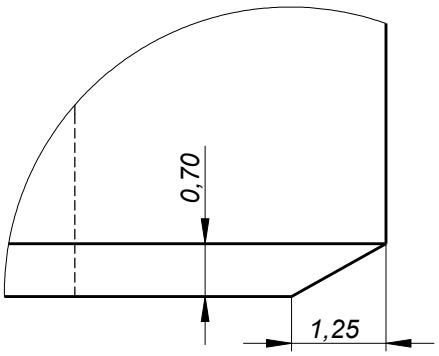

DETAIL B
SCALE 10 : 1

Observations:	*1:1*	*Fixation part*	*DM-1*
Material: AISI 316	*Toleran.*		
	ISO 2768-1: 1989 Medium		

Designed	19/11/21		*Master's Dissertation*	*Francisco Castanho*
Drawn	19/11/21		*Testing device for an anatomical part*	*Nº51959*
Copied	19/11/21			
Verified				

3

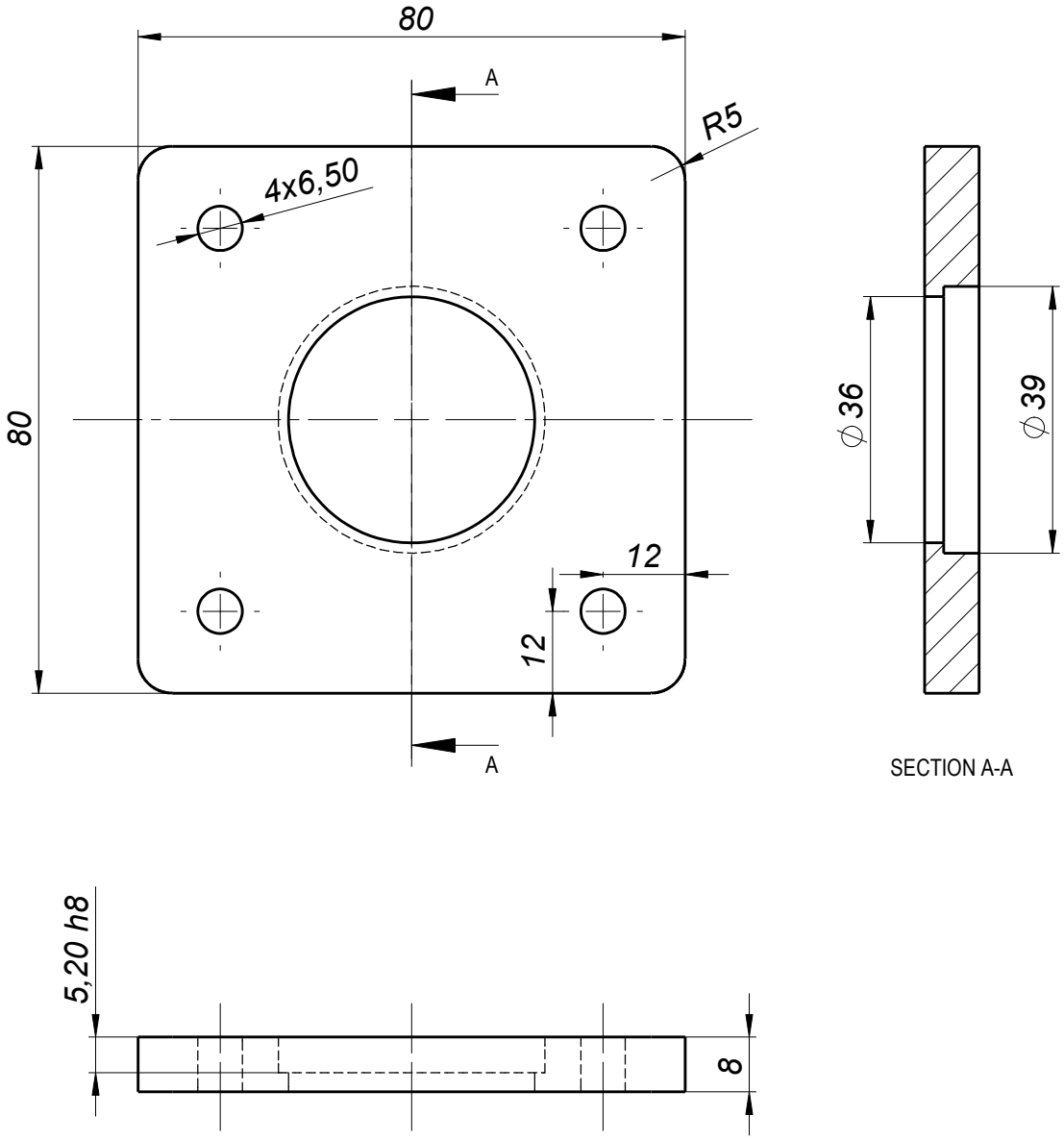

Observations:	*1:1*	*Fixation part locker*	*DM-2*
Material: *AISI 316*	*Toleran.* *ISO 2768-1: 1989 Medium*		

4

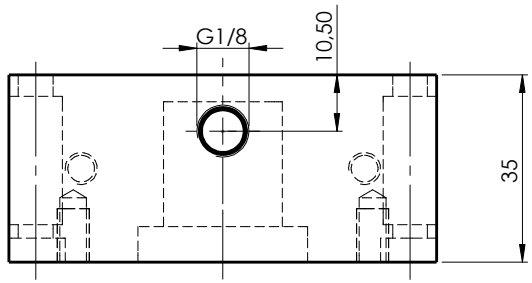

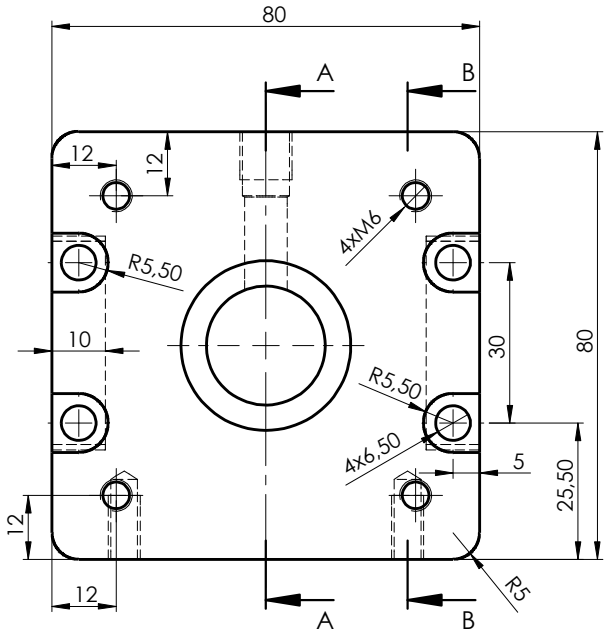

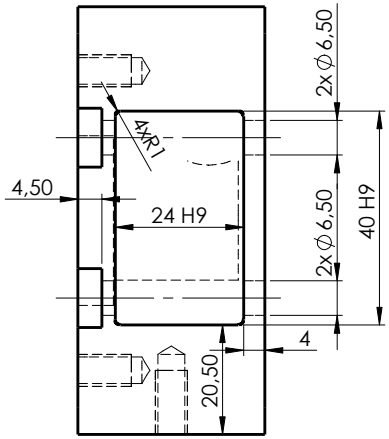

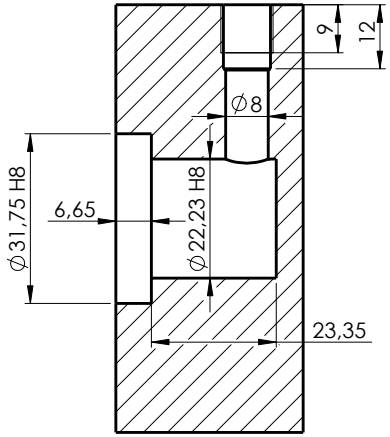

SECTION A-A

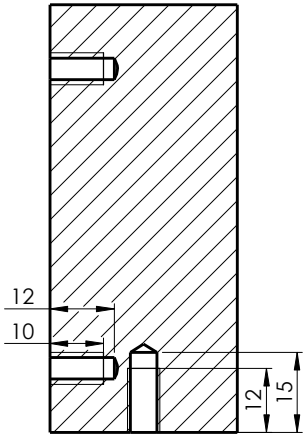

SECTION B-B

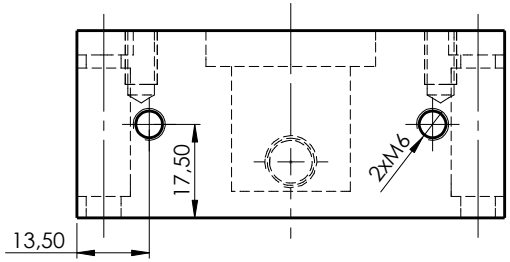

Observations:	Designed	19/11/21	Master's Dissertation Testing device for an anatomical part	Francisco Castanho Nº 51959	
	Drawn	19/11/21			
	Copied	19/11/21			
	Verified				
Material: AISI 316	1:1		Connector block	DM-3	
	Toleranc. ISO 2768-1: 1989 Medium				

Designed	19/11/21	
Drawn	19/11/21	
Copied	19/11/21	
Verified		

Master's Dissertation

Testing device for an anatomical part

Francisco Castanho
Nº51959

5

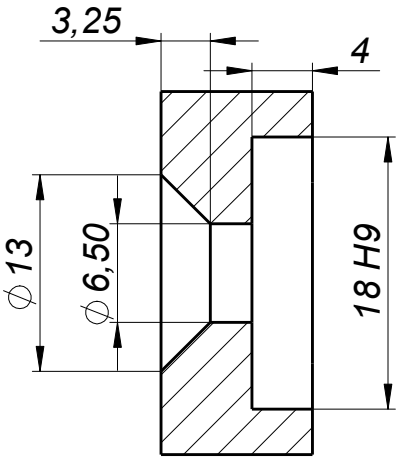

SECTION A-A

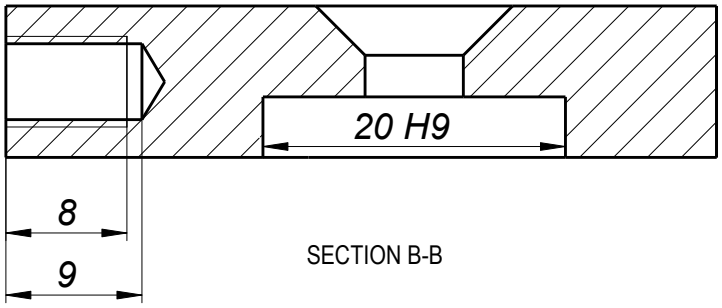

SECTION B-B

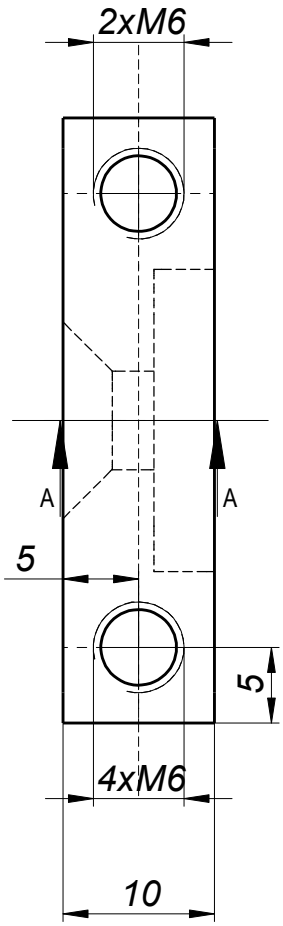

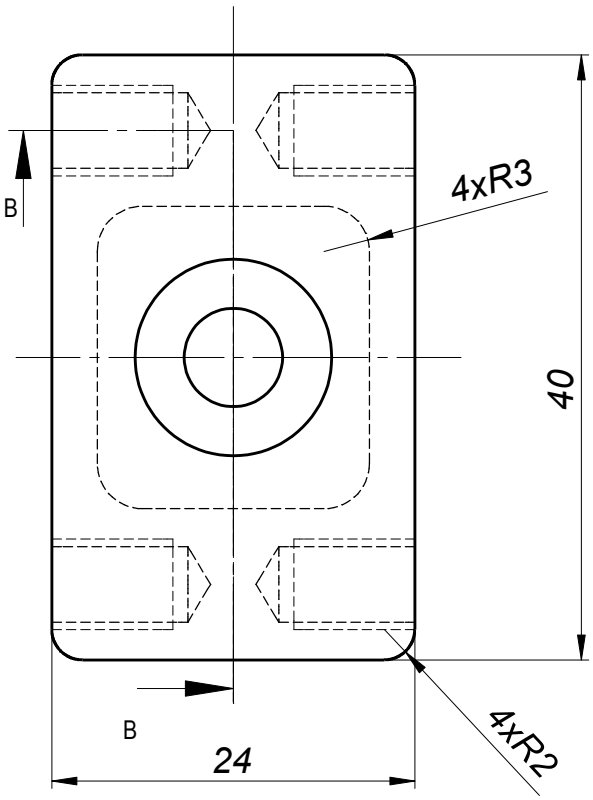

Observations:	*2:1*	*Connector arm -1*	*DM-4*
Material: *AISI 316*	*Toleran.* *ISO 2768-1: 1989 Medium*		

Designed	19/11/21		Master's Dissertation Testing device for an anatomical part	Francisco Castanho Nº51959
Drawn	19/11/21			
Copied	19/11/21			
Verified				

6

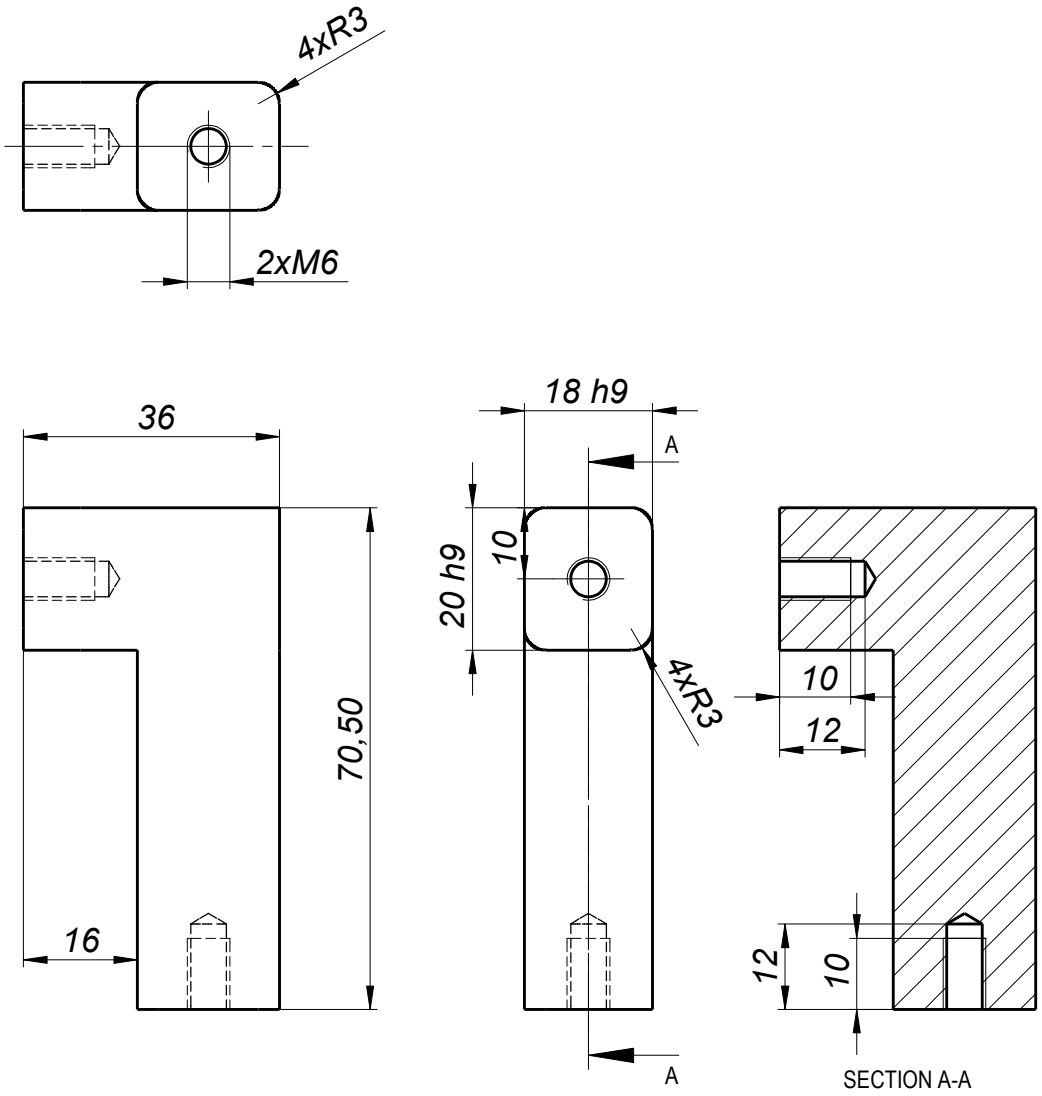

Observations: Material: AISI 316	1:1 Toleran. ISO 2768-1: 1989 Medium	Connector arm-2	DM-5

Designed	19/11/21		Master's Dissertation Testing device for an anatomical part	Francisco Castanho Nº51959
Drawn	19/11/21			
Copied	19/11/21			
Verified				

7

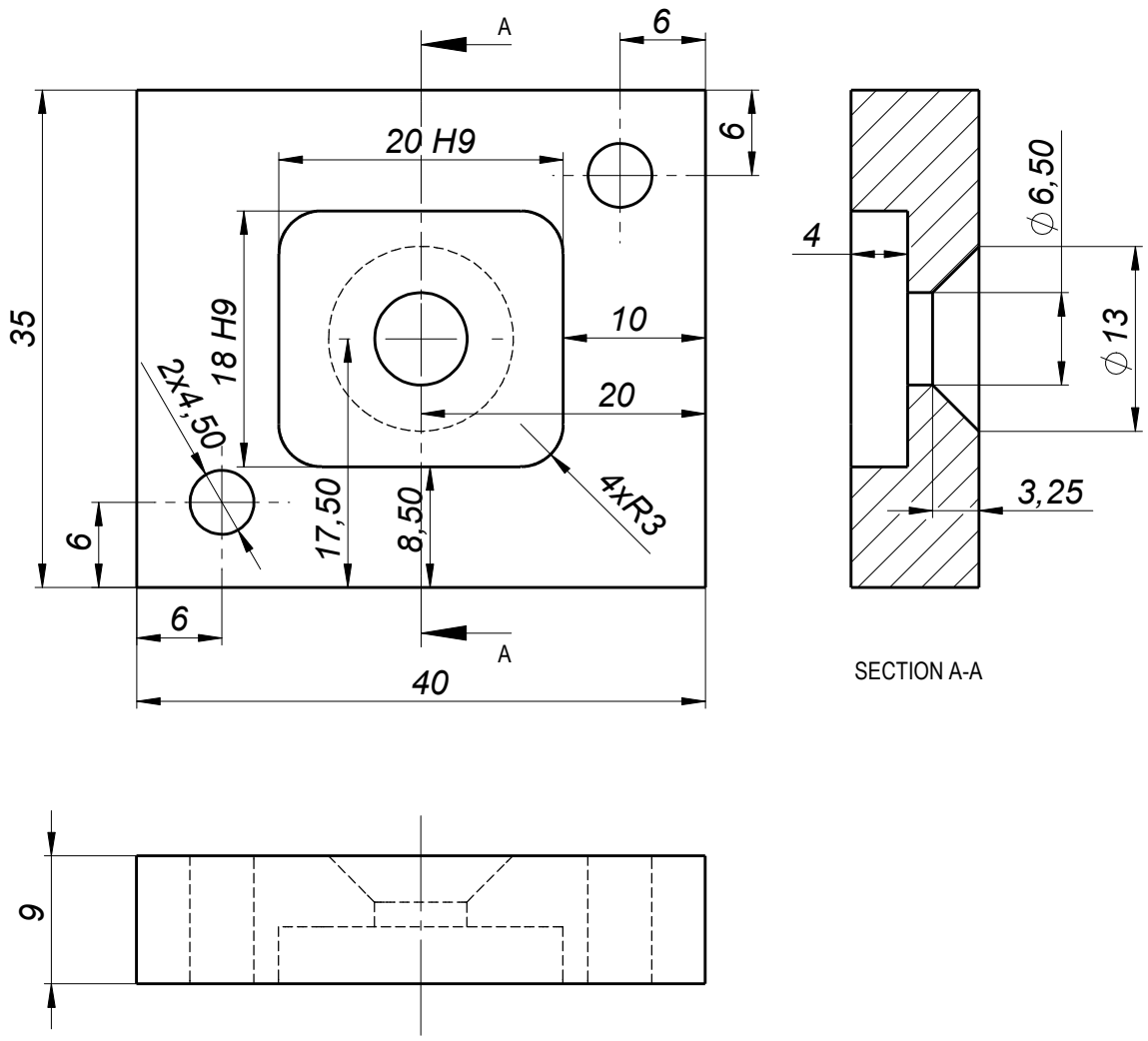

Observations: Material: AISI 316	2:1 Toleran. ISO 2768-1: 1989 Medium	Connector arm-3	DM-6

Designed	19/11/21	
Drawn	19/11/21	
Copied	19/11/21	
Verified		

Master's Dissertation

Testing device for an anatomical part

Francisco Castanho
Nº51959

8

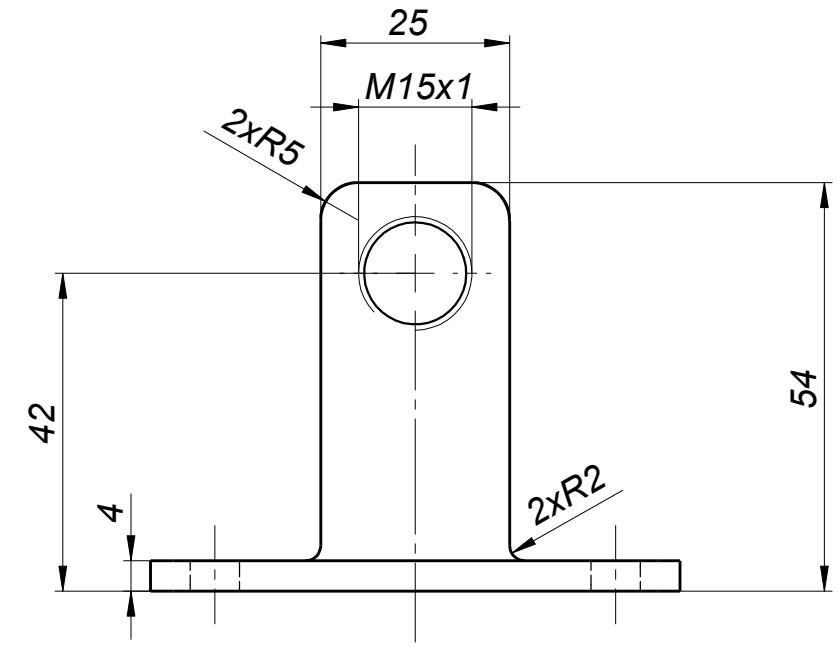

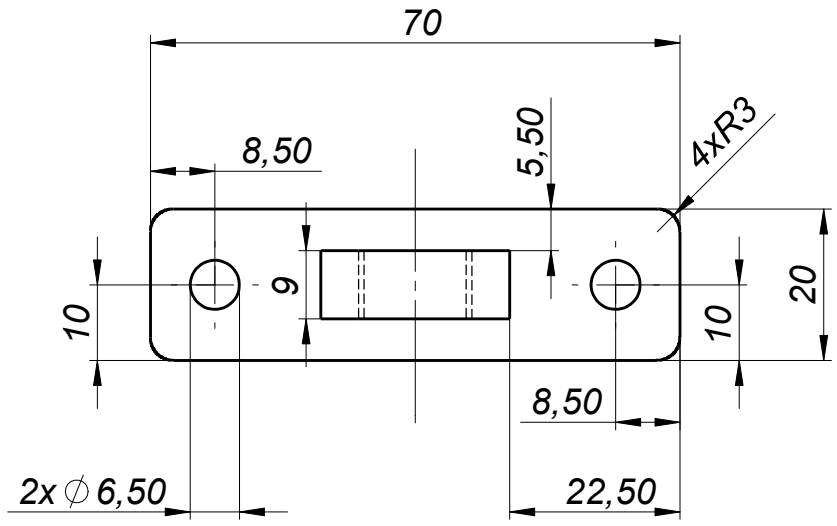

Observations:	1:1	Ball screw nut holder	DM-7
Material: AISI 316	Toleran. ISO 2768-1: 1989 Medium		

Designed	19/11/21		Master's Dissertation Testing device for an anatomical part	Francisco Castanho Nº51959
Drawn	19/11/21			
Copied	19/11/21			
Verified				

9

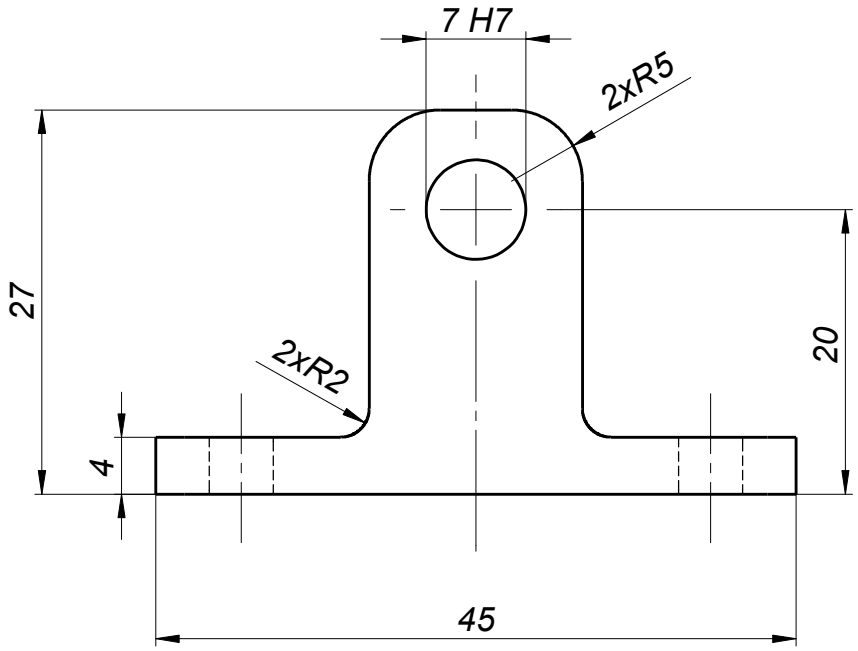

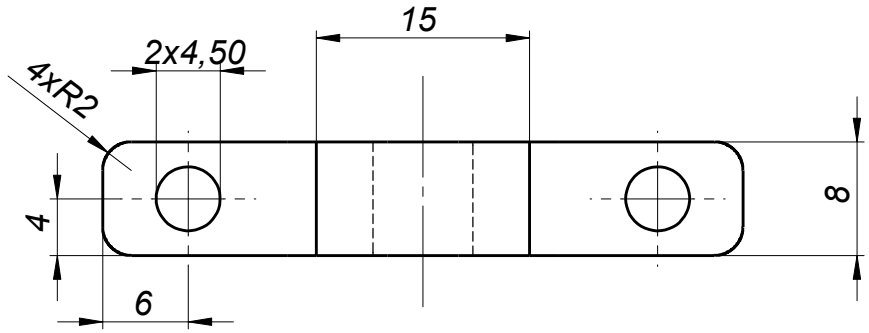

Observations: Material: AISI 316	2:1 Toleran. ISO 2768-1: 1989 Medium	Roller screw holder	DM-8

Designed	20/11/21	
Drawn	20/11/21	
Copied	20/11/21	
Verified		

Master's Dissertation

Testing device for an anatomical part

Francisco Castanho
Nº51959

10

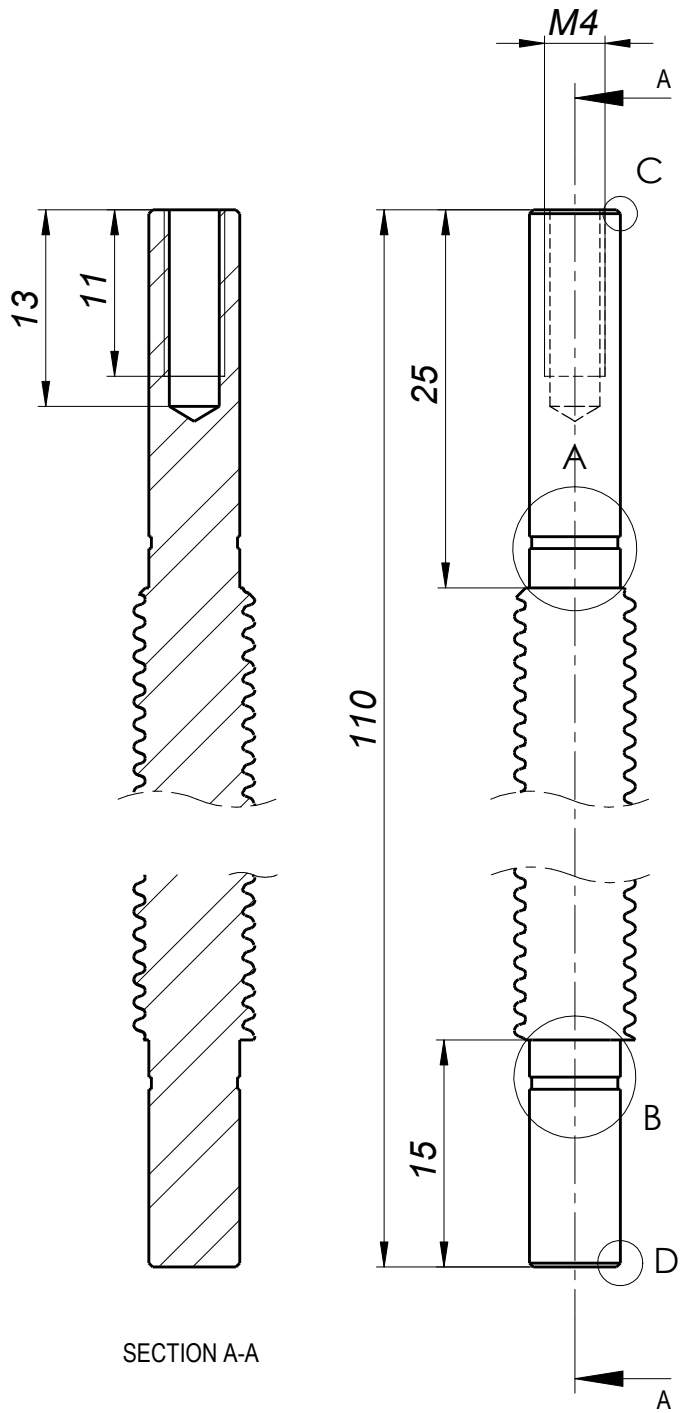

SECTION A-A

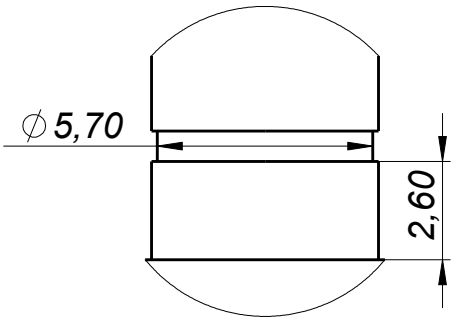

DETAIL A
SCALE 5 : 1

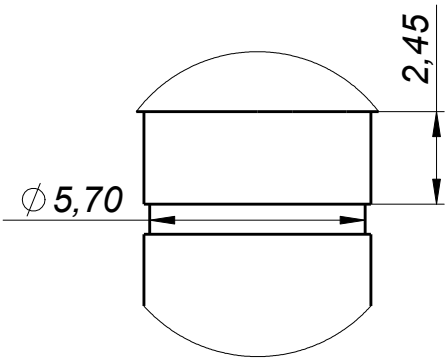

DETAIL B
SCALE 5 : 1

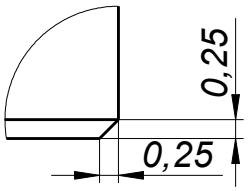

DETAIL D
SCALE 10 : 1

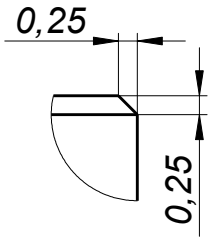

DETAIL C
SCALE 10 : 1

Observations:

Shaft ends for SKF ball screw.
Ordering Key:
BDS 8x2,5 R 70/110 G7 L

2:1

Toleran.

ISO 2768-1: 1989
Medium

Ball screw

DM-9

Designed	20/11/21	
Drawn	20/11/21	
Copied	20/11/21	
Verified		

Master's Dissertation

Testing device for an anatomical part

Francisco Castanho
Nº51959

11

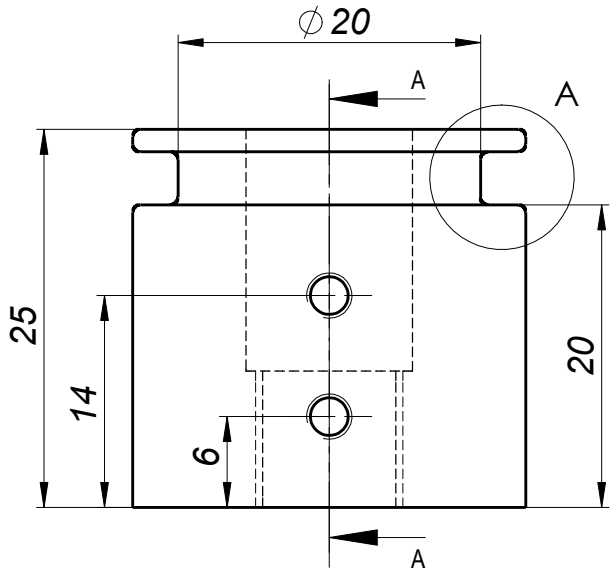

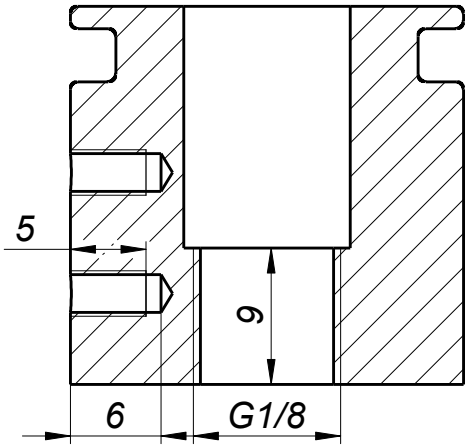

SECTION A-A

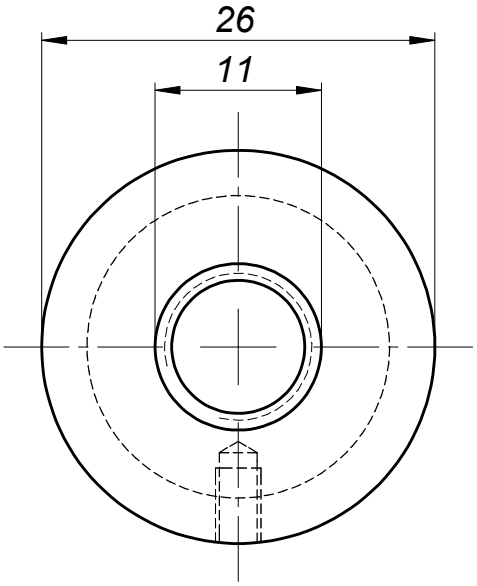

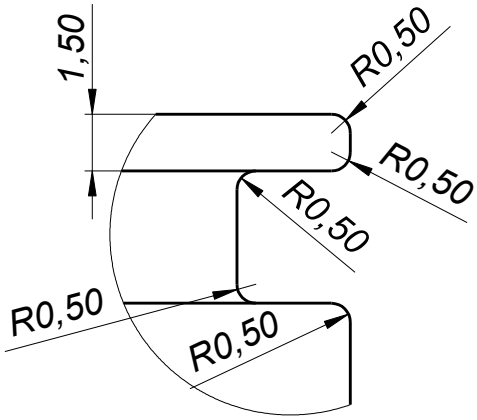

DETAIL A
SCALE 5 : 1

Observations:	*2:1*	*Fixation part (outlet side)*	*DM-10*
Material	*Toleran.*		
AISI 316	*ISO 2768-1: 1989 Medium*		

Designed	20/11/21	
Drawn	20/11/21	
Copied	20/11/21	
Verified		

NOVA School of Science and Technology

Master's Dissertation - Testing device for an anatomical part

Francisco Castanho
Nº51959

12

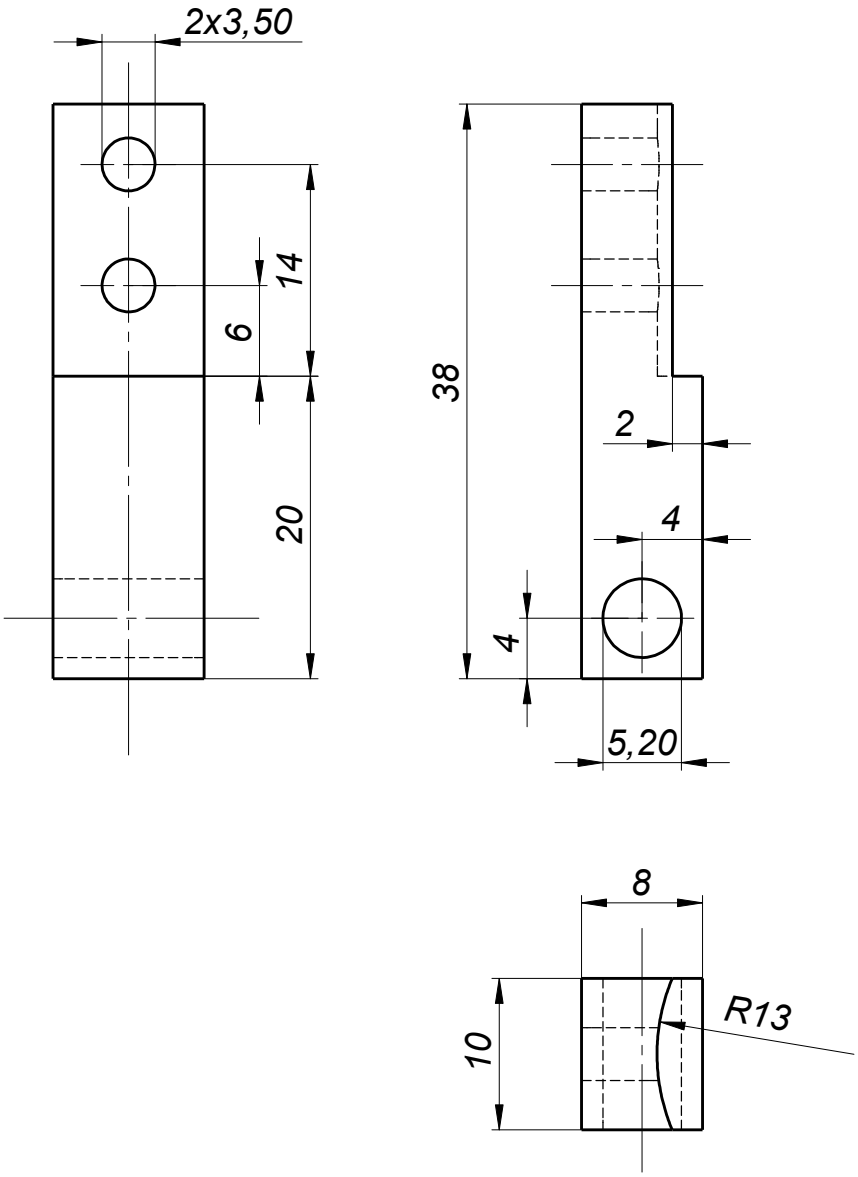

Observations:	2:1	Articulation connector - 1	DM-11
Material: AISI 316	Toleran. ISO 2768-1: 1989 Medium		

Designed	20/11/21	
Drawn	20/11/21	
Copied	20/11/21	
Verified		

NOVA School of Science and Technology

Master's Dissertation - Testing device for an anatomical part

Francisco Castanho
Nº51959

13

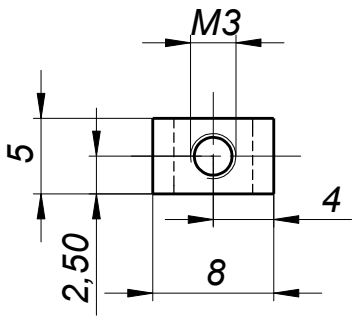

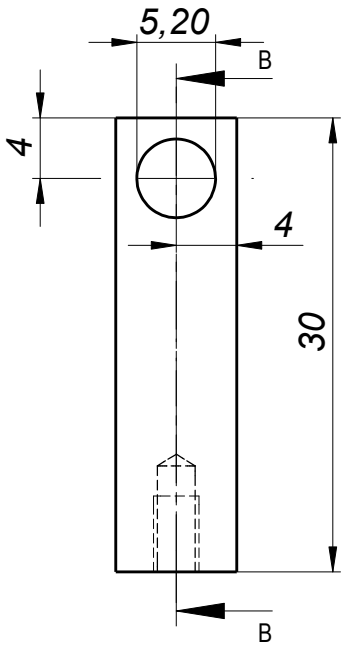

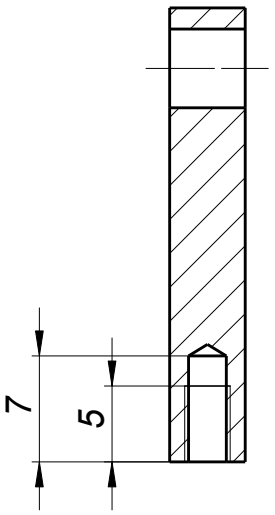

SECTION A-A

Observations:	2:1	Articulation connector - 2	DM-12
Material: AISI 316	Toleran. ISO 2768-1: 1989 Medium		

Designed	20/11/21	
Drawn	20/11/21	
Copied	20/11/21	
Verified		

NOVA School of Science and Technology

Master's Dissertation - Testing device for an anatomical part

Francisco Castanho
Nº51959

14

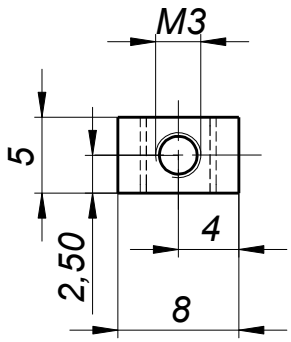

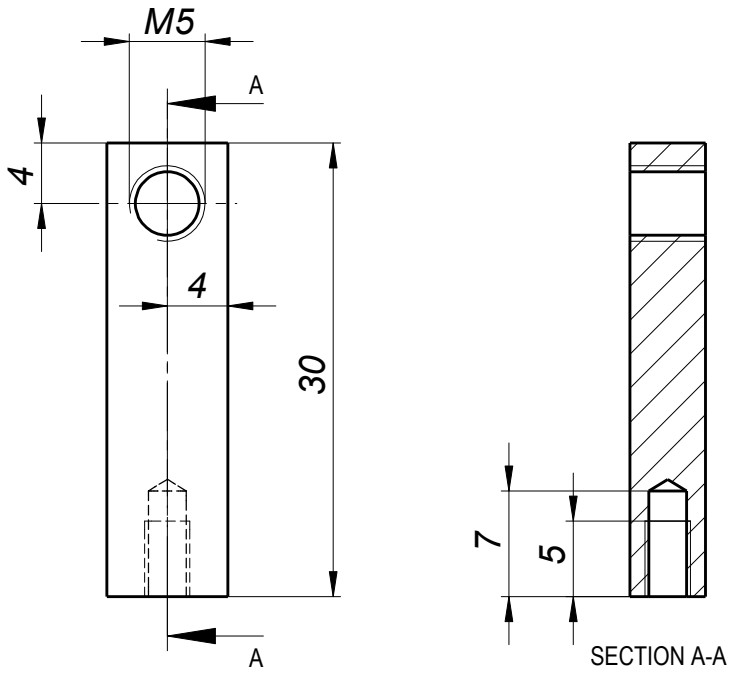

Observations:	2:1	Articulation connector - 3	DM-13
Material AISI 316	Toleran. ISO 2768-1: 1989 Medium		

Designed	20/11/21	
Drawn	20/11/21	
Copied	20/11/21	
Verified		

NOVA School of Science and Technology

Master's Dissertation - Testing device for an anatomical part

Francisco Castanho
Nº51959

15

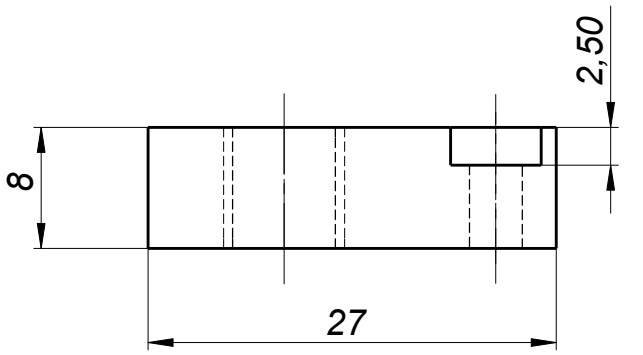

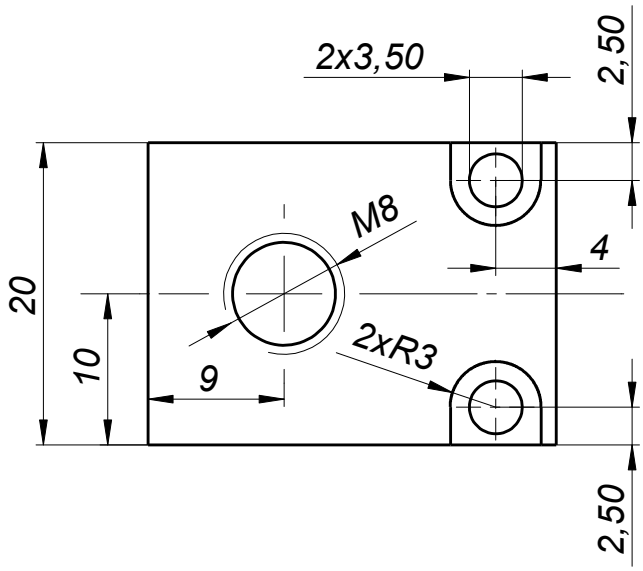

Observations: Material AISI 316	2:1 Toleran. ISO 2768-1: 1989 Medium	Slot connector	DM-14

Designed	20/11/21	
Drawn	20/11/21	
Copied	20/11/21	
Verified		

NOVA School of Science and Technology

Master's Dissertation - Testing device for an anatomical part

Francisco Castanho
Nº51959

16

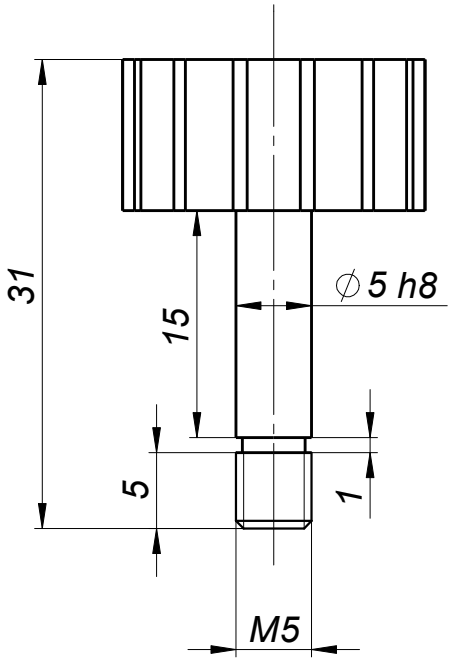

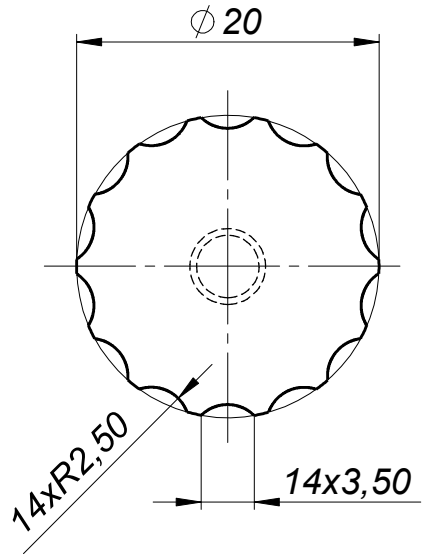

Observations: Material AISI 316	2:1 Toleran. ISO 2768-1: 1989 Medium	Hinge pin	DM-15

Designed	20/11/21	
Drawn	20/11/21	
Copied	20/11/21	
Verified		

17

NOVA School of Science and Technology

Master's Dissertation - Testing device for an anatomical part

Francisco Castanho
Nº51959

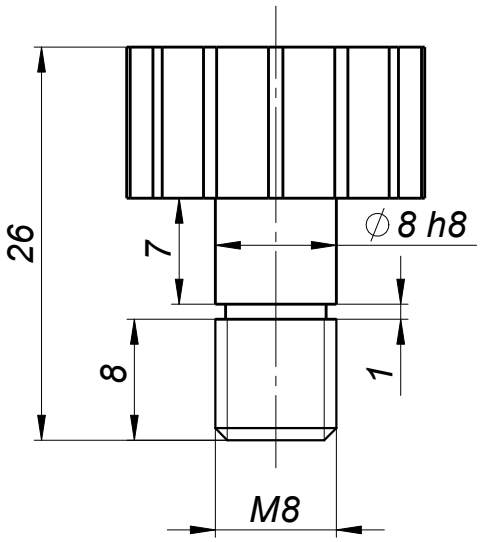

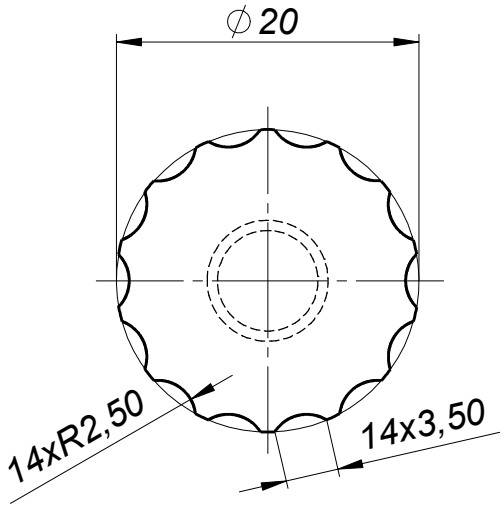

Observations: Material AISI 316	2:1 Toleran. ISO 2768-1: 1989 Medium	Slot screw	DM-16

Designed	20/11/21		NOVA School of Science and Technology	Francisco Castanho Nº51959
Drawn	20/11/21		Master's Dissertation - Testing device for an anatomical part	
Copied	20/11/21			
Verified				

18

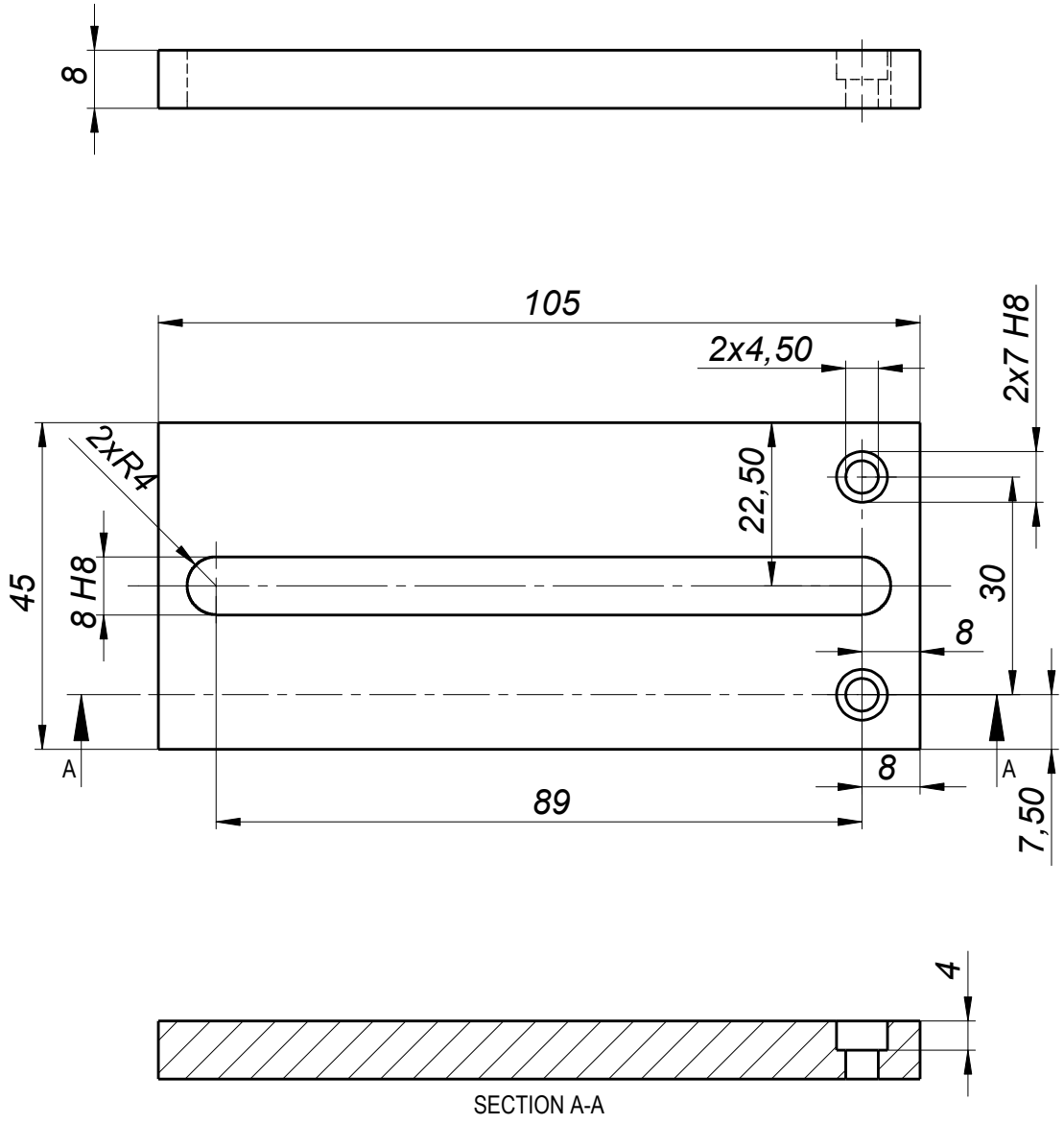

Observations: Material AISI 316	1:1 Toleran. ISO 2768-1: 1989 Medium	Connector with slot	DM-17

Designed	20/11/21	
Drawn	20/11/21	
Copied	20/11/21	
Verified		

NOVA School of Science and Technology

Master's Dissertation - Testing device for an anatomical part

Francisco Castanho
Nº51959

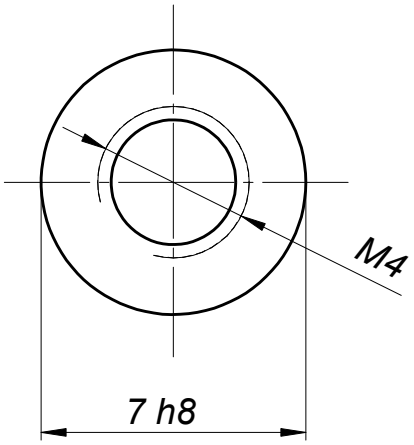

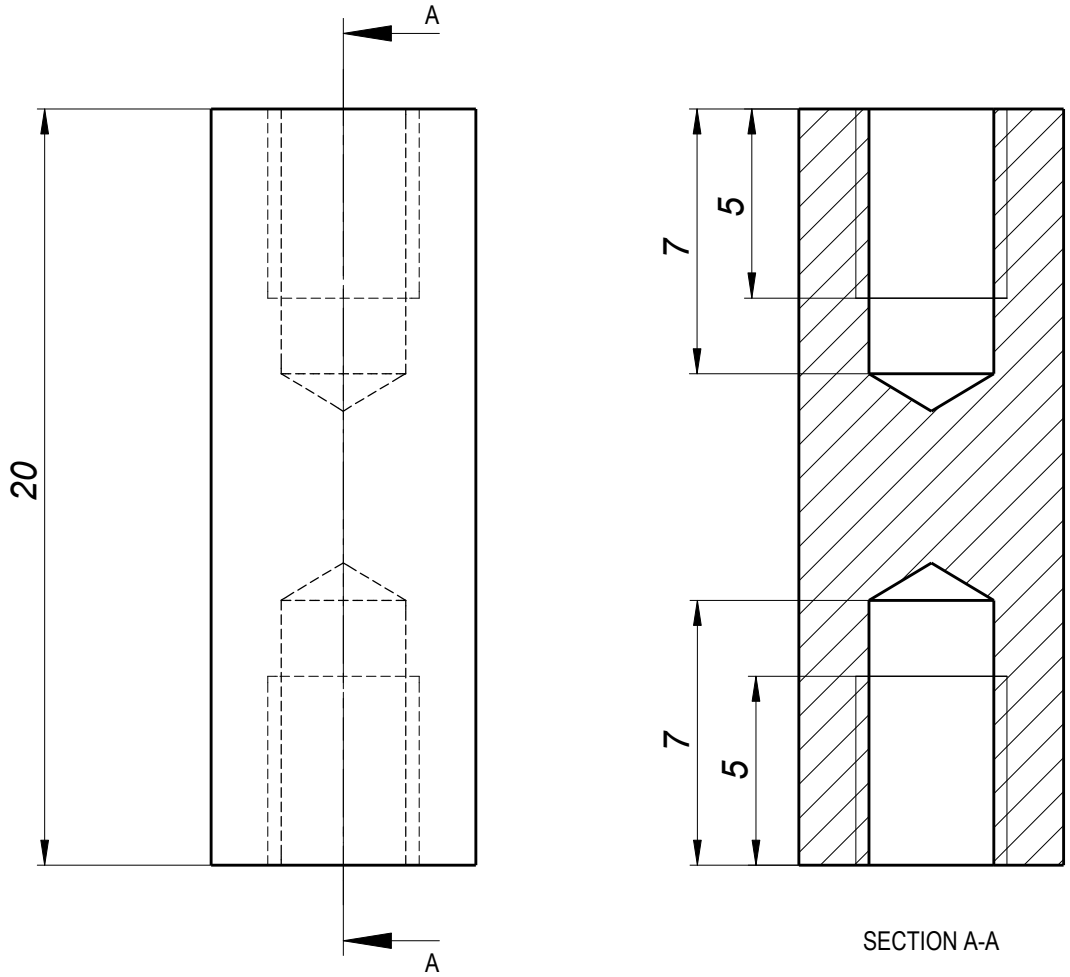

SECTION A-A

Observations: Material AISI 316	5:1 Toleran. ISO 2768-1: 1989 Medium	Flange connector rod	DM-18

Designed	20/11/21	
Drawn	20/11/21	
Copied	20/11/21	
Verified		

NOVA School of Science and Technology

Master's Dissertation - Testing device for an anatomical part

Francisco Castanho
Nº51959

20

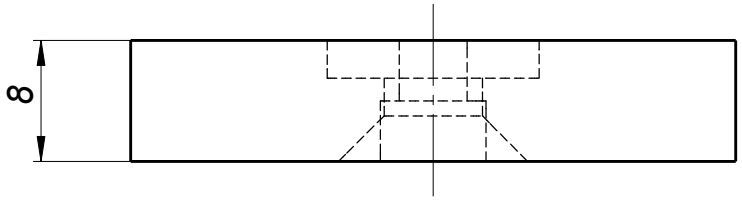

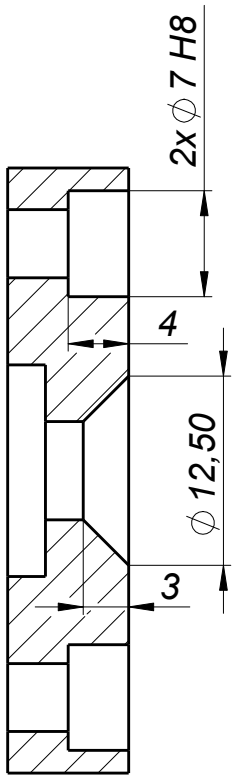

SECTION A-A

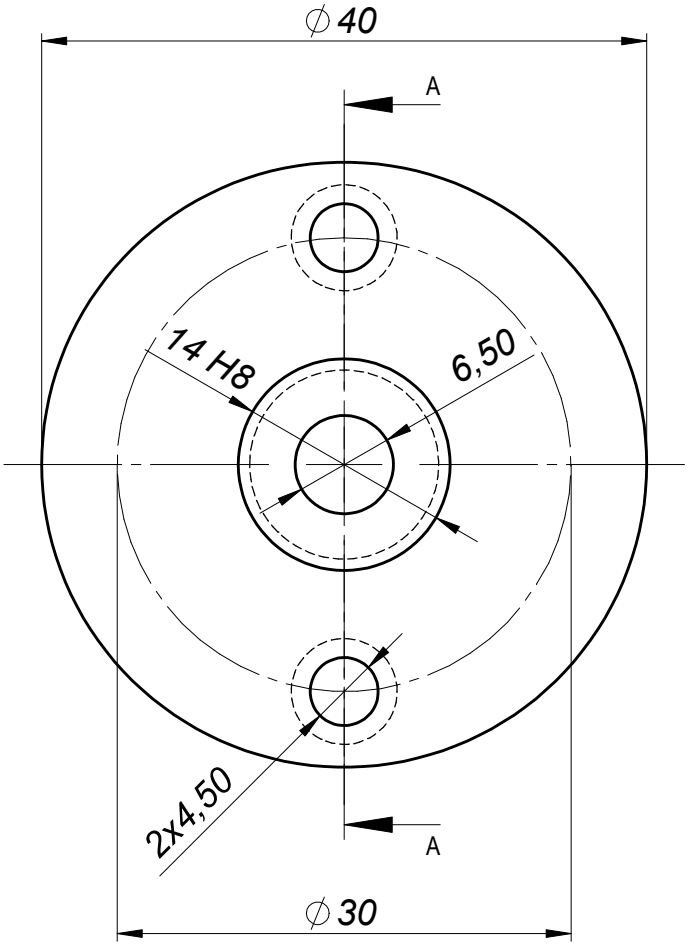

Observations: Material AISI 316	2:1 Toleran. ISO 2768-1: 1989 Medium	Flange	DM-19

Designed	21/11/21	
Drawn	21/11/21	
Copied	21/11/21	
Verified		

21

NOVA School of Science and Technology

Master's Dissertation - Testing device for an anatomical part

Francisco Castanho
Nº51959

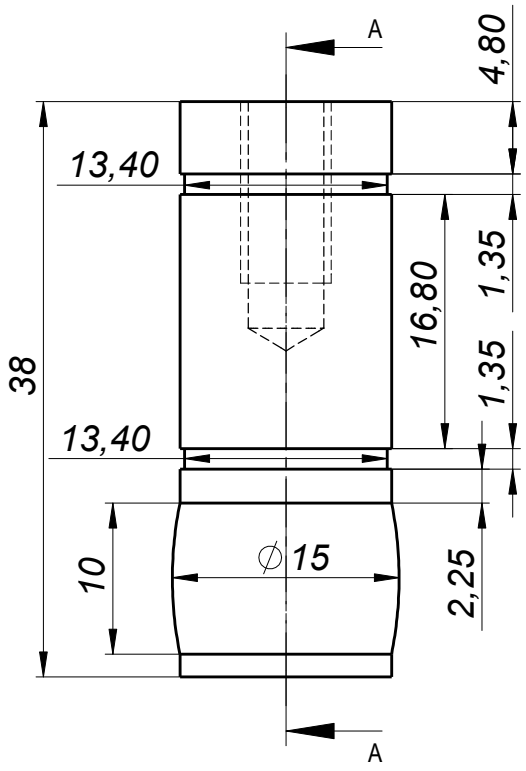

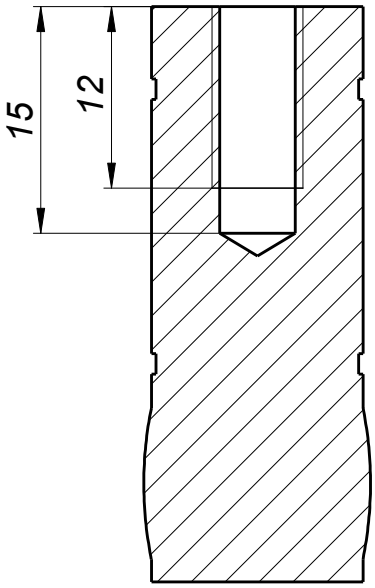

SECTION A-A

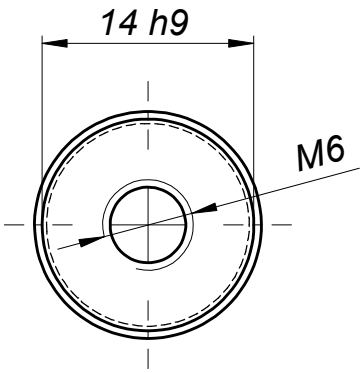

Observations: Material AISI 316	2:1 Toleran. ISO 2768-1: 1989 Medium	Outlet shaft	DM-20

Designed	21/11/21	
Drawn	21/11/21	
Copied	21/11/21	
Verified		

NOVA School of Science and Technology

Master's Dissertation - Testing device for an anatomical part

Francisco Castanho
Nº51959

22

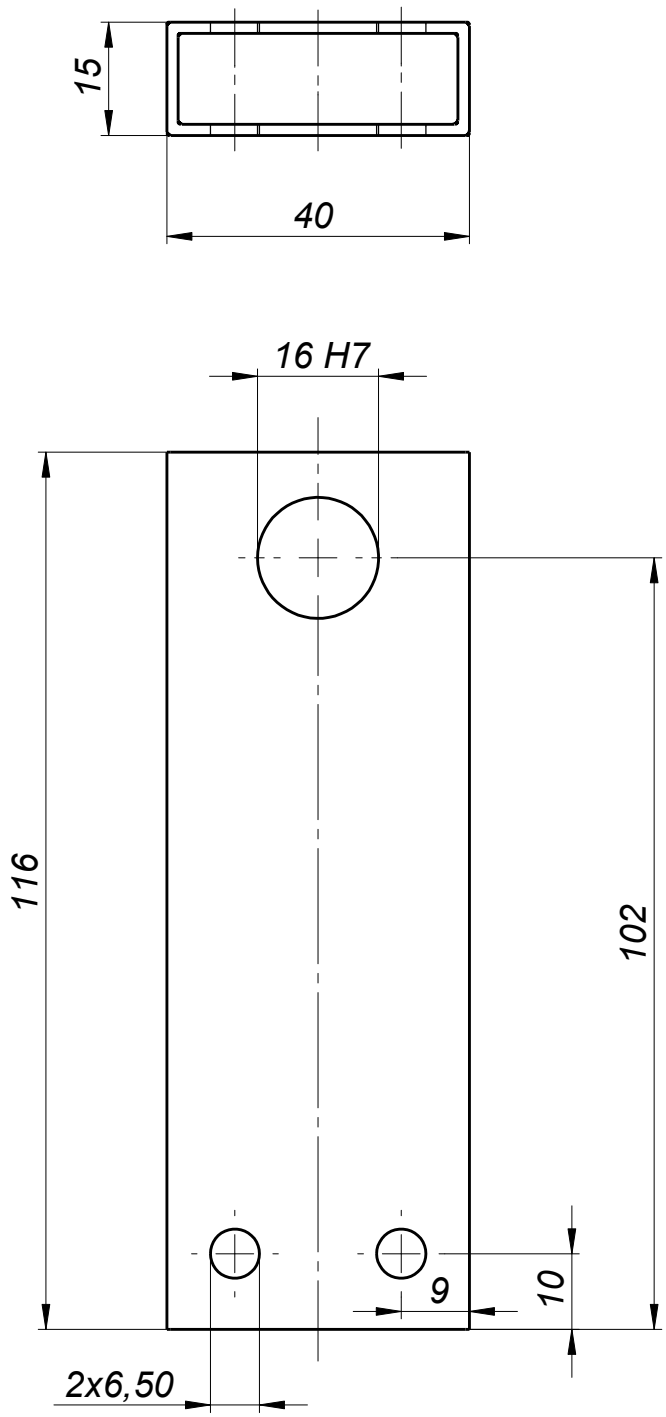

Observations: Rectangular profile tube Section 40x15 - Thickness: 1,5 mm ASTM A-554 AISI 316	1:1 Toleran. ISO 2768-1: 1989 Medium	Structural profile	DM-21

Designed	21/11/21	
Drawn	21/11/21	
Copied	21/11/21	
Verified		

NOVA School of Science and Technology

Master's Dissertation - Testing device for an anatomical part

Francisco Castanho
Nº51959

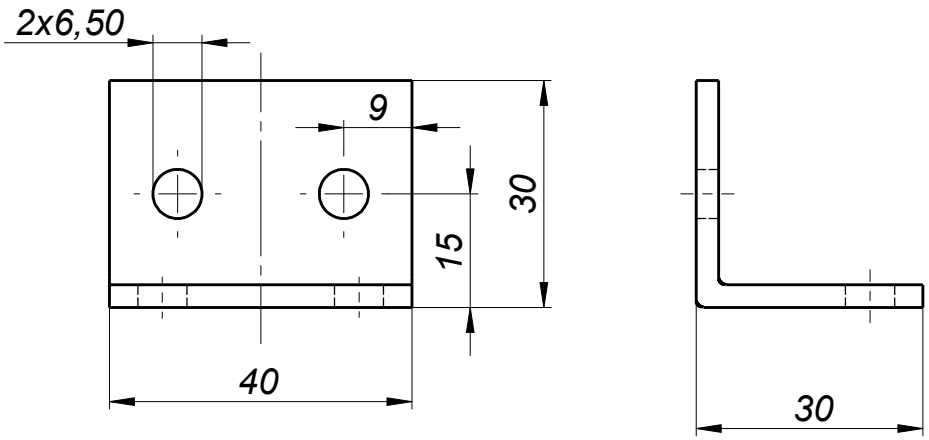

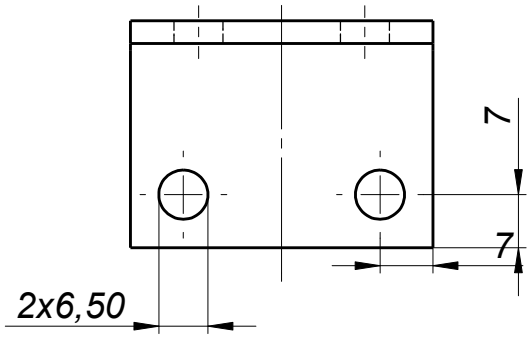

Observations: L-shaped profile - Section 30x30 mm Thickness: 3 mm DIN 1028 AISI 316	1:1 Toleran. ISO 2768-1: 1989 Medium	L-shaped profile	DM-22

Designed	21/11/21	
Drawn	21/11/21	
Copied	21/11/21	
Verified		

NOVA School of Science and Technology

Master's Dissertation - Testing device for an anatomical part

Francisco Castanho
Nº51959

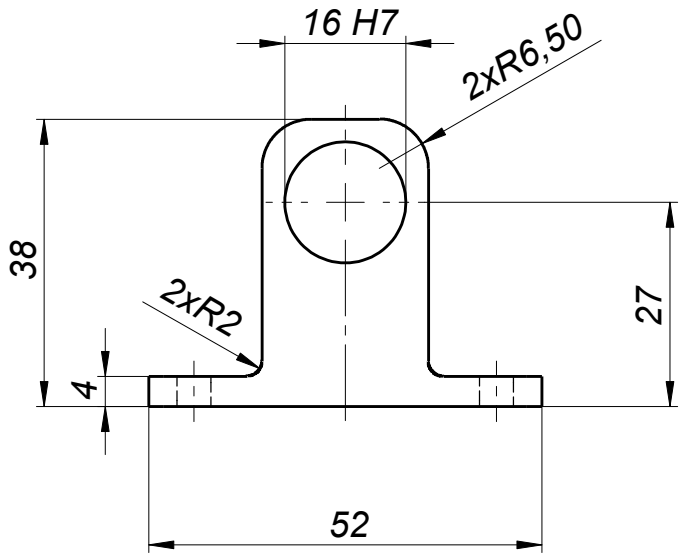

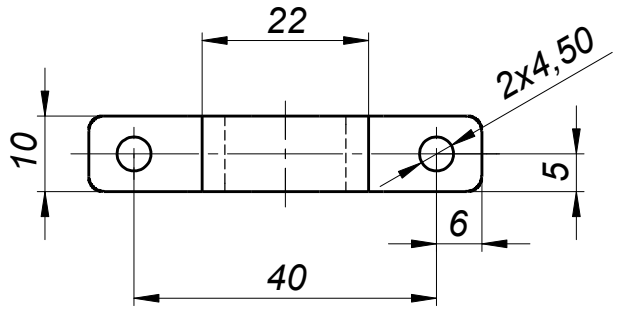

Observations:

Material
AISI 316

1:1

Toleran.

ISO 2768-1: 1989
Medium

Specimen rotation shaft holder

DM-22

Designed	21/11/21	
Drawn	21/11/21	
Copied	21/11/21	
Verified		

NOVA School of Science and Technology

Master's Dissertation - Testing device for an anatomical part

Francisco Castanho
Nº51959

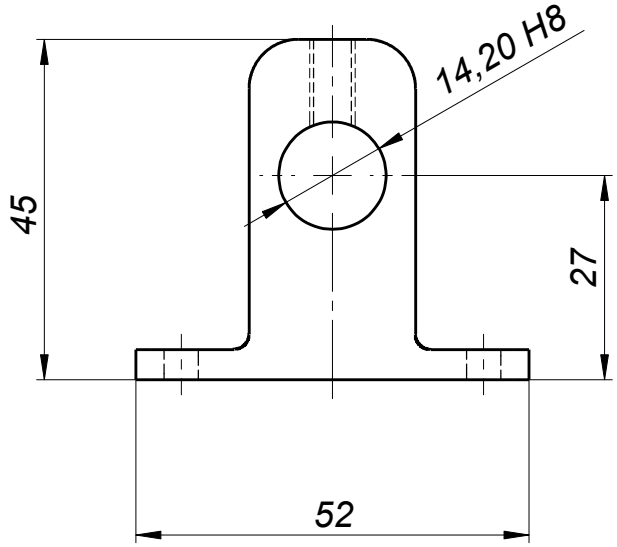

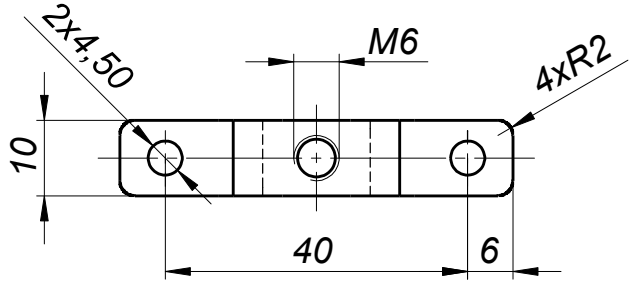

Observations: Material AISI 316	1:1 Toleran. ISO 2768-1: 1989 Medium	Specimen rotation shaft locker

DM-24

Designed	21/11/21	
Drawn	21/11/21	
Copied	21/11/21	
Verified		

NOVA School of Science and Technology

Master's Dissertation - Testing device for an anatomical part

Francisco Castanho
Nº51959

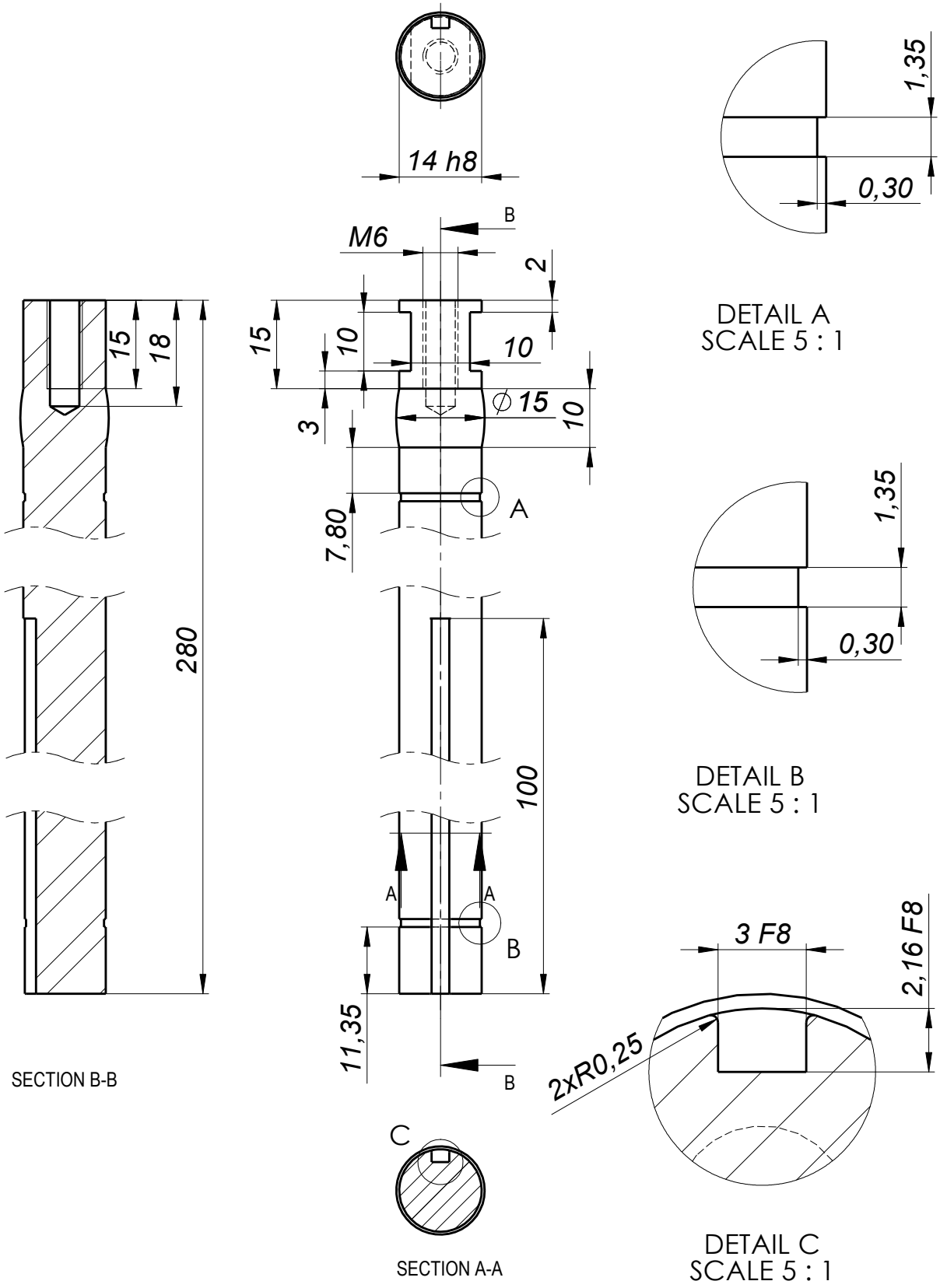

Observations:	1:1	Specimen rotation shaft	DM-25
Material AISI 316	Toleran. ISO 2768-1: 1989 Medium		

Designed	21/11/21	
Drawn	21/11/21	
Copied	21/11/21	
Verified		

NOVA School of Science and Technology

Master's Dissertation - Testing device for an anatomical part

Francisco Castanho
Nº51959

27

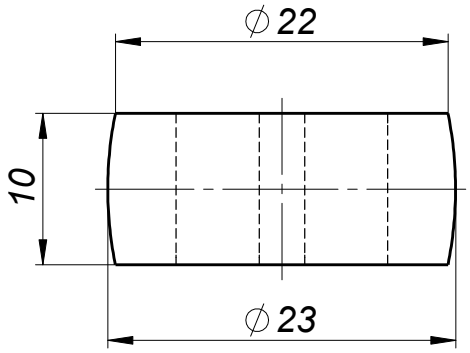

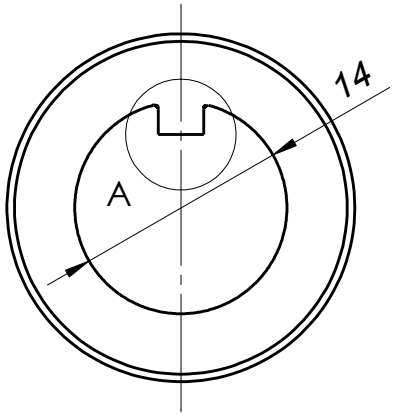

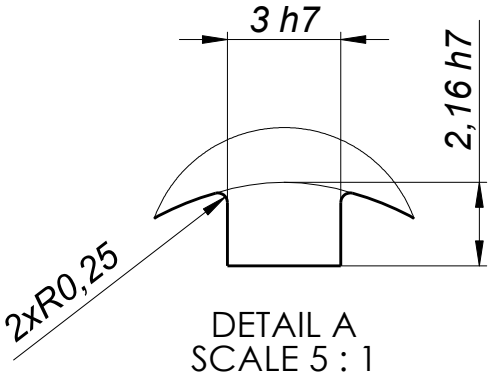

DETAIL A
SCALE 5 : 1

Observations:	2:1	Pulley	DM-26
Material AISI 316	Toleran. ISO 2768-1: 1989 Medium		

Designed	21/11/21	
Drawn	21/11/21	
Copied	21/11/21	
Verified		

NOVA School of Science and Technology

Master's Dissertation - Testing device for an anatomical part

Francisco Castanho
Nº51959

28

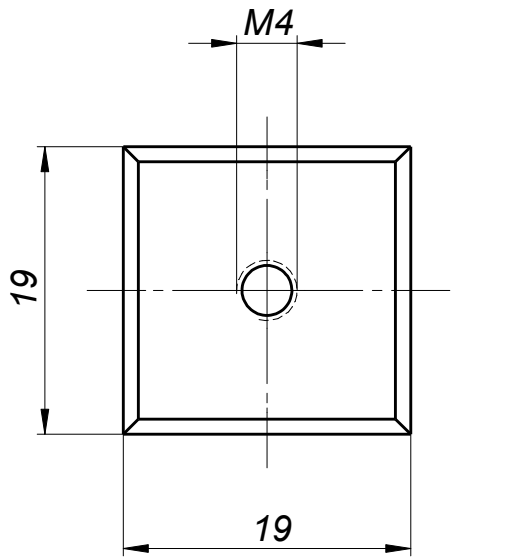

Observations:	2:1	Table fixator	DM-27
Material AISI 316	Toleran. ISO 2768-1: 1989 Medium		

29

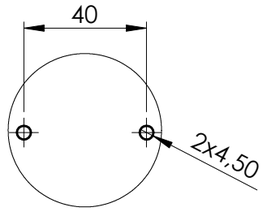

DETAIL F
SCALE 1 : 2

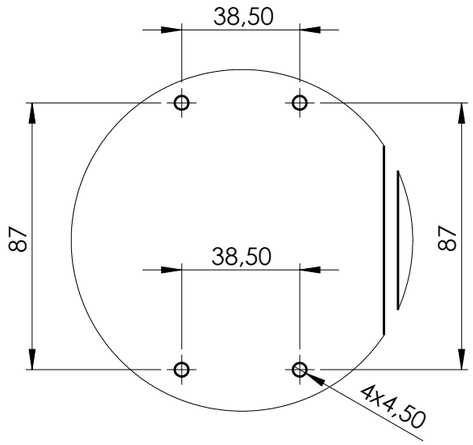

DETAIL D
SCALE 1 : 2

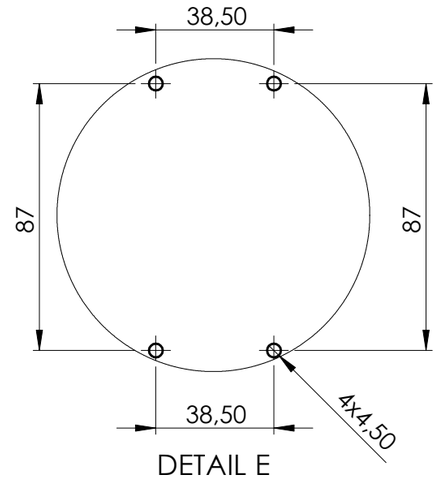

DETAIL E
SCALE 1 : 2

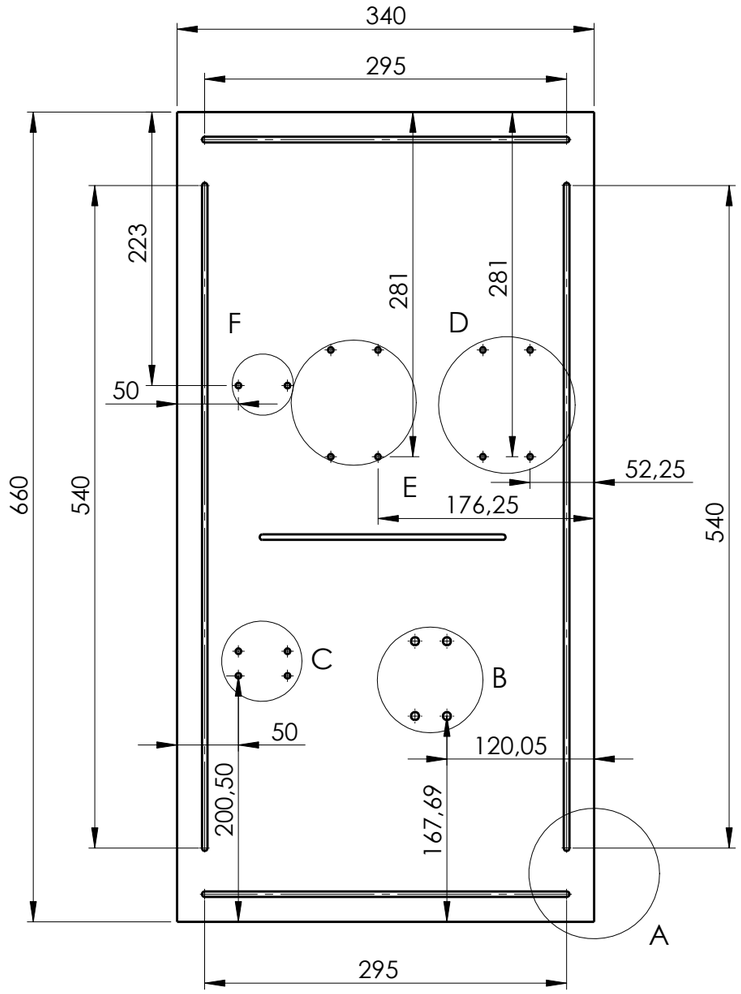

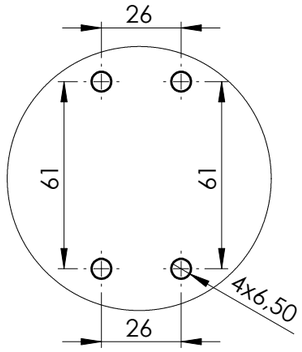

DETAIL B
SCALE 1 : 2

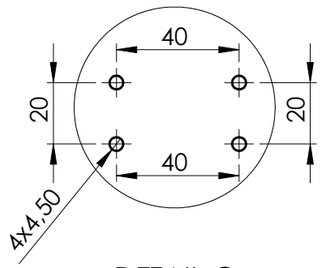

DETAIL C
SCALE 1 : 2

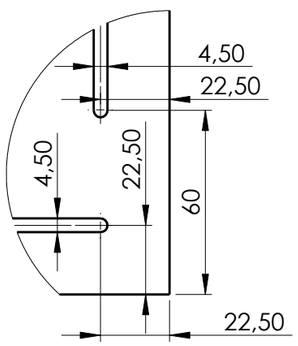

DETAIL A
SCALE 1 : 2

Observations:

Material AISI 316

Detail A repeats on all other corners.

Designed	24/11/21		NOVA School of Science and Technology	Francisco Castanho Nº 51959
Drawn	24/11/21		Master's Dissertation - Testing device for an anatomical part	
Copied	24/11/21			
Verified				
1:5			Setup table top	DM-29
Toleranc. ISO 2768-1: 1989 Medium				

30

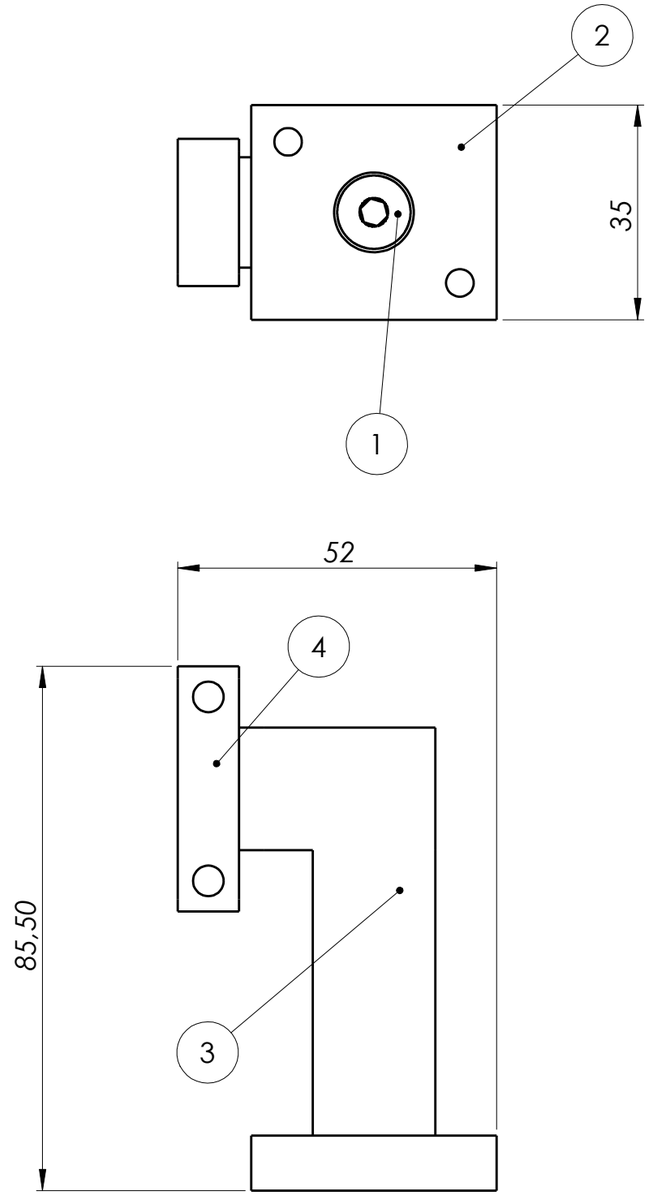

1	Connector arm-1	DM-4	AISI 316	4			
1	Connector arm-2	DM-5	AISI 316	3			
1	Connector arm-3	DM-6	AISI 316	2			
2	Hexagonal socket countersunk head screw M6x10mm	DIN 7991	Stainless steel A2	1			Commercial component-Fabory
NO.	DESIGNATION	DRAWING NO. STANDARD NO.	MATERIAL	ITEM NO.	CAST NO. MATRIX NO.	WEIGHT (g)	OBSERVATIONS

Designed	23/11/21	NOVA School of Science and Technology Master's Dissertation - Testing device for an anatomical part
Drawn	23/11/21	
Copied	23/11/21	
Verified		

Francisco Castanho
Nº 51959

1:1

Subset 1

DM-S1

31

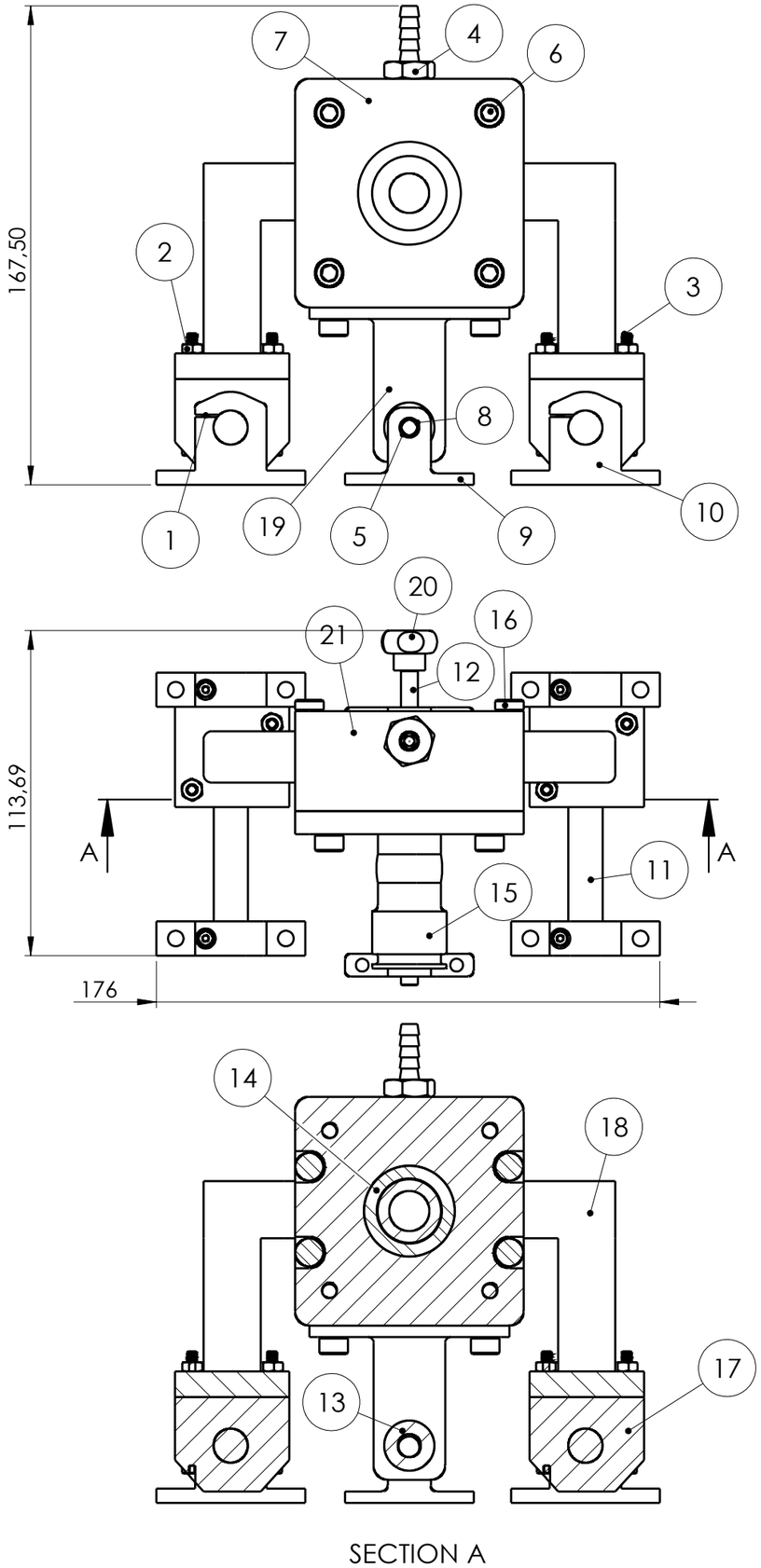

SECTION A

NO.	DESIGNATION	DRAWING NO. STANDARD NO.	MATERIAL	ITEM NO.	CAST NO. MATRIX NO.	WEIGHT (g)	OBSERVATIONS
1	Connector block	DM-3	AISI 316	21			
1	Plastic holder M4x10		Plastic	20			Commercial component-Fabory
1	Ball screw nut holder	DM-7	AISI 316	19			
1	Subset 1	DM-S1		18			
2	Linear guide	LUJR 12		17			Commercial component-SKF
8	Hexagonal low profile socket head screw M5x8mm	DIN 7984	Stainless Steel A2	16			Commercial component-Fabory
1	Fixation part	DM-1	AISI 316	15			
1	Radial shaft seal	8634		14			Commercial component-SKF
1	Ball screw nut			13			Included in ball screw
1	Ball screw	DM-9		12			Commercial component-SKF
4	Precision shaft	LJ MR 12 100 ESSC2		11			Commercial component-SKF
4	Shaft block	LSCS 12		10			Commercial component-SKF
2	Ball screw holder	DM-8	AISI 316	9			
2	Retaining ring for shafts 6MM	DIN 471	Stainless steel 1.4122	8			Commercial component-Fabory
1	Fixation part locker	DM-2	AISI 316	7			
6	Hexagonal socket head screw M6x16mm	DIN 912	Stainless Steel A2	6			Commercial component-Fabory
2	Sleeve bearing	GFM-060709-045	Polymer	5			Commercial component-Igus
1	Male hose adapter	623400 00 44 BZ 00	AISI 316L	4			Commercial component-AIGNEP
4	Hexagonal low profile socket head screw M4x40mm	DIN 7984	Stainless Steel A2	3			Commercial component-Fabory
1	Hexagonal nut M4	DIN 934	Stainless Steel A2	2			Commercial component-Fabory
4	Hexagonal low profile socket head screw M3x8mm	DIN 7984	Stainless Steel A2	1			Commercial component-Fabory

Designed	23/11/21	NOVA School of Science and Technology Master's Dissertation - Testing device for an anatomical part
Drawn	23/11/21	
Copied	23/11/21	
Verified		

Francisco Castanho
Nº 51959

1:2

Subset 2

DM-S2

32

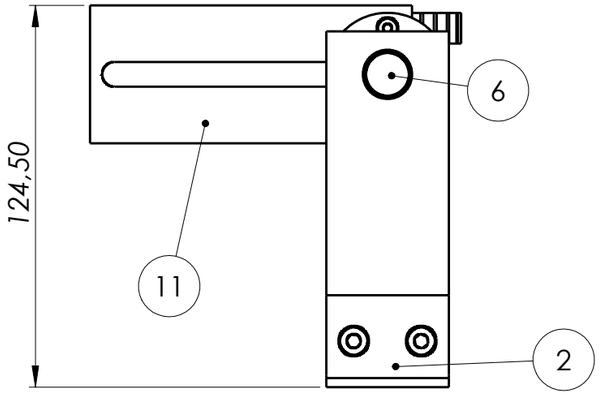

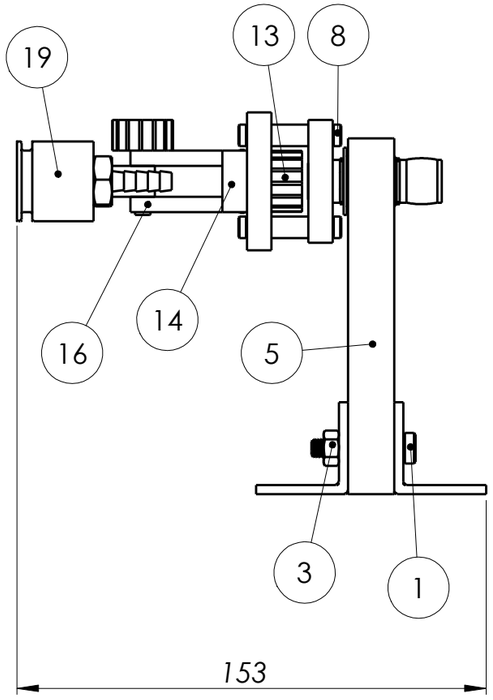

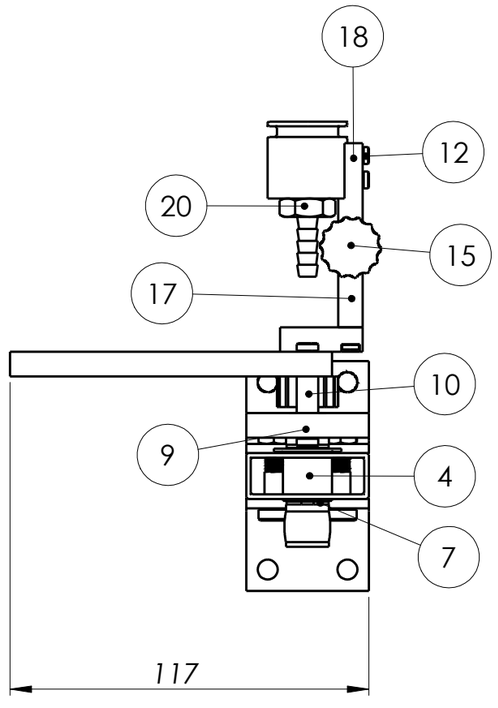

1	Male hose adapter	623400 00 44 BZ 00	AISI 316L	20			Commercial component - AIGNEP
1	Fixation part (inlet side)	DM-10	AISI 316	19			
1	Articulation connector - 1	DM-11	AISI 316	18			
1	Articulation connector - 2	DM-12	AISI 316	17			
1	Articulation connector - 3	DM-13	AISI 316	16			
1	Hinge pin	DM-15	AISI 316	15			
1	Slot connector	DM-14	AISI 316	14			
1	Slot screw	DM-16	AISI 316	13			
4	Hexagonal low profile socket head screw M3x10mm	DIN 7984	Staineless steel A2	12			Commercial component - Fabory
1	Connector with slot	DM-17	AISI 316	11			
2	Flange connector rod	DM-18	AISI 316	10			
1	Flange	DM-19	AISI 316	9			
4	Hexagonal low profile socket head screw M4x8mm	DIN 7984	Staineless steel A2	8			Commercial component - Fabory
2	Retaining ring for shafts 14MM	DIN 471	Staineless steel 1.4122	7			Commercial component - Fabory
1	Outlet shaft	DM-20	AISI 316	6			
1	Structutral profile	DM-21	AISI 316	5			
1	SLeeve bearing	GFM-1416-17	Polymer	4			
2	L-shaped profile 30x30mm	DM-22	AISI 316	2			Commercial component - Fabory
2	Hexagonal low profile socket head screw M6x30mm	DIN 7984	Staineless steel A2	1			Commercial component - Fabory
NO.	DESIGNATION	DRAWING NO. STANDARD NO.	MATERIAL	ITEM NO.	CAST NO. MATRIX NO.	WEIGHT (g)	OBSERVATIONS
22	Assem3^Subconj3		1				

Designed	23/11/21	NOVA School of Science and Technology	Francisco Castanho Nº 51959
Drawn	23/11/21	Master's Dissertation - Testing device for an anatomical part	
Copied	23/11/21		
Verified			
1:2		Subset 3	DM-S3

33

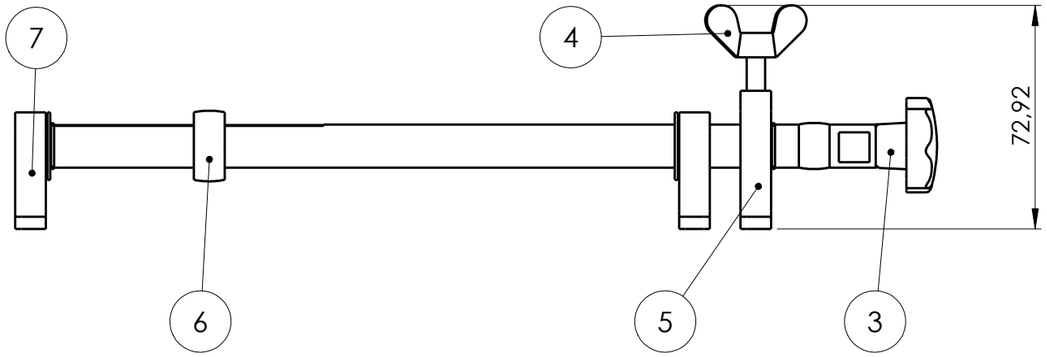

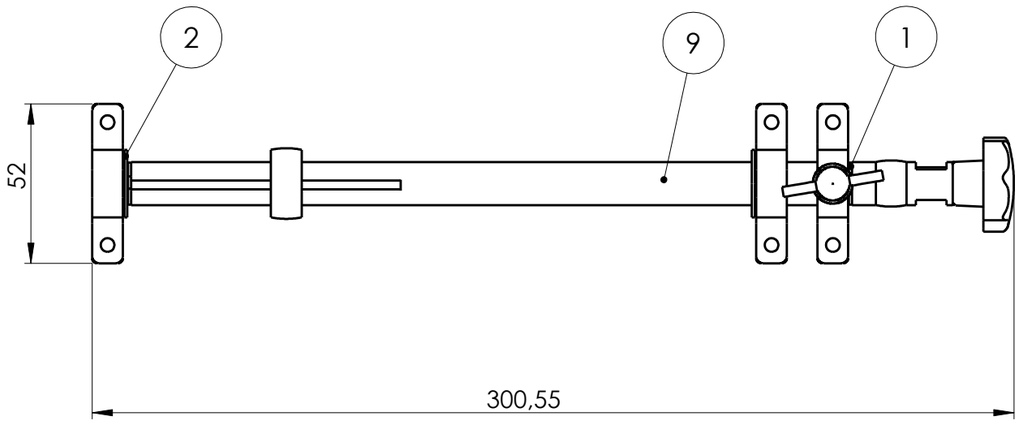

1	Specimen rotation shaft	DM-25	AISI 316	9			
2	Specimen rotation shaft holder	DM-22	AISI 316	7			
1	Pulley	DM-26	AISI 316	6			
1	Specimen rotation shaft locker	DM-24	AISI 316	5			
1	Wing screw M6x25mm	DIN 316	Stainless steel A2	4			Commercial componente-Fabory
1	Star grip type plastic handle	FS31 M6X15	Plastic	3			Commercial componente-Fabory
2	Aluminium profile	GFM-1416-08	Polymer	2			Commercial componente-Fabory
2	Retaining rinf for shafts 14MM	DIN 471	Stainless steel 1.4122	1			Commercial componente-Fabory
NO.	DESIGNATION	DRAWING NO. STANDARD NO.	MATERIAL	ITEM NO.	CAST NO. MATRIX NO.	WEIGHT(g)	OBSERVATIONS

Designed	23/11/21	NOVA School of Science and Technology
Drawn	23/11/21	Master's Dissertation - Testing device for an anatomical part
Copied	23/11/21	
Verified		

Francisco Castanho
Nº 51959

1:2

Subset 4

DM-S4

34

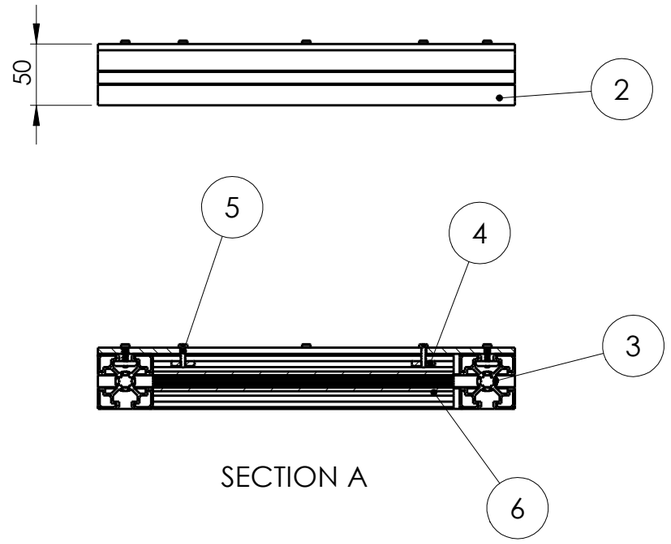

SECTION A

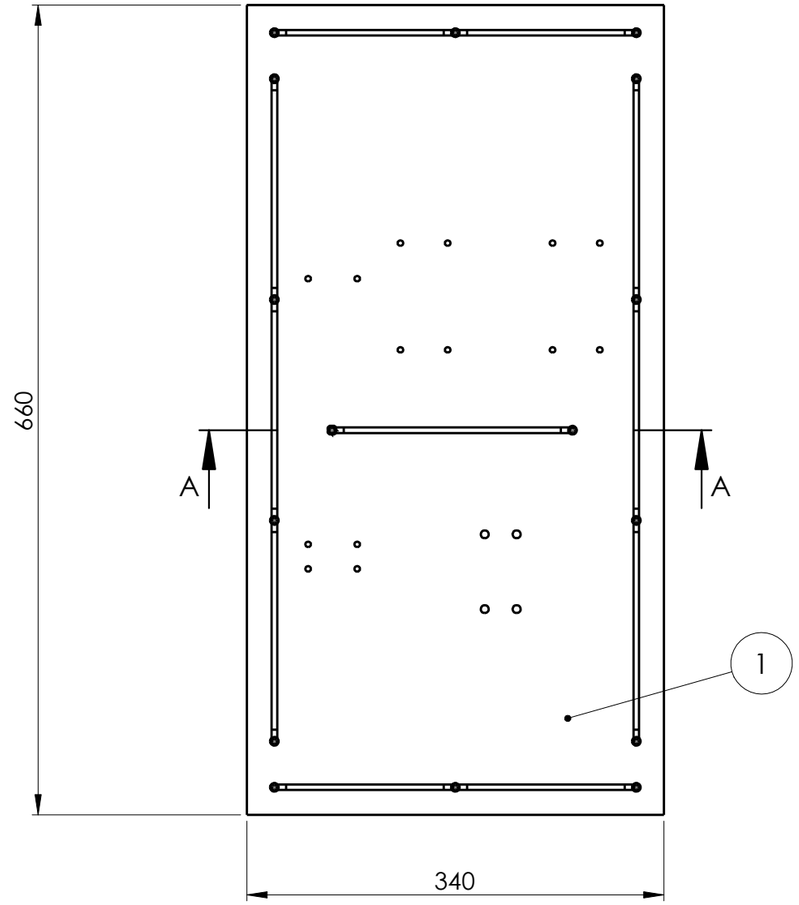

NO.	DESIGNATION	DRAWING NO. STANDARD NO.	MATERIAL	ITEM NO.	CAST NO. MATRIX NO.	WEIGHT(g)	OBSERVATIONS
16	Table fixator	DM-27	AISI 316	6			
16	Hexagonal low profile socket head screw M4x14mm	DIN 7984	Stainless Steel A2	5			Commercial component-Fabory
1	Aluminium profile 45x45x245mm	MW10007	Aluminium alloy Al Mg Si 6060 (ISO 9006/1)	4			Commercial component-LIPRO/Metal Work
2	Aluminium profile 45x45x565mm	MW10007	Aluminium alloy Al Mg Si 6060 (ISO 9006/1)	3			Commercial component-LIPRO/Metal Work
2	Aluminium profile 45x45x340mm	MW10007	Aluminium alloy Al Mg Si 6060 (ISO 9006/1)	2			Commercial component-LIPRO/Metal Work
1	Setup table top	DM-28	AISI 316	1			

Designed	25/11/21	NOVA School of Science and Technology Master's Dissertation - Testing device for an anatomical part	Francisco Castanho Nº 51959
Drawn	25/11/21		
Copied	25/11/21		
Verified			
1:5		Device setup table	DM-S5

35

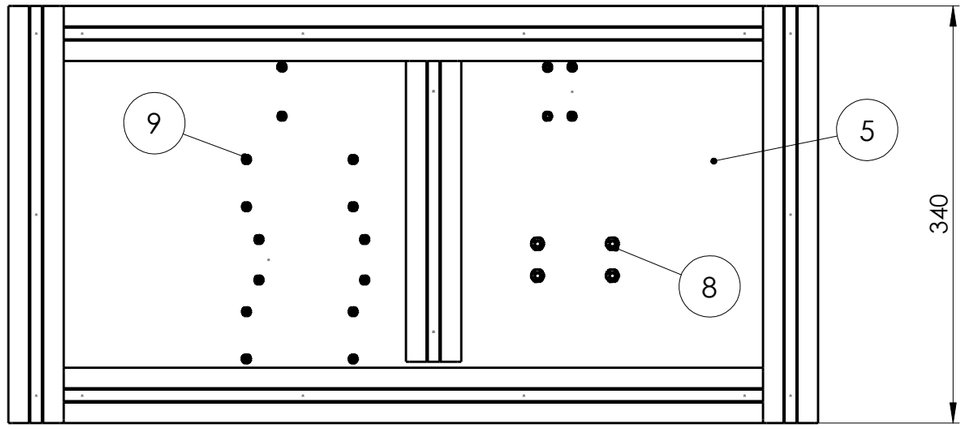

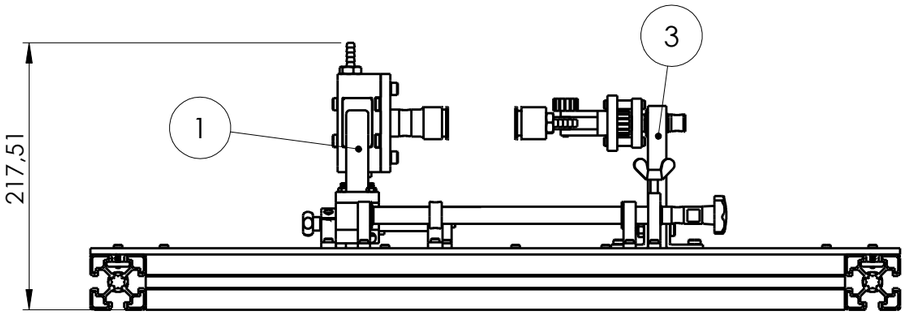

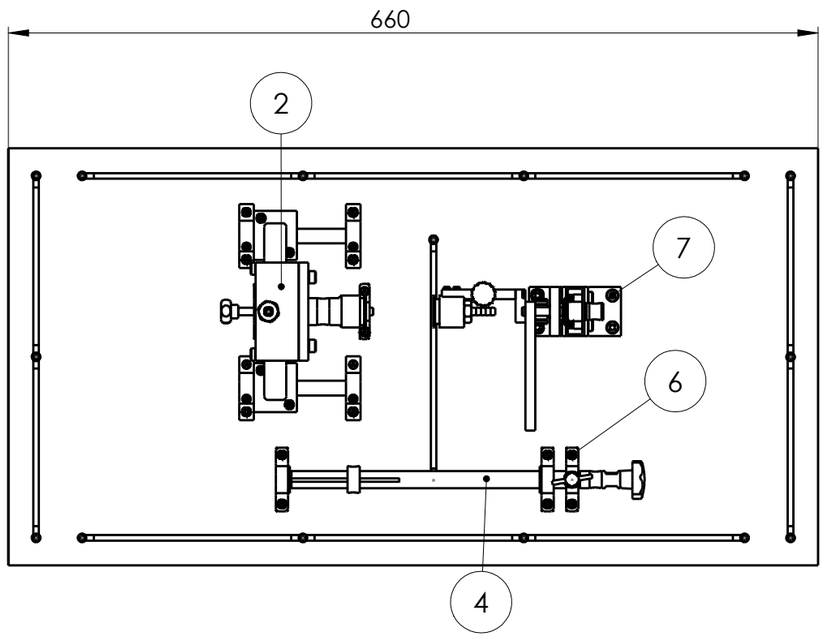

NO.	DESIGNATION	DRAWING NO. STANDARD NO.	MATERIAL	ITEM NO.	CAST NO. MATRIX NO.	WEIGHT(g)	OBSERVATIONS
18	Hexagonal nut M4	DIN 934	Stainless steel A2	9			Commercial component-Fabory
4	Hexagonal nut M6	DIN 934	Stainless steel A2	8			Commercial component-Fabory
4	Hexagonal low profile socket head screw M6x20mm	DIN 7984	Stainless steel A2	7			Commercial component-Fabory
18	Hexagonal low profile socket head screw M4x20mm	DIN 7984	Stainless steel A2	6			Commercial component-Fabory
1	Device setup table	DM-S5		5			
1	Subset 4	DM-S4		4			
1	Subset 3	DM-S3		3			
1	Subset 2	DM-S2		2			
2	Subset 1	DM-S1		1			

Designed	25/11/21	
Drawn	25/11/21	
Copied	25/11/21	
Verified		

NOVA School of Science and Technology

Master's Dissertation - Testing device for an anatomical part

Francisco Castanho
Nº 51959

1:5

Final assembly

DM-S6